

**Measurement of the W Boson Mass  
in the  $W^+W^- \rightarrow q\bar{q}\ell\bar{\nu}$  Channel  
with the OPAL Detector at LEP**

Dissertation der Fakultät für Physik  
der  
Ludwig-Maximilians-Universität München

vorgelegt von

Jörg Dubbert

aus

Paderborn

---

München, den 23. November 2000



**Measurement of the W Boson Mass  
in the  $W^+W^- \rightarrow q\bar{q}\ell\bar{\nu}$  Channel  
with the OPAL Detector at LEP**

Dissertation der Fakultät für Physik  
der  
Ludwig-Maximilians-Universität München

vorgelegt von

Jörg Dubbert

aus

Paderborn

---

München, den 23. November 2000

1. Gutachter: Prof. Dr. Dorothee Schaile

2. Gutachter: Prof. Dr. M. Faessler

Tag der mündlichen Prüfung: 24. April 2001

Intent and outcome are so rarely coincident.  
*Neil Gaiman, The Sandman: The Kindly Ones 9*



## Abstract

A new method to measure the mass of the W boson in the  $W^+W^- \rightarrow q\bar{q}\ell\bar{\nu}$  channel, a convolution fit, was developed and applied to data recorded with the OPAL experiment at LEP.

The Convolution method takes into account the precision of the measurement of each single event of the data sample in an unbinned maximum likelihood fit. The parent distribution of the likelihood fit includes a statistical description of the effects of Initial State Radiation on the mass reconstruction. An improvement of about 10% in the statistical error of the W mass measurement compared to other methods used within the OPAL collaboration is anticipated.

Using an integrated luminosity of  $57 \text{ pb}^{-1}$  of data collected at a center-of-mass energy of  $\sqrt{s} = 183 \text{ GeV}$  and  $183 \text{ pb}^{-1}$  of data collected at a center-of-mass energy of  $\sqrt{s} = 189 \text{ GeV}$ , the mass of the W boson was measured to be

$$M_W = 80.391 \pm 0.098 \text{ GeV}/c^2,$$

assuming the Standard Model relation between the mass and the width of the W boson. The measured mass of the W boson is in excellent agreement with other direct measurements and with the Standard Model prediction derived from electroweak precision tests.





## Zusammenfassung

Eine neue Methode, ein Faltungsfitt, zur Bestimmung der Masse des W-Bosons im  $W^+W^- \rightarrow q\bar{q}\ell\bar{\nu}$  Zerfallskanal wurde entwickelt und auf Daten, die mit dem OPAL Experiment am LEP Beschleuniger gesammelt wurden, angewandt.

Die Faltungsmethode berücksichtigt die Genauigkeit der Messung jedes einzelnen Ereignisses des Datensatzes in einem ungebinnten Maximum-Likelihood-Fit. Die der Likelihood-Anpassung zugrunde liegende Wahrscheinlichkeitsverteilung beinhaltet eine statistische Beschreibung der Auswirkungen von Photonabstrahlung im Anfangszustand auf die Massenrekonstruktion. Im Vergleich zu anderen Meßmethoden, die in der OPAL-Kollaboration angewendet werden, wird eine Verminderung des statistischen Fehlers der bestimmten W-Masse um etwa 10% vorhergesagt.

Für die integrierte Luminosität von  $57 \text{ pb}^{-1}$  und  $183 \text{ pb}^{-1}$  an Daten, die bei Schwerpunktsenergien von  $\sqrt{s} = 183 \text{ GeV}$  und  $\sqrt{s} = 189 \text{ GeV}$  aufgezeichnet wurden, ergibt sich die W-Masse unter Verwendung der Standard-Modell-Relation zwischen Masse und Breite des W-Bosons zu

$$M_W = 80.391 \pm 0.098 \text{ GeV}/c^2.$$

Die gemessene Masse des W-Bosons ist in sehr guter Übereinstimmung mit anderen direkten Messungen und mit den Standardmodell-Vorhersagen aus elektroschwachen Präzisionsmessungen.



# Contents

<b>1</b>	<b>Introduction and Overview</b>	<b>13</b>
<b>2</b>	<b>LEP and OPAL</b>	<b>17</b>
2.1	The Large Electron Positron Collider LEP . . . . .	17
2.2	The OPAL Detector . . . . .	19
2.2.1	The Tracking System . . . . .	20
2.2.2	The Calorimeters . . . . .	21
2.2.3	The Muon System . . . . .	23
2.2.4	The Forward Detector and the SiW Luminometer . . . . .	23
<b>3</b>	<b>The Standard Model</b>	<b>25</b>
3.1	Electroweak Theory . . . . .	26
3.2	Quantum Chromodynamics . . . . .	29
<b>4</b>	<b>Physics of W Boson Pairs at LEP2</b>	<b>33</b>
4.1	The W Boson . . . . .	33
4.1.1	The W Mass . . . . .	33
4.1.2	The W Width . . . . .	35
4.1.3	Gauge Boson Couplings . . . . .	37
4.2	Pair Production of W Bosons . . . . .	38
4.3	Four-Fermion Processes . . . . .	40
4.4	Two-Fermion Processes . . . . .	44
4.5	Final State Interactions . . . . .	45
4.5.1	Bose-Einstein Correlation . . . . .	45
4.5.2	Color Reconnection . . . . .	46
4.6	WW Event Classes . . . . .	46
4.6.1	The Leptonic Decay Channel, $W^+W^- \rightarrow \bar{\ell}\nu\ell\bar{\nu}$ . . . . .	47
4.6.2	The Semileptonic Decay Channel, $W^+W^- \rightarrow q\bar{q}\ell\bar{\nu}$ . . . . .	49
4.6.3	The Hadronic Decay Channel, $W^+W^- \rightarrow q\bar{q}q\bar{q}$ . . . . .	50
<b>5</b>	<b>Simulation of Physics Events</b>	<b>53</b>
5.1	Monte Carlo Generators . . . . .	53
5.2	The Hadronization Model . . . . .	54
5.3	Tau Decays . . . . .	55

5.4	Final State Interaction Models . . . . .	55
5.4.1	Bose-Einstein Correlations . . . . .	55
5.4.2	Color Reconnection . . . . .	55
<b>6</b>	<b>From <math>W^+W^- \rightarrow q\bar{q}\ell\bar{\nu}</math> Events to the W Boson Mass <math>M_W</math></b>	<b>57</b>
6.1	On-Line Data Flow . . . . .	57
6.2	Off-line Analysis . . . . .	59
<b>7</b>	<b>Selection and Reconstruction of <math>W^+W^- \rightarrow q\bar{q}\ell\bar{\nu}</math> Events</b>	<b>61</b>
7.1	The Event Selection . . . . .	62
7.1.1	Common Track and Cluster Quality Cuts . . . . .	62
7.1.2	The $W^+W^- \rightarrow \bar{\ell}\nu\ell\bar{\nu}$ Event Selection . . . . .	62
7.1.3	The $W^+W^- \rightarrow q\bar{q}\ell\bar{\nu}$ Event Selection . . . . .	63
7.1.4	The $W^+W^- \rightarrow q\bar{q}q\bar{q}$ Event Selection . . . . .	68
7.2	Reconstruction of $W^+W^- \rightarrow q\bar{q}\ell\bar{\nu}$ Events . . . . .	69
7.2.1	The Lepton . . . . .	69
7.2.2	Evil Taus . . . . .	70
7.2.3	Events without a Lepton Track . . . . .	74
7.2.4	The Non-Leptonic Part . . . . .	75
7.2.5	Monte Carlo Detector Recalibration . . . . .	77
7.3	Determination of the Invariant Mass . . . . .	77
7.3.1	Scaled Hadronic Mass . . . . .	78
7.3.2	Constrained Kinematic Fits . . . . .	79
<b>8</b>	<b>Measurement of the Mass of the W Boson</b>	<b>87</b>
8.1	Overview . . . . .	87
8.2	The Convolution Method . . . . .	90
8.2.1	Calculation of the Event Probability Density . . . . .	90
8.2.2	ISR and Effects on the Event Mass Reconstruction . . . . .	96
8.2.3	The Physics Function . . . . .	99
8.2.4	Data Quality Cuts . . . . .	102
8.2.5	Maximum Likelihood Fit . . . . .	105
8.3	Ensemble Tests . . . . .	108
8.4	Bias Correction and Calibration . . . . .	110
8.5	Expected Statistical Errors . . . . .	111
8.6	Systematic Uncertainties . . . . .	114
<b>9</b>	<b>Results and Discussion</b>	<b>125</b>
9.1	Results at $\sqrt{s} = 183$ GeV . . . . .	125
9.2	Results at $\sqrt{s} = 189$ GeV . . . . .	128
9.3	Combined Results . . . . .	131
9.4	Comparison with Alternative Methods . . . . .	134
9.4.1	The Reweighting Method . . . . .	134
9.4.2	The Breit-Wigner Fit . . . . .	134

<i>CONTENTS</i>	3
9.4.3 Comparison of Results . . . . .	135
9.5 Comparison with the other LEP Experiments . . . . .	143
9.6 Summary of Results . . . . .	143
<b>10 Summary</b>	<b>149</b>
<b>A Performance of the Evil Tau Rejection</b>	<b>153</b>
<b>B Influence of the Penalty Factors on the Event Probability Density</b>	<b>157</b>
<b>C Correlation between Scaled Hadronic Mass and Fitted Mass</b>	<b>161</b>
<b>D Acceptance of the Data Quality Cuts</b>	<b>165</b>
<b>E Monte Carlo Samples</b>	<b>169</b>
E.1 Monte Carlo Samples at $\sqrt{s} = 183$ GeV . . . . .	169
E.2 Monte Carlo Samples at $\sqrt{s} = 189$ GeV . . . . .	170
<b>Bibliography</b>	<b>173</b>



# List of Figures

2.1	Aerial view of CERN with the SPS and LEP collider . . . . .	17
2.2	Three-dimensional schematic view of the OPAL detector . . . . .	20
4.1	Feynman diagrams of 1-loop corrections to the W propagator . . . . .	34
4.2	Comparison of the Standard Model predictions of the top and W masses with indirect and direct measurements . . . . .	35
4.3	Lowest order Feynman diagrams for $e^+e^- \rightarrow W^+W^- \rightarrow 4f$ . . . . .	38
4.4	Total cross section of the W-pair production as calculated from the CC03 diagrams as a function of the center-of-mass energy . . . . .	39
4.5	OPAL measurements of the total cross section of the W-pair production . . . . .	40
4.6	The six fundamental classes of 4-fermion diagrams . . . . .	41
4.7	The four most important 4-fermion background processes in W-pair physics . . . . .	42
4.8	Cross sections of the most important processes in the center-of-mass energy range of LEP2 . . . . .	43
4.9	Lowest order Feynman diagrams for $e^+e^- \rightarrow Z^0/\gamma \rightarrow f\bar{f}$ and $e^+e^- \rightarrow Z^0/\gamma \rightarrow f\bar{f}\gamma$ . . . . .	44
4.10	An event selected as $W^+W^- \rightarrow \bar{\ell}\nu\ell\bar{\nu}$ as seen in the OPAL event display . . . . .	47
4.11	An event selected as $W^+W^- \rightarrow q\bar{q}\ell\bar{\nu}$ as seen in the OPAL event display . . . . .	49
4.12	An event selected as $W^+W^- \rightarrow q\bar{q}q\bar{q}$ as seen in the OPAL event display . . . . .	50
6.1	Data flow from the event recording to the physics result . . . . .	58
7.1	Likelihood distributions for the $W^+W^- \rightarrow q\bar{q}\ell\bar{\nu}$ selections . . . . .	67
7.2	Deviation of the reconstructed direction of flight of the tau lepton in $W^+W^- \rightarrow q\bar{q}\tau\bar{\nu}$ events from its true direction . . . . .	71
7.3	Distribution of the fitted W mass for $W^+W^- \rightarrow q\bar{q}\tau\bar{\nu}$ events before and after the <i>Evil tau rejection</i> . . . . .	73
7.4	Distribution of the fitted W mass for <i>Evil tau</i> events . . . . .	74

7.5	Distribution of the fitted W mass for <i>Trackless</i> $W^+W^- \rightarrow q\bar{q}e\bar{\nu}$ events and <i>Trackless</i> $W^+W^- \rightarrow q\bar{q}\mu\bar{\nu}$ events . . . . .	75
7.6	Distribution and resolution of the hadronic mass, the scaled hadronic mass, and the fitted mass . . . . .	79
7.7	Distribution of the fit probabilities at a center-of-mass energy of $\sqrt{s} = 189$ GeV . . . . .	84
7.8	Comparison of the results of the standard kinematic fit and the $\chi^2$ -minimization . . . . .	85
8.1	Distribution of the event mass errors for $W^+W^- \rightarrow q\bar{q}q\bar{q}$ and $W^+W^- \rightarrow q\bar{q}\ell\bar{\nu}$ events . . . . .	89
8.2	Examples of $\chi_i^2(m)$ and corresponding event probability densities $P_i(m)$ for data events at $\sqrt{s} = 189$ GeV . . . . .	93
8.3	Invariant mass of the W boson as a function of the energy $E$ of one decay product and the inter-particle angle $\theta$ . . . . .	94
8.4	Invariant mass of the W boson as a function of the energy $E$ of the higher energetic jet . . . . .	95
8.5	Spectrum of the ISR photons in selected $e^+e^- \rightarrow W^+W^- \rightarrow q\bar{q}\ell\bar{\nu}$ events at a center-of-mass energy of $\sqrt{s} = 189$ GeV . . . . .	97
8.6	Mean shift between the true mean W mass in an event and the fitted mass as a function of the ISR photon energy . . . . .	98
8.7	Comparison of the mean generated mass of the two W bosons in Monte Carlo events with a Breit-Wigner function . . . . .	100
8.8	Comparison of the signal function $f_{\text{signal}}(m; M_W, \Gamma_W, \sqrt{s})$ with a relativistic Breit-Wigner function . . . . .	101
8.9	Distribution of the reconstructed mass for background events at a center-of-mass energy of $\sqrt{s} = 183$ GeV . . . . .	103
8.10	Distribution of the reconstructed mass for background events at a center-of-mass energy of $\sqrt{s} = 189$ GeV . . . . .	104
8.11	Calibration functions for $M_W$ at $\sqrt{s} = 183$ GeV . . . . .	112
8.12	Calibration functions for $M_W$ at $\sqrt{s} = 189$ GeV . . . . .	113
8.13	W mass and pull distributions of the ensemble test for a center-of-mass energy $\sqrt{s} = 183$ GeV . . . . .	115
8.14	W mass and pull distributions of the ensemble test for a center-of-mass energy $\sqrt{s} = 189$ GeV . . . . .	116
9.1	Results for $M_W$ in the $W^+W^- \rightarrow q\bar{q}\ell\bar{\nu}$ channel for the data collected with the OPAL detector at the center-of-mass energy of $\sqrt{s} = 183$ GeV . . . . .	128
9.2	Results for $M_W$ in the $W^+W^- \rightarrow q\bar{q}\ell\bar{\nu}$ channel for the data collected with the OPAL detector at the center-of-mass energy of $\sqrt{s} = 189$ GeV . . . . .	131



9.3	Combined results for $M_W$ in the $W^+W^- \rightarrow q\bar{q}\ell\bar{\nu}$ channel for the data collected with the OPAL detector at the center-of-mass energies of $\sqrt{s} = 183$ GeV and $\sqrt{s} = 189$ GeV . . . . .	133
9.4	Comparison of the results of the three W mass measurement methods in the $W^+W^- \rightarrow q\bar{q}\ell\bar{\nu}$ channel for the data collected with the OPAL detector at the center-of-mass energy of $\sqrt{s} = 183$ GeV . . . . .	141
9.5	Comparison of the results of the three W mass measurement methods in the $W^+W^- \rightarrow q\bar{q}\ell\bar{\nu}$ channel for the data collected with the OPAL detector at the center-of-mass energy of $\sqrt{s} = 189$ GeV . . . . .	142
9.6	Comparison of the measurement of the mass of the W boson in the $W^+W^- \rightarrow q\bar{q}\ell\bar{\nu}$ channel with the <i>Convolution method</i> with the results of the four LEP experiments at the center-of-mass energy of $\sqrt{s} = 183$ GeV . . . . .	144
9.7	Comparison of the measurement of the mass of the W boson in the $W^+W^- \rightarrow q\bar{q}\ell\bar{\nu}$ channel with the <i>Convolution method</i> with the results of the four LEP experiments at the center-of-mass energy of $\sqrt{s} = 189$ GeV . . . . .	144
9.8	Comparison of direct and indirect measurements of the mass of the W boson . . . . .	145
9.9	Comparison of the Standard Model predictions of the top and W masses with indirect and direct measurements . . . . .	145
A.1	Mass and pull distributions for the ensemble tests to estimate the improvement of the expected statistical error by applying the <i>Evil tau rejection</i> . . . . .	154
B.1	Difference of the event probability values of $W^+W^- \rightarrow q\bar{q}e\bar{\nu}$ and $W^+W^- \rightarrow q\bar{q}\mu\bar{\nu}$ events for different penalty functions . . . . .	158
B.2	Difference of the event probability values of $W^+W^- \rightarrow q\bar{q}\tau\bar{\nu}$ events for different penalty functions . . . . .	158
C.1	2C/1C fitted mass versus scaled hadronic mass for Monte Carlo events at center-of-mass energies of $\sqrt{s} = 183$ GeV and $\sqrt{s} = 189$ GeV . . . . .	162



# List of Tables

3.1	Quantum numbers of the fundamental fermions . . . . .	27
4.1	Decay widths and branching ratios of the W bosons to the different channels . . . . .	37
7.1	Efficiency matrix of the OPAL $W^+W^- \rightarrow q\bar{q}\ell\bar{\nu}$ selection at a center-of-mass energy of $\sqrt{s} = 189$ GeV . . . . .	68
8.1	Parameterization of the input of the kinematic fit routine for the different particle types . . . . .	91
8.2	Mean number of background events at $\sqrt{s} = 183$ GeV . . . . .	103
8.3	Mean number of background events at $\sqrt{s} = 189$ GeV . . . . .	104
8.4	Number of data events after consecutive cuts in the analysis at a center-of-mass energy of $\sqrt{s} = 183$ GeV . . . . .	106
8.5	Number of data events after consecutive cuts in the analysis at a center-of-mass energy of $\sqrt{s} = 189$ GeV . . . . .	106
8.6	Acceptance of the consecutive data quality cuts at a center-of-mass energy of $\sqrt{s} = 183$ GeV . . . . .	106
8.7	Acceptance of the consecutive data quality cuts at a center-of-mass energy of $\sqrt{s} = 189$ GeV . . . . .	106
8.8	Coefficients of the calibration functions at a center-of-mass energy of $\sqrt{s} = 183$ GeV . . . . .	111
8.9	Coefficients of the calibration functions at a center-of-mass energy of $\sqrt{s} = 189$ GeV . . . . .	111
8.10	Expected statistical error and pull width for the ensemble test at a center-of-mass energy of $\sqrt{s} = 183$ GeV . . . . .	115
8.11	Expected statistical error and pull width for the ensemble test at a center-of-mass energy of $\sqrt{s} = 189$ GeV . . . . .	116
8.12	Scaling factors for the study of detector calibration and simulation effects at a center-of-mass energy of $\sqrt{s} = 183$ GeV . . . . .	120
8.13	Systematic uncertainties for $M_W$ at the center-of-mass energy of $\sqrt{s} = 183$ GeV . . . . .	122
8.14	Systematic uncertainties for $M_W$ at the center-of-mass energy of $\sqrt{s} = 189$ GeV . . . . .	122

9.1	Number of selected data events at a center-of-mass energy of $\sqrt{s} = 183$ GeV . . . . .	126
9.2	Summary of the fit results for the data at $\sqrt{s} = 183$ GeV . . . . .	126
9.3	Summary of the applied corrections to the fitted W mass at $\sqrt{s} = 183$ GeV . . . . .	127
9.4	Number of selected data events at a center-of-mass energy of $\sqrt{s} = 189$ GeV . . . . .	129
9.5	Summary of the fit results for the data at $\sqrt{s} = 189$ GeV . . . . .	129
9.6	Summary of the applied corrections to the fitted W mass at $\sqrt{s} = 189$ GeV . . . . .	130
9.7	Mean number of events in a data-sized Monte Carlo subsample of $57 \text{ pb}^{-1}$ at $\sqrt{s} = 183$ GeV selected with the <i>Convolution method</i> . . . . .	135
9.8	Mean number of events in a data-sized Monte Carlo subsample of $183 \text{ pb}^{-1}$ at $\sqrt{s} = 189$ GeV selected with the <i>Convolution method</i> . . . . .	135
9.9	Comparison of the expected statistical errors of the three W mass extraction methods at OPAL at a center-of-mass energy of $\sqrt{s} = 183$ GeV . . . . .	136
9.10	Comparison of the expected statistical errors of the three W mass extraction methods at OPAL at a center-of-mass energy of $\sqrt{s} = 189$ GeV . . . . .	137
9.11	Systematic uncertainties and total expected error on the W mass of the three analysis methods at OPAL . . . . .	138
9.12	Comparison of the applied bias corrections for the <i>Breit-Wigner fit</i> and the <i>Convolution method</i> at a center-of-mass energy of $\sqrt{s} = 183$ GeV . . . . .	139
9.13	Comparison of the applied bias corrections for the <i>Breit-Wigner fit</i> and the <i>Convolution method</i> at a center-of-mass energy of $\sqrt{s} = 189$ GeV . . . . .	139
9.14	Comparison of the measured W mass of the three extraction methods at OPAL at a center-of-mass energy of $\sqrt{s} = 183$ GeV . . . . .	140
9.15	Comparison of the measured W mass of the three extraction methods at OPAL at a center-of-mass energy of $\sqrt{s} = 189$ GeV . . . . .	140
A.1	Expected statistical errors and pull widths in the $W^+W^- \rightarrow q\bar{q}\tau\bar{\nu}$ channel for the ensemble tests to estimate the influence of the <i>Evil tau rejection</i> . . . . .	154
D.1	Acceptance of the consecutive data quality cuts for signal and background events at $\sqrt{s} = 183$ GeV . . . . .	166
D.2	Acceptance of the consecutive data quality cuts for signal and background events at $\sqrt{s} = 189$ GeV . . . . .	166
E.1	Monte-Carlo samples used as background in the analysis at the center-of-mass energy of $\sqrt{s} = 183$ GeV . . . . .	169

E.2	Monte-Carlo signal samples used to determine the calibration functions at the center-of-mass energy of $\sqrt{s} = 183$ GeV . . . . .	169
E.3	Monte-Carlo samples used for systematic studies in the analysis at the center-of-mass energy of $\sqrt{s} = 183$ GeV . . . . .	170
E.4	Monte-Carlo samples used as background in the analysis at the center-of-mass energy of $\sqrt{s} = 189$ GeV . . . . .	170
E.5	Monte-Carlo signal samples used to determine the calibration functions at the center-of-mass energy of $\sqrt{s} = 189$ GeV . . . . .	170
E.6	Monte-Carlo samples used for systematic studies in the analysis at the center-of-mass energy of $\sqrt{s} = 189$ GeV . . . . .	171



# Chapter 1

## Introduction and Overview

The 20th century has proven to be the most successful yet for science.

In physics, several theoretical and experimental advances have deepened our level of understanding of how the universe came into being and how the inner parts of the world work—despite all pessimistic claims present late in the 19th century, that *“in physics, in principle, everything has already been investigated, there are only minor gaps to fill”* (Prof. Philipp von Jolly of Munich University to Max Planck, as the latter asked about the prospects of research in physics before beginning his studies).

The interplay between theoretical predictions, experimental discoveries and theoretical explanations is especially strong in the field of elementary particle physics which started out in 1928 with the theoretical prediction of antiparticles by Dirac in the first attempts to formulate a relativistic theory of quantum mechanics. This theory led to the realization that the non-relativistic quantum mechanics of single particles had to be abolished in favor of quantum field theory in which the number of particles is no longer constant. The actual discovery of positrons in cosmic rays by Anderson in 1932 opened the door to a world where particles could be created and annihilated at will. The subsequently formulated theory of electromagnetic interaction with matter, quantum electrodynamics—developed by Feynman, Schwinger and Dyson—is the most precisely tested theory in physics.

To investigate matter at an ever smaller scale and to create the newly found antimatter in the laboratory, the first accelerators were built and the field of high energy experimental physics, dedicated to the study of elementary particles and their interactions, was born.

Over the next decades, a flood of new particles (mesons and baryons) was discovered in accelerator experiments and cosmic rays. This complex picture of a particle zoo was then beautifully simplified by the introduction of the quark model by Gell-Mann, Ne’eman and Zweig in 1964, which reduced the number of over 100 known different particles of that time to three elementary quarks which can be arranged in pairs or triplets to form the spectrum of the observed hadrons, including protons and neutrons, the building blocks of the atomic nuclei. Experimental evi-

dence and theoretical considerations later led to the inclusion of three more quark species in the theory.

Almost at the same time as the introduction of the quark model, another theoretical breakthrough occurred with the unification of the electromagnetic and the weak forces by Glashow, Salam and Weinberg. Later work by 't Hooft and Veltman proved that the electroweak theory is in fact renormalizable.

Combining the electroweak theory with quantum chromodynamics, the theory of the strong interaction and quarks, the Standard Model of elementary particle physics was born. The whole world was reduced to three generations of elementary particles, each containing two leptons and two quarks, and twelve gauge bosons which mediate the electromagnetic, weak and strong forces. The Standard Model has proven to be extraordinarily successful and of great predictive power. Up to the present day no experimental evidence has been found to prove that this theory is wrong. After the discovery of the top-quark in 1995 at the Tevatron accelerator at Fermilab, only one particle predicted by the theory, the Higgs boson, which is responsible for the masses of the electroweak  $Z^0$  and  $W^\pm$  gauge bosons and the fermion masses, has stubbornly refused detection.

In parallel to the theoretical progress, the experimental aspect of elementary particle physics underwent great changes. Fixed target experiments with sluggish bubble chambers and photographic evaluation of the induced reactions gave way to colliding beam experiments with electronic readout and further to highly complex multipurpose detectors of the size of buildings and at the forefront of technological advancement. The ever increasing cost and the complexity of the experiments and machinery needed in high energy physics quickly led to the formation of international collaborations and to the centralization of accelerator facilities, even in the early days.

The CERN research center, situated near Geneva in Switzerland, is the leading laboratory for elementary particle physics in Europe, a joint venture of (nowadays) twenty member states. Since its creation in 1954, many important discoveries in the field of particle physics took place at CERN, among them the first direct observation of the electroweak gauge bosons, the  $Z^0$  and the  $W^\pm$  particles in 1983 at the Sp $\bar{p}$ S accelerator. In the last 10 years, CERN's LEP accelerator, a gigantic  $e^+e^-$  collider, and its four experiments ALEPH, DELPHI, L3 and OPAL, have provided the means for precision measurements of the Standard Model parameters, such as the  $Z^0$ -lineshape, and have led the search for the Higgs boson and new particles which would be evidence of necessary extensions of the Standard Model.

The W boson and the measurement of its mass—one of the fundamental parameters of the Standard Model—are the subject of this thesis. The mass measurement is performed in the  $W^+W^- \rightarrow q\bar{q}\ell\bar{\nu}$  decay channel with the OPAL detector at CERN.

The thesis is structured the following way: after this introduction, chapter 2 describes the LEP accelerator and the OPAL experiment, the two machines used to create and measure the data analyzed in this work. Chapter 3 provides a brief overview over the Standard Model of elementary particle physics, chapter 4 then



concentrates on the physics of the W-Boson at LEP. The different Monte Carlo generators, which were used for the simulation of physics events for statistical and systematical tests, are introduced in chapter 5. In chapter 6, the data flow from the individual events to the physics result is briefly outlined and a general overview of the analysis approach is provided. Chapter 7 describes the selection and the reconstruction of  $W^+W^- \rightarrow q\bar{q}\ell\bar{\nu}$  events; both are based on a general analysis framework, which is provided in a joint effort by members of the OPAL collaboration to simplify the first access to the data and the event selection and to place the different methods of analysis on a common ground. The analysis method used in this thesis to extract the mass of the W boson from the data, the *Convolution fit*, is described in detail in chapter 8. The *Convolution method* is then applied to the data collected in the years 1997 and 1998 and a combined result for the mass of the W boson in the  $W^+W^- \rightarrow q\bar{q}\ell\bar{\nu}$  channel for the center-of-mass energies of  $\sqrt{s} = 183$  GeV and  $\sqrt{s} = 189$  GeV is derived. The results of the data analysis are presented in chapter 9. Also included in chapter 9 is a comparison of the *Convolution method* with two alternative approaches to extract the W mass in this decay channel which are currently used within the OPAL collaboration. The last chapter, chapter 10, provides a summary of this thesis.



## Chapter 2

# LEP and OPAL

### 2.1 The Large Electron Positron Collider LEP



**Figure 2.1:** Aerial view of the European research center for elementary particle physics CERN. The position of the accelerators SPS (Super Proton Synchrotron) and LEP (Large Electron Positron Collider) with its four experiments ALEPH, DELPHI, L3, and OPAL has been added.

The Large Electron Positron collider at the European research center for elementary particle physics CERN near Geneva in Switzerland is currently the largest accelerator in the world. In a circular vacuum system of 27 km circumference, 100 m below the surface, bunches of electrons and positrons are accelerated to almost the speed of light in opposite directions and are collided at four interaction points. Around these interaction points the experiments ALEPH [1], DELPHI [2],

L3 [3], and OPAL [4] have been built to probe the debris of the  $e^+e^-$  collisions. Figure 2.1 shows an aerial view of the CERN research area and the position of the LEP accelerator.

A great advantage of  $e^+e^-$  accelerators compared to proton accelerators (as e.g. the Tevatron at Fermilab) is the missing inner structure of the primary interacting particles. The initial state of the reactions is therefore far better known which simplifies precision measurements. Furthermore, the whole center-of-mass energy, two times the beam energy, is available in the colliding electrons and positrons; in proton collisions only the part of the energy carried by the interacting partons is available, the rest is carried away by spectator particles.

The disadvantage of  $e^+e^-$  accelerators is the loss of energy that electrons and positrons experience through synchrotron radiation when forced on a circular path. This energy loss is proportional to  $1/m^4$  ( $m$  is the mass of the accelerated particle) and can be neglected for heavier particles like protons. The lost energy has to be restored each revolution by high frequency (RF) resonator cavities to the beam. For highly relativistic electrons and positrons of energy  $E$  the energy loss  $\Delta E$  on a circular trajectory of radius  $R$  is given by

$$\Delta E [\text{GeV}] = 8.85 \cdot 10^{-8} \frac{E^4 [\text{GeV}^4]}{R [\text{km}]}.$$
 (2.1)

For a beam energy of 100 GeV the energy loss of electrons and positrons in the LEP ring is about 2 GeV, or 2% of their total energy, per turn.

The radius of the accelerator and the technical design of the high frequency resonator cavities (as well as the available cooling power for superconducting cavities) limit the maximum achievable center-of-mass energy; for the LEP ring the upper limit is about 210 GeV.

Another important parameter of accelerators is the luminosity  $\mathcal{L}$ , which determines the event rate  $dN/dt$  as a function of the cross section  $\sigma(s)$  of a reaction:

$$\frac{dN}{dt} = \mathcal{L} \cdot \sigma(s),$$
 (2.2)

where  $s$  denotes the square of the center-of-mass energy.

For  $e^+e^-$  ring accelerators the luminosity  $\mathcal{L}$  is given by the number of bunches  $n$ , the number of electrons (positrons) per bunch  $N_{e^-}$  ( $N_{e^+}$ ), the revolution frequency  $f$  and the horizontal and vertical bunch cross sections  $\sigma_x^*$  and  $\sigma_y^*$  at the interaction point,

$$\mathcal{L} = \frac{n N_{e^+} N_{e^-} f}{4\pi \sigma_x^* \sigma_y^*}.$$
 (2.3)

In the year 1998, the LEP accelerator reached peak luminosities of about  $8 \cdot 10^{31} \text{ cm}^{-2} \text{ s}^{-1}$  at a center-of-mass energy of 189 GeV.

During the years 1989 to 1995, the LEP accelerator was running at a center-of-mass energy of  $\sqrt{s} \approx 91 \text{ GeV}$  in the vicinity of the  $Z^0$  resonance. About four and a

half million decays of the  $Z^0$  boson into fermion-antifermion pairs,  $e^+e^- \rightarrow Z^0 \rightarrow f\bar{f}$ , have been recorded by each experiment. This data made a precise measurement of the properties of the  $Z^0$  boson possible.

In June 1996, after an upgrade of the accelerator with superconducting RF cavities, the so called LEP2 period started with a center-of-mass energy of  $\sqrt{s} \approx 161$  GeV; the center-of-mass energy was subsequently increased during the following years and has reached a value of  $\sqrt{s} \approx 210$  GeV in the year 2000.

The motivation for an increase of the center-of-mass energy is, on the one hand, the search for *new physics*, here the search for the Higgs boson and particles predicted by extensions of the Standard Model, as e.g. Supersymmetry, play an important role; on the other hand, increasing the center-of-mass energy above two times the mass of the W boson ( $\sqrt{s} > 160$  GeV) allows the pair production of these particles. The upgraded LEP accelerator therefore enables the physicists to study all electroweak heavy gauge bosons in precision measurements.

The year 2000 will be the last year for LEP; after the end of data taking in November 2000, the accelerator and its experiments will be dismantled to make way for the construction of the next accelerator, the Large Hadron Collider (LHC). Beginning in 2005, the LHC—a proton proton collider with a center-of-mass energy of 14 TeV—and its two multipurpose experiments ATLAS [5] and CMS [6] will push back the frontiers and will open up new realms of elementary particle physics.

## 2.2 The OPAL Detector

OPAL (Omni Purpose Apparatus at LEP) is one of the four experiments at the Large Electron Positron collider. The task of the detector is the identification and the measurement of the momentum and the energy of the particles produced in the  $e^+e^-$  collisions.

Figure 2.2 shows a three-dimensional schematic view of the experiment and its components; its structure is typical for a modern collider detector. The detector is built of many subsystems, but can be divided into three major parts: the inner tracking system, the calorimeters and the muon system. Due to the cylindrical geometry, which is a compromise between maximum coverage of the solid angle around the interaction point and simple design and magnetic field geometry, most subsystems are divided in a barrel part and endcaps. The detector has a length of 12 m and a diameter of 10 m.

A detailed description of the OPAL experiment can be found in [4]. The following sections only briefly describe the central and, for this analysis, most important components of the detector, starting at the innermost parts and continuing to the outer parts.

To describe the data taken with the OPAL detector a right-handed Cartesian coordinate system is used. The z-axis is defined by the direction of the electron beam, the x-axis points to the center of the LEP ring and the y-axis points perpendicu-

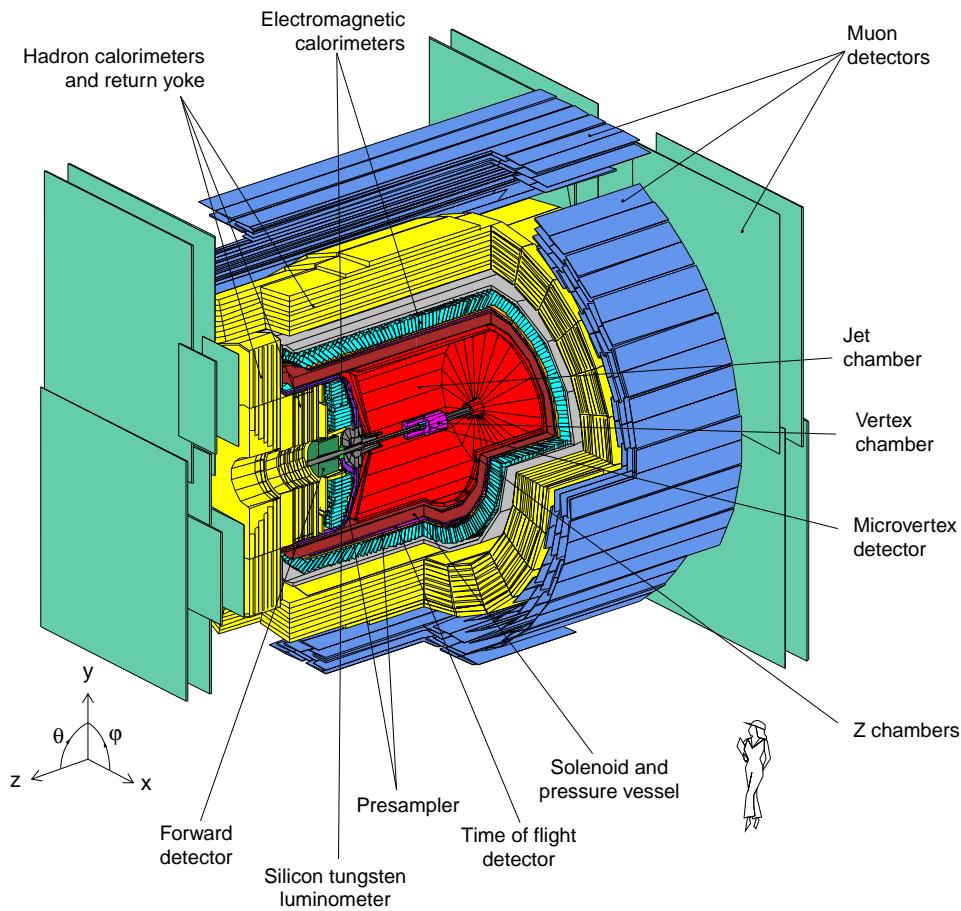


**Figure 2.2:** Three dimensional schematic view of the OPAL detector.

lar upward from the  $x$ - $z$  plane. Instead of Cartesian coordinates, tracks measured in the detector are often parameterized in polar coordinates, the polar angle  $\theta$  is counted from the  $z$ -axis, the azimuthal angle  $\phi$  from the  $x$ -axis.

### 2.2.1 The Tracking System

The central tracking system is used to measure the momentum of charged particles which traverse the subdetectors. The tracking system is immersed in a cylinder symmetric magnetic field of 0.435 T oriented along the  $z$ -axis, which is created by a solenoid which encompasses the Jet chamber.

The innermost detector is the Microvertex detector which is built directly around the beam pipe in the vicinity of the interaction point. It consists of silicon microstrip counters. The Microvertex detector is primarily used to measure secondary vertices, e.g. of  $b$ -meson decays.

The Vertex detector, a cylindrical drift chamber of 100 cm length and a diam-

eter of 47 cm, allows the precise measurement of tracks in the  $r$ - $\phi$  plane and the determination of the  $z$ -coordinate via stereo cells.

The heart of the tracking system is the Jet chamber, a drift chamber which is 400 cm long and has a diameter of 370 cm. The Jet chamber consists of 24 sectors with 159 axial signal wires each and is filled with an argon/methan/isobutane gas mixture at 4 bar.

The reconstruction of tracks in drift chambers is based on the ionization of the chamber gas by the traversing charged particles and on a measurement of the drift time of the liberated electrons to the signal wires which are kept at a positive high voltage [7]. Particle momenta can be then determined from the curvature of the reconstructed tracks in the magnetic field.

The Jet chamber is not only used for a precise momentum measurement, but also allows a particle identification via the measurement of the specific energy loss  $dE/dx$  (which is proportional to the number of liberated charge carriers per unit length and depends on the velocity and charge of the ionizing particle).

The drift chambers are complemented by the encompassing Z-chambers, which precisely measure the  $z$ -component and therefore the polar angle  $\theta$  of the tracks of charged particles as they leave the Jet chamber.

The tracking system achieves a momentum resolution<sup>1</sup> of

$$\frac{\sigma_{p_T}}{p_T} = \sqrt{(0.02)^2 + (0.0015 p_T [\text{GeV}])^2}, \quad (2.4)$$

where  $p_T$  denotes the transverse momentum, i.e. the momentum in the  $x$ - $y$  plane. The average angular resolution is about 0.3 mrad in  $\phi$  and 1 mrad in  $\theta$ .

The Time-of-Flight detector (TOF), situated after the tracking system and the magnet coil, is built of 160 scintillators (650 cm long by 9 cm wide). Traversing charged particles excite the scintillator material and lead to the emission of photons which are measured by photomultipliers at both ends of the TOF bars. In conjunction with a beam crossing signal, the TOF allows the measurement of the flight time of charged particles from the interaction point to this subdetector. The Time-of-Flight detector, with its fast response, is a major part of the trigger system of the OPAL detector. The measurement of the time of flight and the pulse height of the produced signals can be used for a charged particle identification in the momentum range of 0.6–2.5 GeV.

### 2.2.2 The Calorimeters

The calorimeter system follows the central detectors and is used in the energy measurement of charged and neutral particles. Unlike the tracking chambers, which are low density position measuring devices used to determine charged particle momenta and directions, the calorimeters are designed as total absorption detectors aimed to stop all impinging particles. As the interaction mechanism of particles

<sup>1</sup>Throughout this thesis we will use  $c = 1$  and  $\hbar = 1$ ; thus masses and momenta will be measured in GeV.

with matter depends on whether they are subject to the strong force or not, the calorimeter system consists of two subdetectors: the electromagnetic calorimeter and the hadron calorimeter.

The electromagnetic calorimeter (ECAL) encloses the magnet and is used for the identification and the energy measurement of electrons, positrons and photons. It is built as a homogeneous calorimeter of about 10000 lead glass blocks; the segmentation of the calorimeter also allows the measurement of the track angles and the matching of clusters with the tracking information taken from the inner drift chambers. To this purpose the lead blocks are pointing towards the interaction region in the barrel part; in the endcaps they are parallel to the z-axis.

Electrons and photons create an electromagnetic shower of photons and electron-positron pairs in the high-Z material of the lead glass blocks through an interplay of bremsstrahlung and pair creation<sup>2</sup>. The energy measurement in the calorimeter is based on the number and the pulse height of the Cherenkov photons produced by the relativistic electron and positrons in the shower. The Cherenkov light is measured by photomultipliers connected to the lead glass blocks.

The extension of at least 22 radiation lengths of the ECAL ensures that the electromagnetic showers are always contained within the calorimeter.

The electromagnetic calorimeter achieves an intrinsic energy resolution of

$$\frac{\sigma_E}{E} = 0.2\% + \frac{6.3\%}{\sqrt{E[\text{GeV}]}} \quad (2.5)$$

in the barrel region and

$$\frac{\sigma_E}{E} = \frac{5\%}{\sqrt{E[\text{GeV}]}} \quad (2.6)$$

in the endcaps.

Situated in front of the electromagnetic calorimeter, there are already about two radiation lengths of material which are primarily made up by the magnet coil and the pressure tank for the Jet chamber. Electromagnetic showers can therefore start before the particles actually reach the calorimeter. A Presampler, built of Limited-Streamer tubes and mounted between the TOF detector and the electromagnetic calorimeter is used to measure the position and charged multiplicity of electromagnetic showers as they enter the ECAL. These measurements are used to derive energy corrections in order to improve the energy resolution of the ECAL. Thus, compared to the intrinsic resolution, the effective resolution of the electromagnetic calorimeter is degraded only by a factor of approximately  $2/\sin \theta$ . The Presampler also improves the  $\gamma/\pi^0$  discrimination.

The hadron calorimeter (HCAL) surrounds the electromagnetic calorimeter. It is built as a sampling calorimeter with interleaved layers of active and passive material, and is used for the energy measurement of hadrons. The passive layers of the

<sup>2</sup>Both, bremsstrahlung and pair creation are enhanced in material with a high nuclear charge number  $Z$ . Choosing such material allows the construction of more compact electromagnetic calorimeters.



HCAL are formed by the iron return yoke of the solenoid magnet, the active layers consist of Streamer chambers. The impinging hadrons lose their energy in inelastic collisions with the heavy nuclei of the passive calorimeter material, producing secondary hadrons and thus initiating a hadronic shower. A hadronic shower also contains an electromagnetic shower component induced by the decay of e.g.  $\pi^0$  mesons<sup>3</sup>. The hadron calorimeter has a radial extension of four interaction lengths. Compared to the electromagnetic calorimeter, the resolution is much reduced—due to the larger fluctuations present in hadronic showers—and reaches only

$$\frac{\sigma_E}{E} \approx \frac{120\%}{\sqrt{E[\text{GeV}]}}. \quad (2.7)$$

### 2.2.3 The Muon System

The OPAL detector is completed by the muon system, which is used to identify muons. Apart from the undetectable neutrinos, muons are the only particles that are not stopped in the calorimeters. The muon system consists of four layers of planar drift chambers in the barrel region and Limited-Streamer tubes in the endcaps. The direction of a muon track can be determined from the hit coordinates in the individual layers. Muons created in the initial processes of the  $e^+e^-$  collisions can be distinguished from secondary muons—produced in the shower processes in the calorimeters—and cosmic muons by comparing the hits in the muon chambers with the information provided by the central tracking system.

### 2.2.4 The Forward Detector and the SiW Luminometer

The luminosity delivered by the LEP accelerator to the OPAL experiment is determined by measuring the event rate of small angle Bhabha scattering,  $e^+e^- \rightarrow e^+e^-$ . The cross section of this process can be calculated very precisely using quantum electrodynamics and a measurement of the event rate then yields the luminosity according to equation (2.2).

The measurement of Bhabha events is performed by the forward detector—a set of sampling calorimeters and drift tubes—and the silicon tungsten luminometer—a sampling calorimeter.

At the center-of-mass energies of  $\sqrt{s} = 183 \text{ GeV}$  and  $\sqrt{s} = 189 \text{ GeV}$ , at which the data analyzed in this thesis was recorded, the error on the luminosity is dominated by theoretical uncertainties in the calculation of the cross section and is smaller than 0.5%.

---

<sup>3</sup>The energy measurement is made in combination with the electromagnetic calorimeter, since the ECAL constitutes already two interaction lengths of material, so that hadronic showers can start before the HCAL.



## Chapter 3

# The Standard Model

The Standard Model forms the theoretical foundation of elementary particle physics. All matter is built of only twelve fundamental fermions (spin 1/2 particles): six leptons and six quarks, which can be arranged in 3 generations of two leptons and two quarks—and their antiparticles—each. The first generation consists of the electron (e), the electron neutrino ( $\nu_e$ ) and the up (u) and down (d) quarks, the second generation of the muon ( $\mu$ ), the muon neutrino ( $\nu_\mu$ ) and the charm (c) and strange (s) quarks, and the third generation of the tau ( $\tau$ ), the tau neutrino ( $\nu_\tau$ ) and the top (t) and bottom (b) quarks.

Interactions between the elementary particles are described by the exchange of twelve bosons (spin 1 particles). The electromagnetic force is mediated by the massless photon ( $\gamma$ ), the weak force by the massive  $Z^0$  and  $W^\pm$  bosons. Eight massless bosons, the gluons (g), mediate the strong force.

The theory also requires the existence of another scalar particle, the Higgs boson (H), to give rise to the masses of the  $Z^0$  and  $W^\pm$  bosons in a mechanism called *spontaneous symmetry breaking*. Fermion masses can be introduced in a natural way by Yukawa-couplings to the Higgs boson as well. So far, the Higgs boson has not been observed directly<sup>1</sup>.

There is no principal difference between the three generations, except for the masses of their constituents. The stable massive matter which forms the observable universe consists entirely of fermions of the first family (except for neutron stars where under the high gravitational pressure particles of higher generation may exist).

The theory of the Standard Model is based on the principle of local gauge invariance; the Lagrangian is invariant under local transformations of certain symmetry groups. For the electromagnetic force this symmetry group is  $U(1)$ , for the weak force  $SU(2)$ , and for the strong force  $SU(3)$ . The invariance of the Lagrangian under symmetry operations leads to associated conserved quantum

---

<sup>1</sup>From this fact a lower limit on the mass of the Standard Model Higgs boson can be calculated. The current preliminary value, as determined from the data collected by the four LEP experiments up to a center-of-mass energy of 209 GeV, is  $M_H > 113.3$  GeV with a confidence level of 95% [8].

numbers.

The Standard Model does not include the gravitational force, as there is yet no satisfying quantum theory of gravitation. As the gravitational force is very weak compared to the other three forces, it can be neglected in the description of elementary particle physics—but it still governs the universe at large scales.

### 3.1 Electroweak Theory

Even before the advent of the Standard model there was a gauge invariant field theory of electromagnetism, the theory of quantum electrodynamics (QED). It is based on the  $U(1)_{\text{em}}$  symmetry group which leads to the conservation of the charge quantum number; the local gauge invariance also necessitates the introduction of an associated massless vector field, the photon. Alas, the formulation of a gauge invariant theory of the weak force ran into severe problems with the renormalization of the theory.

Glashow, Salam, and Weinberg formulated a unification of the electromagnetic and the weak force which was later proven to be renormalizable by 't Hooft and Veltman.

This electroweak theory is based on the symmetry group  $SU(2)_L \times U(1)_Y$ , which reflects the experimental evidence that the fundamental fermions are arranged in three generations of left handed doublets and right handed singlets<sup>2</sup>. The  $SU(2)_L$  part couples only to left handed fermions, while the  $U(1)_Y$  part couples to left and right handed fermions. The individual fermions are characterized by their quantum numbers weak isospin  $I$ , its third component  $I_3$ , and the weak hypercharge  $Y$ , see table 3.1. The charge  $Q$  of the fermion is given by the Gell-Mann-Nishijima relation

$$Q = I_3 + Y. \quad (3.1)$$

Neutrinos (antineutrinos) exist, at the present state of knowledge, only in left (right) handed form and are considered massless. The weak eigenstates  $d'$ ,  $s'$ ,  $b'$  of the quarks are linear combinations of the mass eigenstates  $d$ ,  $s$ ,  $b$ ; the transformation is described by the Cabbibo-Kobayashi-Maskawa-Matrix  $V$ . In the leptonic sector no such mixing between generations occurs as long as the neutrinos are massless.

The electroweak theory with the unbroken  $SU(2)_L \times U(1)_Y$  symmetry postulates the existence of four spin 1 vector bosons, a triplet associated with the  $SU(2)$  group,  $W_\mu^{1,2,3}$ , and a singlet associated with the  $U(1)$  group,  $B_\mu$ . All these vector bosons are massless, hence the theory would predict an infinite range for the weak interaction, in clear violation with the experimental evidence of a range of less than  $10^{-14}$  m.

---

<sup>2</sup>It should be noted that a priori there is *no unique* way to construct the model of electroweak interactions from first principles; experimental data must be used to discriminate between several possible gauge theories.

Fermions			$I$	$I_3$	$Y$
Leptons					
$\begin{pmatrix} \nu_e \\ e^- \end{pmatrix}_L$	$\begin{pmatrix} \nu_\mu \\ \mu^- \end{pmatrix}_L$	$\begin{pmatrix} \nu_\tau \\ \tau^- \end{pmatrix}_L$	1/2	1/2	-1/2
$e^-_R$	$\mu^-_R$	$\tau^-_R$	1/2	-1/2	-1/2
$e^-_R$	$\mu^-_R$	$\tau^-_R$	0	0	-1
Quarks					
$\begin{pmatrix} u \\ d' \end{pmatrix}_L$	$\begin{pmatrix} c \\ s' \end{pmatrix}_L$	$\begin{pmatrix} t \\ b' \end{pmatrix}_L$	1/2	1/2	1/6
$u_R$	$c_R$	$t_R$	1/2	-1/2	1/6
$d'_R$	$s'_R$	$b'_R$	0	0	2/3
$d'_R$	$s'_R$	$b'_R$	0	0	1/3

**Table 3.1:** Quantum numbers of the fundamental fermions.

To remedy this stigma, the mechanism of *spontaneous symmetry breaking*<sup>3</sup> is used to give mass—and therefore a finite range—to the three weak gauge bosons while leaving the electromagnetic subgroup  $U(1)_{\text{em}}$  unbroken. In the Minimal Standard Model, a  $SU(2)$  doublet of complex scalar Higgs fields,

$$\phi = \begin{pmatrix} \phi^+ \\ \phi^0 \end{pmatrix} \quad (3.2)$$

with hypercharge  $Y = 1/2$ , which couples to the electroweak gauge bosons and has a non-vanishing vacuum expectation value, is sufficient for this purpose. The self-interactions of the Higgs field is described by the potential

$$V(\phi) = -\mu^2 \phi^\dagger \phi + \frac{\lambda}{4} (\phi^\dagger \phi)^2, \quad (3.3)$$

where  $\mu$  and  $\lambda$  are free parameters; the vacuum expectation value of  $\phi$  is then given by

$$v = \frac{2\mu}{\lambda}, \quad (3.4)$$

the ground state itself is infinitely degenerated.

By selecting an appropriate ground state of the Higgs doublet and exploiting the freedom of a gauge transformation, three of the four Higgs fields vanish—they become so-called Goldstone bosons—and their degrees of freedom are absorbed

<sup>3</sup>The term *spontaneous symmetry breaking* is used if the ground state of a system does not exhibit the symmetry of its underlying Lagrangian.

in the vector fields of the now massive gauge bosons. Only one component of the Higgs doublet remains free, the massive neutral scalar Higgs boson  $H$  of the Standard Model.

The observed physical gauge bosons of the broken electroweak theory are orthogonal linear combination of the original bosons and correspond to the massless photon of the  $U(1)_{\text{em}}$  group and the three massive  $Z^0$  and  $W^\pm$  bosons of the weak force:

$$A_\mu = \sin(\theta_W)W_\mu^3 + \cos(\theta_W)B_\mu \quad (3.5)$$

$$Z_\mu = \cos(\theta_W)W_\mu^3 - \sin(\theta_W)B_\mu \quad (3.6)$$

$$W_\mu^\pm = \frac{1}{\sqrt{2}} (W_\mu^1 \mp W_\mu^2). \quad (3.7)$$

Here  $\theta_W$  denotes the *weak mixing angle*.

The masses of the physical vector bosons are given by the gauge couplings  $g_1$  and  $g_2$  of the  $U(1)$  and  $SU(2)$  groups, respectively, and the vacuum expectation value  $v$  of the Higgs field,

$$M_\gamma = 0, \quad (3.8)$$

$$M_Z = \frac{1}{2} \sqrt{g_1^2 + g_2^2} v, \quad (3.9)$$

$$M_W = \frac{1}{2} g_2 v. \quad (3.10)$$

From equations (3.9) and (3.10), it can be seen that the masses of the  $Z^0$  and  $W^\pm$  bosons are related by the coupling constants of the symmetry groups alone, the dependence on the Higgs parameters cancels out. The weak mixing angle  $\theta_W$ , better known as the Weinberg angle, is defined by the coupling constants of the  $U(1)$  and  $SU(2)$  groups, but can also be expressed as the ratio of the mass of the charged gauge boson  $W^\pm$  to the mass of the neutral gauge boson  $Z^0$ ,

$$\cos \theta_W = \frac{g_2}{\sqrt{g_1^2 + g_2^2}} = \frac{M_W}{M_Z}. \quad (3.11)$$

To simplify the comparison with experimentally measurable quantities it is often convenient to express the theoretical parameters

$$g_1, g_2, \lambda, \mu$$

by the equivalent physical parameters

$$e, G_F, M_Z, M_H$$

where  $e$  is the electric charge,  $G_F$  is the Fermi constant and  $M_H$  the mass of the Higgs boson. The following relations (in lowest order perturbation theory,  $\alpha$  is the finestructure constant) can be used to transform the variables:

$$e = \frac{g_1 g_2}{\sqrt{g_1^2 + g_2^2}}, \quad M_W = \sqrt{\frac{\pi \alpha}{\sqrt{2} G_F}} \frac{1}{\sin \theta_W}, \quad M_H = \sqrt{2} \mu.$$

## 3.2 Quantum Chromodynamics

The strong interaction is described by the theory of quantum chromodynamics (QCD). From the fundamental fermions only the quarks participate in the strong interaction.

In analogy to the theory of quantum electrodynamics, the concept of a color charge was introduced to describe the strong interaction. In contrast to the QED, which needs only one charge and one neutral gauge boson, the photon, the QCD requires three color charges (commonly referred to as red, green and blue) and eight gluons as mediating bosons, which carry a combination of color and anticolor charge. As a result of their color charge the gluons themselves are subject to the strong force and can interact with each other.

The underlying symmetry group for the theory of quantum chromodynamics is the  $SU(3)_C$  group of color symmetry. Since the gauge bosons of the theory, the gluons, are massless, the physical instances are described directly by the fields associated with the  $SU(3)_C$  group and the only free parameter of the theory is the coupling constant  $\alpha_s$ .

The non-abelian structure of the  $SU(3)$  group and the resulting self-interaction of its gauge bosons, together with the vanishing gluon masses, has severe implications within the theory: the energy dependence of the coupling constant, the *running* of  $\alpha_s$ , is different from the QED case. The coupling constant  $\alpha_s$  becomes greater with increasing distance between the color charges, which means that the forces between quarks and gluons get stronger as they are separated further from each other. This behavior ultimately leads to the so called *confinement*: isolated particles carrying a color charge cannot exist. As the color charges are separated further and further from each other, the energy density between them becomes large enough that quark-antiquark pairs or gluons can be created, thus leading to the so-called *fragmentation* of the original particles. On the other hand, the coupling gets smaller with decreasing distance, a phenomenon called *asymptotic freedom*, which allows the application of perturbation theory in QCD at high momentum transfers.

The observed hadrons must be color neutral (white) and can be built by either combining a quark and antiquark in the case of mesons, or by combining three quarks in the case of baryons.







## Chapter 4

# Physics of W Boson Pairs at LEP2

This chapter provides an introduction to the physics of W-pairs at LEP2. A brief overview of the properties of the W boson is followed by a description of the mechanism of the W-pair production at LEP2 and four-fermion processes of which the W-pair production forms a subset. The main non four-fermion background class, the two-fermion processes, which are important for the measurement of the mass  $M_W$  of the W boson, are then described, before we briefly enter the realm of final state interactions. The chapter closes with a classification scheme of W-pair events based on their decay modes and discusses the merits and disadvantages of each event class with respect to the measurement of the W mass.

### 4.1 The W Boson

The W boson is one of the massive gauge bosons mediating the weak force in the scope of the Standard Model. It was discovered at the Sp $\bar{p}$ S accelerator at CERN by the experiments UA1 and UA2 in proton antiproton collisions in 1983, where its mass was measured for the first time [9, 10].

#### 4.1.1 The W Mass

After very accurate measurements of the  $Z^0$  boson lineshape during the LEP1 era, at LEP2 finally the mass  $M_W$  of the W boson became accessible to precision measurements in  $e^+e^-$  collisions. The interrelation of the Standard Model parameters makes precision measurements extremely worthwhile: not only is one parameter determined with high accuracy, but estimates for quantities that are difficult or impossible to measure directly can be also improved and the self-consistency of the theory can be verified.

The mass  $M_W$  of the W boson is given in the *on-shell-scheme* by [11]

$$M_W^2 = \frac{\pi \alpha}{\sqrt{2} G_F \sin^2 \theta_W} \frac{1}{1 - \Delta r}, \quad (4.1)$$

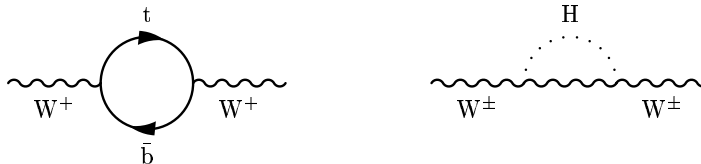


**Figure 4.1:** Feynman diagrams of 1-loop corrections to the W propagator mediated through the top-quark (left) and the Higgs boson (right).

where  $\theta_W$  is the Weinberg angle,  $G_F$  the Fermi constant and  $\alpha$  the finestructure constant; the factor  $\Delta r$  is 0 at *tree level* (i.e. lowest order perturbation theory, also called *Born level*) and depends on the mass of the top quark and the Higgs mass when loop corrections are included in the W propagator. Figure 4.1 shows two contributing Feynman diagrams for 1-loop correction on the W propagator. The direct determination of the W mass therefore allows, together with a measurement of the top mass, to estimate the mass of the—up to now unobserved—Higgs boson. A high precision in the measurement of  $M_W$  is needed, as the loop corrections on the mass of the W boson depend only on the logarithm of the Higgs mass.

Using global fits to the Standard Model, the W mass can be estimated with very high precision from the numerous measurements of the other Standard Model parameters. From these fits a value of

$$M_W = 80.386 \pm 0.025 \text{ GeV} \quad (4.2)$$

is obtained [12]. The direct measurement of the W mass, especially when it has a comparable precision as the global Standard Model fit, is an important cross-check of the self-consistency of the theory. The final combined LEP result on the W mass from ALEPH, DELPHI, L3 and OPAL after the end of data taking in November 2000 will reach this precision [11] and play an important role in these tests. At the present time, the combined value from all direct measurements of the W mass at the Sp̄pS, Tevatron, and LEP colliders is given as [12]

$$M_W = 80.436 \pm 0.037 \text{ GeV}. \quad (4.3)$$

Figure 4.2 shows a comparison of the direct and indirect measurements of the mass of the W boson and the top quark mass with the predictions of the Standard Model for different masses of the Higgs boson for the data collected up to the year 1997<sup>1</sup>. The intersection of the confidence levels of these measurements with the yellow (light grey) band allows the derivation of limits on the Higgs bo-

<sup>1</sup>A more recent comparison can be found as figure 9.8 on page 145 in chapter 9.

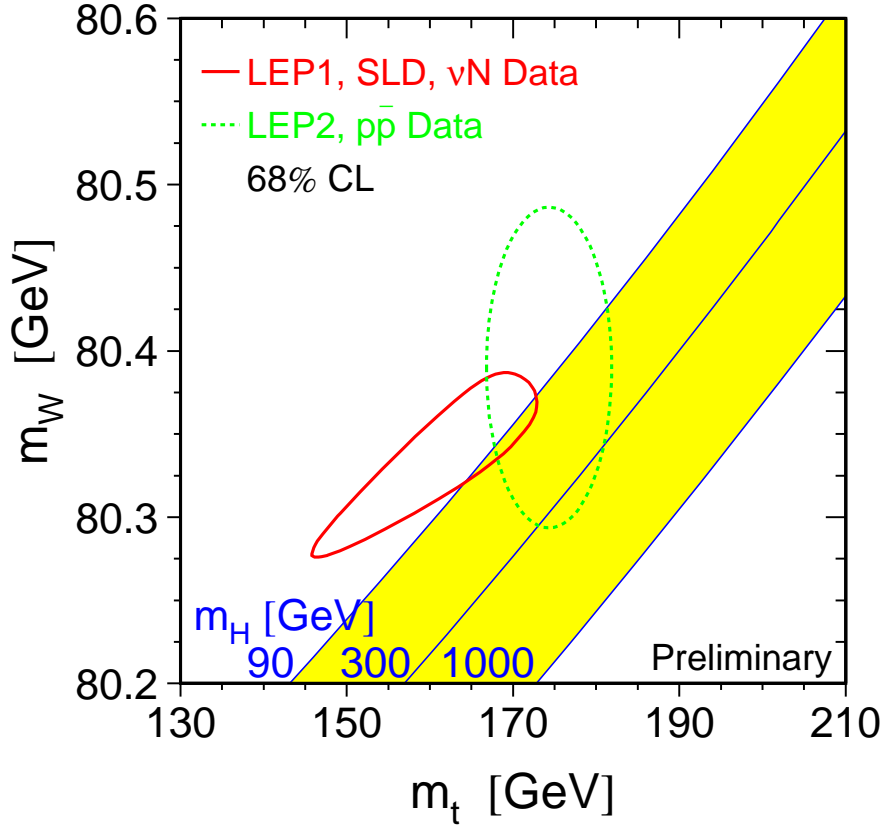


**Figure 4.2:** Comparison of the Standard Model predictions of the top and W masses with indirect (LEP1, SLD,  $\nu N$ ) and direct measurements (LEP2,  $p\bar{p}$ ) in 1997 [13]. The indirect measurements are obtained from a fit to electroweak precision data. The yellow (light grey) area shows the Standard Model prediction for a range of the Higgs mass.

son mass. The lower limit of 90 GeV on the Higgs mass was set by (unsuccessful) direct searches.

#### 4.1.2 The W Width

The width  $\Gamma_W$  of the W boson is determined by its couplings to the fundamental fermions. As the parameters of the Standard Model are highly interrelated, it can be derived from the W mass. In the leptonic decay, the W boson couples to each generation of the lepton-neutrino pairs individually, the decay modes are  $W \rightarrow e\nu_e$ ,  $W \rightarrow \mu\nu_\mu$ , and  $W \rightarrow \tau\nu_\tau$ . In the hadronic decay, the W boson couples to u- and d-like quarks. The weak eigenstates of the d-like quarks are linear combinations of the d, s, b quarks and a mixing between the three generations occurs which is described by the Cabbibo-Kobayashi-Maskawa (CKM) matrix  $V$ .

Within the *Born level* approximation, and neglecting the fermion masses, the partial width for a decay of a W boson to a pair of fermions  $f_i \bar{f}'_j$  is given by

$$\Gamma_W^{\text{Born}}(f_i \bar{f}'_j) = \frac{\alpha}{12 \sin \theta_W} M_W \begin{cases} 1 & \text{for leptons,} \\ N_C |V_{ij}|^2 & \text{for quarks,} \end{cases} \quad (4.4)$$

where  $\theta_W$  denotes the Weinberg angle,  $\alpha$  the finestructure constant,  $N_C = 3$  the number of different color charges and  $V_{ij}$  the elements of the CKM matrix. The decay of a W boson to a final state containing a top quark is kinematically forbidden, since the top quark has approximately two times the mass of the W boson. Therefore only six different hadronic decays contribute to the W width of which four are suppressed due to the small size of the off-diagonal elements of the CKM matrix.

The dominant decay modes of the W boson are  $W \rightarrow e \nu_e$ ,  $W \rightarrow \mu \nu_\mu$ ,  $W \rightarrow \tau \nu_\tau$ ,  $W \rightarrow ud$ , and  $W \rightarrow cs$ . Neglecting other contributions, we arrive at a first approximation of the W width of

$$\Gamma_W \approx (3 + 2 \times 3) \frac{\alpha}{12 \sin^2 \theta_W} M_W = 3 \frac{\alpha}{4 \sin^2 \theta_W} M_W. \quad (4.5)$$

Electroweak loop corrections can be more easily accounted for by parameterizing the lowest-order width in terms of  $G_F$ ,  $M_Z$ , and  $M_W$  instead of  $\sin \theta_W$  and  $\alpha$ . In this parameterization the electroweak corrections depend in a negligible way on the mass of the Higgs boson and remain below 0.5% of the total width. Furthermore the QCD radiative corrections for the hadronic decay modes are practically constant and equal to  $2 \alpha_s (M_W^2) / 3 \pi$ . The total width of the W boson with the improved Born approximation is then given by [11]

$$\Gamma_W \approx \frac{G_F M_W^3}{2 \sqrt{2} \pi} \left( 1 + \frac{2 \alpha_s (M_W^2)}{\pi} \right), \quad (4.6)$$

where  $\alpha_s$  denotes the strong coupling constant.

The experimental determination of the width of the W boson proves to be extremely difficult, since the measured width is given by the convolution of the natural width and the detector resolution. Both are of comparable size and any uncertainty in the detector resolution directly affects the determination of  $\Gamma_W$ .

The most precise direct measurement of  $\Gamma_W$  was performed by the four LEP experiments, yielding a value of [14]

$$\Gamma_W = 2.12 \pm 0.11 \text{ GeV}. \quad (4.7)$$

At present, the best value of  $\Gamma_W$  is given by the CDF and D0 collaborations, but it is derived from an indirect measurement in which the W width is determined by a

comparison with the well known  $Z^0$  width. The result of this indirect measurement is [13]

$$\Gamma_W = 2.043 \pm 0.092 \text{ GeV}. \quad (4.8)$$

The branching ratios have been measured with a precision of about 1–4% and are consistent with the Standard Model expectations, see table 4.1.

Process	Decay Width / GeV		Branching Ratio	
	Theoretical Exp.	Measured	Theoretical Exp.	Measured [15]
$W \rightarrow q\bar{q}$	1.4104	—	0.6751	$0.685 \pm 0.006$
$W \rightarrow e\nu_e$	0.2262	—	0.1083	$0.107 \pm 0.002$
$W \rightarrow \mu\nu_\mu$	0.2262	—	0.1083	$0.105 \pm 0.003$
$W \rightarrow \tau\nu_\tau$	0.2262	—	0.1082	$0.104 \pm 0.004$
$W \rightarrow f\bar{f}'$	2.0891	$2.12 \pm 0.11^a$ $2.04 \pm 0.09^b$	—	—

**Table 4.1:** Decay widths and branching ratios of the W bosons to the different channels. The experimental result of the W width quotes the values for the indirect and direct measurements.

<sup>a</sup>direct measurement [14]

<sup>b</sup>indirect measurement [13]

### 4.1.3 Gauge Boson Couplings

The W boson not only couples to the fundamental fermions, but—due to the non-abelian structure of the Standard Model—also to the other electroweak gauge bosons and to the Higgs boson as well.

The triple gauge boson couplings  $WWZ^0$  and  $WW\gamma$  are of the Yang-Mills form. This specific form leads to a proper high energy behavior of the W-pair cross section and is essential for the renormalization of the Standard Model. Anomalous couplings, different from the Yang-Mills form, generally lead to a rising high energy cross section and a violation of unitarity. At LEP2, the center-of-mass energy is too low to observe the possible deviating high energy behavior, but limits on anomalous triple gauge boson couplings can be established by the precise measurement of the W-pair production cross section  $\sigma_{WW}(s)$  as a function of the center-of-mass energy  $\sqrt{s}$  (as an example, see figure 4.5 on page 40 for the effects of the absence of the  $WWZ^0$  coupling on this cross section) or a measurement of the angular distribution of the W bosons and their decay products; especially the angular distribution in the W-production angle is sensitive to non-standard couplings.

All results of the triple boson coupling constants obtained so far with the OPAL detector are consistent with their Standard Model predictions [16, 17].

## 4.2 Pair Production of W Bosons

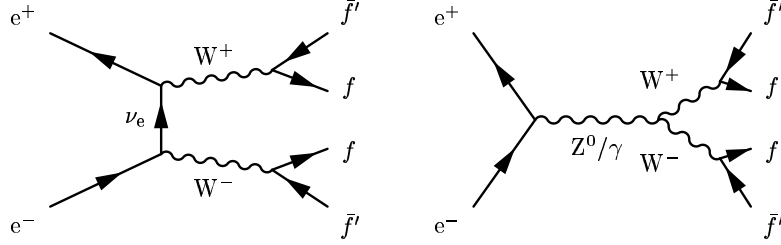


**Figure 4.3:** Lowest order Feynman diagrams for  $e^+e^- \rightarrow W^+W^- \rightarrow 4f$ .

The pair production of W bosons in  $e^+e^-$  collisions is possible as soon as the center-of-mass energy exceeds a threshold of two times the mass of the W boson ( $\sqrt{s} > 2 M_W \approx 161$  GeV). At tree level only three diagrams contribute to the W-pair production, compare figure 4.3. Following the notation of [11], this set of diagrams is referred to as CC03<sup>2</sup>.

The first diagram, mediated by a neutrino exchange, is called a t-channel diagram and belongs to the class of abelian diagrams, the other two diagrams, mediated through a  $Z^0$  boson or  $\gamma$ , are called s-channel diagrams and belong, due to the presence of a triple gauge boson vertex, to the non-abelian class of diagrams. The t-channel diagram dominates the cross section close to the threshold. The W-pair production process and the CC03 diagrams actually belong to the larger set of four-fermion processes which are discussed in more detail in section 4.3.

The total cross section of the W-pair production can be calculated approximately by taking the finite width  $\Gamma_W$  of the W boson into account. In this so called *off-shell Born-level* calculation, the total cross section  $\sigma^{\text{off-shell}}$  is given by the convolution of distributions representing the W bosons with the *on-shell Born-level* cross section  $\sigma_0$  which assumes stable W bosons. The *on-shell Born-level* cross section can be written as the quadratic sum of the individual amplitudes associated with the CC03 diagrams. The total cross section is then given by

$$\sigma^{\text{off-shell}}(s) = \int_0^s dx \int_0^{(\sqrt{s}-\sqrt{x})^2} dy \rho(x) \rho(y) \sigma_0(s, x, y), \quad (4.9)$$

where  $\sqrt{s}$  denotes the center-of-mass energy and  $x$  ( $y$ ) the squared mass of the first (second) W boson. The W bosons are described by relativistic Breit-Wigner functions

$$\rho(x) = \frac{1}{\pi} \frac{\Gamma_W}{M_W} \frac{x}{(x - M_W^2)^2 + x^2 (\Gamma_W/M_W)^2} \quad (4.10)$$

<sup>2</sup>The nomenclatur states that this subset of the four-fermion processes is mediated by a charged-current and consists of 3 diagrams.



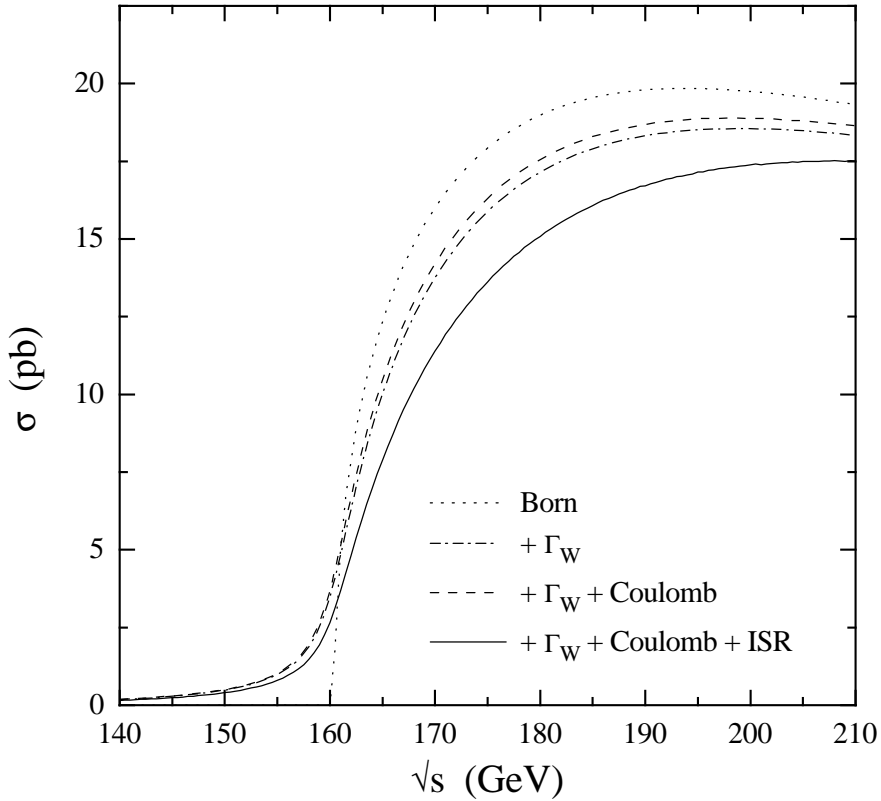


**Figure 4.4:** The total cross section of the W-pair production as calculated from the CC03 diagrams as a function of the center-of-mass energy [11]. The Born cross section and successive improvements are shown, see the text for further explanations.

which are the only terms in equation (4.10) which depend on the W boson mass  $M_W$  and width  $\Gamma_W$ .

The cross section is further modified by radiative corrections, which are discussed in detail in [11]. An important role is played by *Initial State Radiation* (ISR), the emission of a photon from the incoming electron or positron, which leads to a lower effective center-of-mass energy and results in final states of four fermions and one or more photons. A second radiative correction, the *Coulomb singularity* is important near the threshold and describes the exchange of low energy photons between the two W bosons. This correction modifies the cross section at the threshold by about 6%.

Figure 4.4 shows the total W-pair production cross section as calculated from the doubly resonant CC03 diagrams in the Born approximation as a function of the available center-of-mass energy as well as the influence of the width of the W boson and the radiative corrections on the cross section. The total cross section for the W-pair production as measured with the OPAL detector up to a center-of-

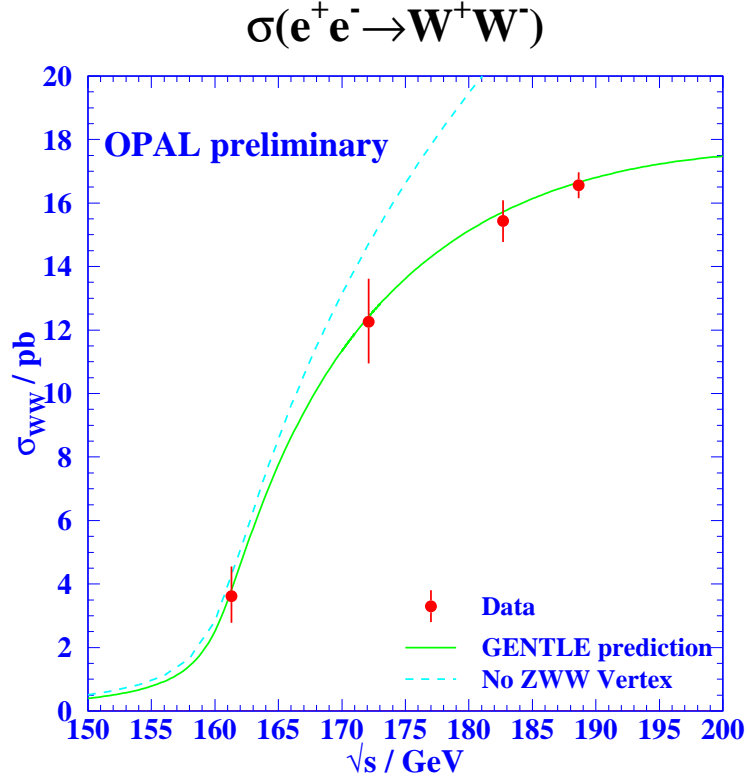


**Figure 4.5:** OPAL measurements [18] of the total cross section of the W-pair production as a function of the center-of-mass energy compared to predictions of the GENTLE program.

mass energy of  $\sqrt{s} = 189$  GeV [18] is depicted in figure 4.5. The measurements agree well with the Standard Model prediction calculated by the semi-analytical GENTLE program [19] (solid line). The dashed line shows the total cross section in the absence of the  $WWZ^0$  vertex.

### 4.3 Four-Fermion Processes

The W-pair production and their decay,  $e^+e^- \rightarrow W^+W^- \rightarrow 4f$ , belong to the class of 4-fermion processes, i.e. reactions with an  $e^+e^-$  initial state and four fermions in the final state. Such processes do not only proceed through the three doubly resonant CC03 diagrams of the W-pair production, but also through diagrams with the same initial and final state, but different intermediate states. Interference effects between the W-pair production diagrams and other diagrams with final states which can occur in the decay of two W bosons have to be taken into account in the analysis of W-pair events and the measurement of the W mass.

The 4-fermion processes can be classified in abelian and non-abelian diagrams,

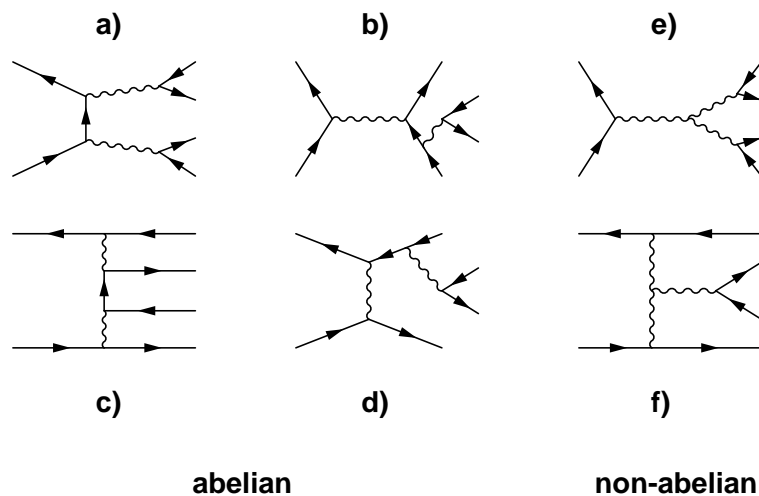


**Figure 4.6:** The six fundamental classes of 4-fermion diagrams. Straight lines denote fermions, wavy lines gauge bosons. In the abelian diagrams (a-d) each gauge boson line can be either a  $\gamma$ , a  $Z^0$ , or a  $W^\pm$  boson, depending on the fermions. In the non-abelian diagrams (e and f) two of the three boson lines are  $W^\pm$  bosons. For diagrams b) and d) the boson emitted by an outgoing fermion can also originate from an incoming fermion.

the non-abelian diagram contain a triple gauge boson vertex (that is, either  $WW\gamma$  or  $WWZ^0$ ). Figure 4.6 shows the six fundamental types of 4-fermion diagrams, including the diagrams a) and e) which contribute to the  $W$ -pair production.

Diagrams with final states which can originate from the decay of a pair of  $W^+W^-$  bosons can interfere with the CC03 diagrams. As an example, consider the process

$$e^+e^- \rightarrow u\bar{d}\mu\bar{\nu}_\mu,$$

which is a possible final state of a  $W$ -pair decay ( $W^+ \rightarrow u\bar{d}$  and  $W^- \rightarrow \mu\bar{\nu}_\mu$ ). For this process not only the diagrams a) and e) contribute to the cross section, but diagram b) contributes four times (a  $\gamma$  or  $Z^0$  in the  $s$ -channel and a  $W^+$  or  $W^-$  emitted from the outgoing fermion line) as well. The number of interfering diagrams increases with the number of electrons or electron-neutrinos in the final state, because this is the only case in which the diagrams c), d) and f) can contribute.

The usage of only the CC03 diagrams in  $W$ -pair physics, instead of the full set of 4-fermion diagrams, nevertheless proves to be a good approximation as the contributions of the other diagrams are small. This is due to the fact that most of the 4-fermion contributions are situated in different phase space regions than the  $W$ -pair events. As an example, consider again the above mentioned process,  $e^+e^- \rightarrow u\bar{d}\mu\bar{\nu}_\mu$ . For the CC03 diagrams the invariant masses of the fermion

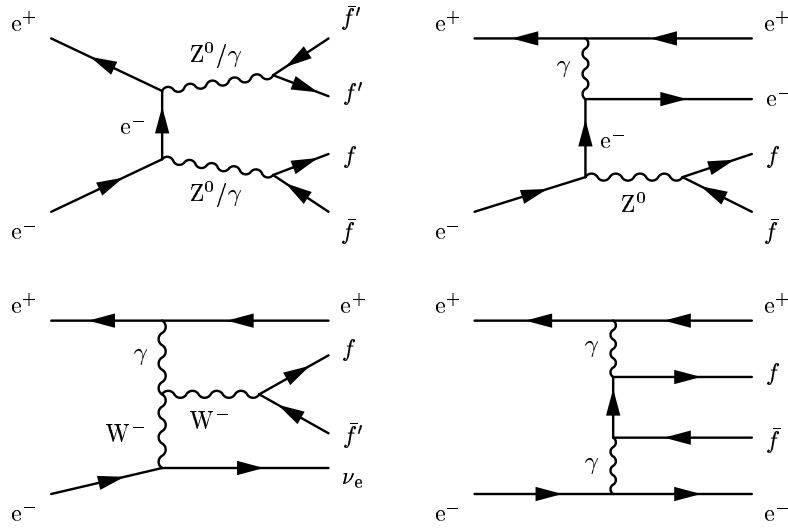


**Figure 4.7:** The four most important 4-fermion background processes in W-pair physics.

pairs ( $u\bar{d}$  and  $\mu\bar{\nu}_\mu$ ) has to be close to the W mass  $M_W$ , since they are produced by real W bosons. For the interfering diagram b) only one W boson is produced and therefore only one fermion pair will have an invariant mass close to the W mass. In addition, the individual amplitudes of other 4-fermion diagrams are often very small compared to the CC03 diagrams. The most important contributions to W-pair physics arise from the following four types of 4-fermion diagrams, depicted in figure 4.7:

- $Z^0(\gamma)$  pair production ( $Z\gamma, ZZ, \gamma\gamma$ )  
Due to phase space arguments only the  $Z^0 Z^0$  case is relevant in W-pair physics. The  $Z^0 Z^0$  production is a potential background source in the fully hadronic decay channel  $W^+W^- \rightarrow q\bar{q}q\bar{q}$ .
- Single  $Z^0$  production ( $eeZ$ )  
This process has a high cross section and is an important background in the  $W^+W^- \rightarrow q\bar{q}e\nu$  channel, although the diagram does not interfere with the CC03 diagrams (an exception is the  $e^+\nu_e e^-\bar{\nu}_e$  final state). However, in most cases only one electron can be detected since the intermediate photon is quasi-real, which leads to small angle scattering.
- Single W production ( $evW$ )  
This process leads to an indistinguishable background for final states with an electron-neutrino pair and the diagram can interfere with the CC03 class of diagrams. The— in most cases—quasi-real photon leads only to small angle scattering and the electron usually remains undetected in the beam pipe, which simplifies the suppression of this background.

- 2-photon production

This process has a very high cross section, but is suppressed as a background source in  $W$ -pair physics due to the fact that the invariant mass of the fermion pairs is very low. In most cases only small angle scattering of the electron and positron occurs and they escape undetected in the beam pipe. The remaining fermion pair is boosted along the  $z$  direction and these events can be easily rejected in the  $W^+W^- \rightarrow q\bar{q}q\bar{q}$  and  $W^+W^- \rightarrow q\bar{q}\ell\bar{\nu}$  cases. However, they pose a source of indistinguishable background in the  $W^+W^- \rightarrow \bar{\ell}\nu\ell\bar{\nu}$  case.

The cross sections of the most important processes in the center-of-mass energy range of LEP2 are summarized in figure 4.8, including the  $W$ -pair production, the above mentioned four-fermion background processes and the two-fermion processes described in the next section.

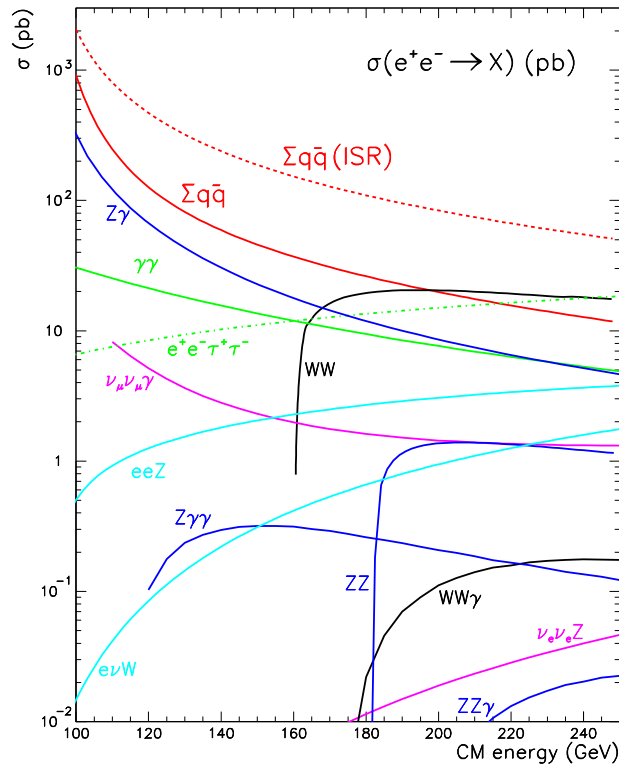


**Figure 4.8:** The cross sections of the most important processes in the center-of-mass energy range of LEP2.  $WW$  denotes the  $W$ -pair production cross section. Important background processes for the measurement of the  $W$  mass are  $e\nu W$ ,  $eeZ$ , and  $ZZ$ . The important two-fermion processes, whose cross sections are denoted by  $\Sigma q\bar{q}$  and  $\Sigma q\bar{q}(\text{ISR})$ , are discussed in section 4.4.

#### 4.4 Two-Fermion Processes

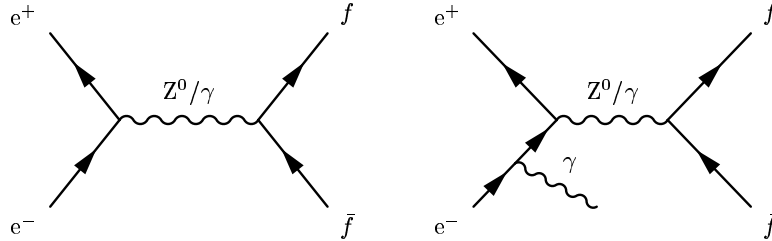


**Figure 4.9:** Lowest order Feynman diagrams for  $e^+e^- \rightarrow Z^0/\gamma \rightarrow f\bar{f}$  (left) and  $e^+e^- \rightarrow Z^0/\gamma \rightarrow f\bar{f}\gamma$  (right).

All W-pair decay channels in which one of the W bosons decays hadronically into a quark-antiquark pair suffer from the background of  $e^+e^- \rightarrow Z^0/\gamma \rightarrow q\bar{q}$ , which belongs to the class of 2-fermion processes  $e^+e^- \rightarrow Z^0/\gamma \rightarrow f\bar{f}$ , see figure 4.9. The inclusion of radiative corrections in the calculation of the cross section is especially important in this class of events, as most of the  $Z^0$  bosons at LEP2 center-of-mass energies are created in association with one or more photons emitted by the incoming electron or positron (*Initial State Radiation, ISR*), see figure 4.9 right. The convolution of the ISR photon spectrum with the Born cross section leads to a significant enhancement of the cross section even at high energies, as can be seen in figure 4.8; here  $\Sigma q\bar{q}(\text{ISR})$  denotes the cross section of the process  $e^+e^- \rightarrow q\bar{q}$ , taking ISR into account, while  $\Sigma q\bar{q}$  denotes the uncorrected cross section.

The cross section for 2-fermion processes increases enormously if the energy of the ISR photon is

$$E_\gamma = \frac{s - M_Z^2}{2\sqrt{s}}.$$

Events of this type are called *radiative returns*, since the effective center-of-mass energy is equal to the  $Z^0$  mass,  $\sqrt{s'} = M_Z$ , and the bosons are created at the  $Z^0$  resonance peak. Fortunately, these events are easy to reject by calculating the invariant mass of the fermion pair.

Of more interest are the non-radiative events, since in these cases the complete center-of-mass energy is converted to hadrons. If the primary quarks emit hard gluon radiation, three or four jet topologies can be created which can appear as events from the processes  $W^+W^- \rightarrow q\bar{q}\tau\bar{\nu}$ —in which the tau lepton decays hadronically—and  $W^+W^- \rightarrow q\bar{q}q\bar{q}$ .

## 4.5 Final State Interactions

In this section we review briefly the influence of final state interactions (FSI) on the reconstruction of the W mass. While final state interactions do not actually modify the properties of the W boson as a particle, they provoke a mismatch of decay products to the correct parent W boson, or even make the concept of a single parent invalid, which can result in systematic shifts of the reconstructed mass of the W boson compared to its true mass.

The two final state interactions discussed here, *Bose-Einstein Correlations*—a purely quantum mechanical phenomenon—and *Color Reconnection*—a QCD interference effect—only affect the reconstruction of the W mass in the hadronic decay channel,  $W^+W^- \rightarrow q\bar{q}q\bar{q}$ . While present in any hadronic decay, they cannot change the reconstructed mass of the W boson in the semileptonic channel,  $W^+W^- \rightarrow q\bar{q}\ell\bar{\nu}$ .

Monte Carlo studies of FSI show a model-dependent mass bias, the difference of the reconstructed mass to the true mass, in the range of 100 MeV for the W boson mass. With the expected statistical error of 30–40 MeV on the W mass measurement at the end of LEP2, one ends up in the undesirable situation that a systematic error dominates the precision of the final result. The discovery of sensitive variables on the effects of FSI and their measurement in an attempt to narrow down the range of acceptable models therefore becomes a matter of utmost importance [20, 21].

### 4.5.1 Bose-Einstein Correlation

The term *Bose-Einstein Correlations* (BEC) describes the quantum mechanical phenomenon that there is a difference between the correlation of identical and non-identical bosons, an effect already observed in pp-collisions in same-sign pions more than 40 years ago.

In W boson pair production the *Bose-Einstein Correlations* can produce, in the hadronization stage, a coherence between identical bosons originating from the  $W^+$  and  $W^-$ . Thus it is no longer possible to assign the produced particles to one or the other W boson. In the usual mass reconstruction scheme for W-pair events in the  $W^+W^- \rightarrow q\bar{q}q\bar{q}$  decay channel, two jets are associated with each W boson and the invariant mass of this system is calculated; the W bosons are treated as completely separate particles. The BEC lead to an energy flow between the two jet systems which is not taken into account in the calculation of the reconstructed W boson mass. Monte Carlo studies of this effect with different models show a mass bias on the W mass in the range of 20–100 MeV.

At OPAL the approach to measure the *Bose-Einstein Correlations* at LEP2 energies is to compare the number of like-sign and unlike-sign pions produced in  $e^+e^- \rightarrow W^+W^- \rightarrow q\bar{q}q\bar{q}$ ,  $e^+e^- \rightarrow W^+W^- \rightarrow q\bar{q}\ell\bar{\nu}$  and  $e^+e^- \rightarrow Z^0/\gamma \rightarrow q\bar{q}$  events. At present, the statistical precision is insufficient to determine whether *Bose-Einstein Correlations* exist between different W bosons [22].

### 4.5.2 Color Reconnection

The *Color Reconnection* effect refers to the interference between color singlets in the non-perturbative phase of the hadronization<sup>3</sup>. As the space-time separation between the two decaying W bosons at LEP2 center-of-mass energies is smaller than the typical hadronization scale, a color flow between the members of the original color singlets resulting from a fully hadronic decay of a W pair,  $W^+W^- \rightarrow q\bar{q}q\bar{q}$ , can occur. This can lead to the production of particles which cannot be associated with either of the W bosons alone.

The *Color Reconnection* effect is supposed to alter event shape variables, charged particle multiplicities, and momentum spectra.

In the measurement of the mass of the W boson, the *Color Reconnection* effect can introduce significant shifts of the reconstructed mass in the  $W^+W^- \rightarrow q\bar{q}q\bar{q}$  channel, since the color flow between the decay products of the two W bosons can lead to an incorrect association of color objects and their energy to the W bosons.

With the current knowledge of non-perturbative QCD, *Color Reconnection* interference effects can be estimated only in the context of specific models implemented in the Monte Carlo generators, see chapter 5.4.

So far the statistical precision of the data collected in W boson pair decays at LEP2 is insufficient to discriminate between the different models. However, experimental studies of sensitive variables on *Color reconnection* in an attempt to estimate its effect on the W mass measurement in the  $W^+W^- \rightarrow q\bar{q}q\bar{q}$  channel are ongoing [21, 24].

## 4.6 WW Event Classes

The W-pair events can be classified according to their decay mode into three classes. In the leptonic class both W bosons decay to a lepton-neutrino pair. In the semileptonic class, one W boson decays hadronically to a quark-antiquark pair, the other to a lepton-neutrino pair. In the hadronic class both W bosons decay hadronically to quark-antiquark pairs.

Each of the channels has advantages and disadvantages concerning the event selection, background contributions and the method used to extract the mass of the W boson from the data.

In the detector, the decay of a W boson into an lepton-neutrino pair results in a single track in tracking system from the charged lepton, or in the case of a primary tau lepton decaying into hadrons in a low multiplicity jet (1 or 3 charged tracks). Associated with the track is a cluster in the calorimeters. If the lepton is an electron, it is stopped in the ECAL and deposits its total energy there; in the case of a muon only a small amount of energy is lost in the two calorimeters (due to its higher mass, the muon hardly emits bremsstrahlung and thus cannot initiate an electromagnetic

---

<sup>3</sup>At present there is general consensus that observable effects of such interactions during the perturbative phase are expected to be small [23].



shower in the ECAL; the energy loss occurs only through ionization), but additional information is provided by the muon chambers. Primary and secondary neutrinos escape unobserved, but lead to a lack of observed energy and momentum.

The decay of a W boson to a quark-antiquark pair leads to high multiplicity particle jets due to the hadronization of the primary partons. Usually, two jets are observed, but if a hard gluon is emitted by one of the quarks under a great angle a third separate jet can be created. The jet energy can be reconstructed by combining momentum information from the tracking system with the information from the calorimeters.

#### 4.6.1 The Leptonic Decay Channel, $W^+W^- \rightarrow \bar{\ell}\nu\ell\bar{\nu}$

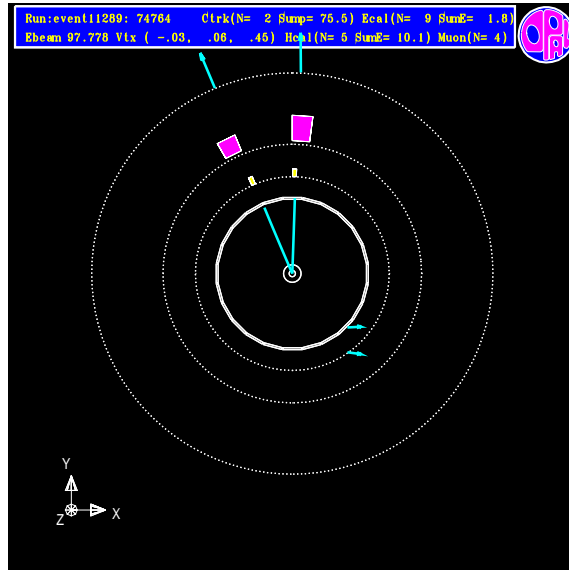


**Figure 4.10:** An event selected as  $W^+W^- \rightarrow \bar{\ell}\nu\ell\bar{\nu}$  as seen in the OPAL event display, a schematic view of the detector and its response. The cyan (light grey) lines originating at the vertex are the tracks of the two muons in the central tracking chambers, the yellow (light grey) and magenta (grey) blocks are entries in the electromagnetic and hadronic calorimeters and the cyan (light grey) arrows denote hits in the muon chambers.

The events in the leptonic class,  $W^+W^- \rightarrow \bar{\ell}\nu\ell\bar{\nu}$ , are characterized by two acoplanar, energetic leptons and large missing energy and momentum, which is carried away by the undetected neutrinos. In 4/9 of the cases, one of the leptons is a tau lepton, which can decay to a narrow hadronic jet; in 1/9 of the cases both leptons are taus. The main background contributions arise from the processes  $e^+e^- \rightarrow Z^0/\gamma \rightarrow f\bar{f}$ ,  $e^+e^- \rightarrow Z^0Z^0$ ,  $e^+e^- \rightarrow Z^0e^+e^-$ , and  $e^+e^- \rightarrow W\ell\nu_e$ .

Figure 4.10 shows a typical candidate for a leptonic WW decay in the OPAL event display, a schematic view of the detector and its response.

**Advantages:**

- Clean event signature (2 high energetic leptons or low multiplicity jets)
- No high multiplicity jets
- Low background from other processes
- No combinatorial background (no wrong jet-W association possible)
- No influence of *Color Reconnection* and *Bose-Einstein Correlations* on the reconstructed mass  $M_W$
- No systematic uncertainties associated with the hadronization model

**Disadvantages:**

- Low statistics (11% of all decays, 5% if final states with tau leptons are excluded)
- Missing information due to undetected neutrinos
- No energy information for primary tau leptons (due to the additional neutrino emitted in the tau decay)
- No complete kinematic reconstruction possible due to the lack of a sufficient number of constraints

### 4.6.2 The Semileptonic Decay Channel, $W^+W^- \rightarrow q\bar{q}\ell\bar{\nu}$

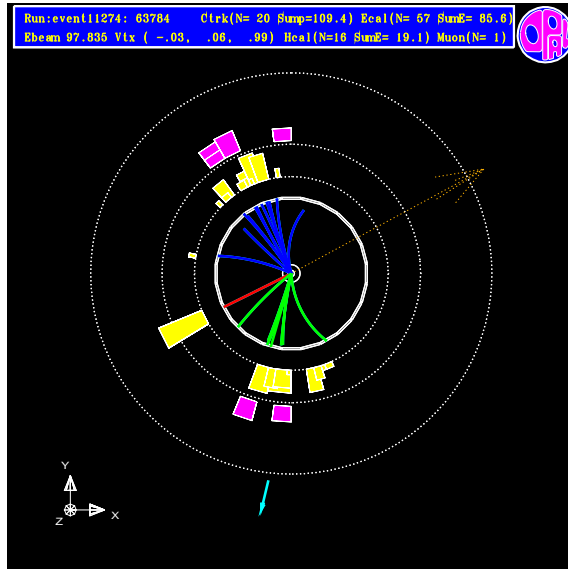


**Figure 4.11:** An event selected as  $W^+W^- \rightarrow q\bar{q}\ell\bar{\nu}$  as seen in the OPAL event display, a schematic view of the detector and its response. The blue (dark grey) and green (light grey) lines originating from the vertex are the tracks of the two reconstructed jets in the central tracking chambers, the red (grey) line the track of the electron, the yellow (light grey) and magenta (grey) blocks are entries in the electromagnetic and hadronic calorimeters, the cyan (light grey) arrow denotes a hit in the muon chambers, the dashed arrow the missing momentum of the unobserved neutrino.

The events in the semileptonic class,  $W^+W^- \rightarrow q\bar{q}\ell\bar{\nu}$ , are characterized by two hadronic jets and an isolated track with possibly an associated calorimeter clusters (in the case of an electron) for the lepton, or a low multiplicity (1 or 3 charged tracks) jet in the case of a primary tau lepton decaying into hadrons. In all events missing energy and a momentum imbalance are expected due to the undetected neutrino. The overall background is very low (at the percent level), only in the  $W^+W^- \rightarrow q\bar{q}\tau\bar{\nu}$  channel the  $e^+e^- \rightarrow Z^0/\gamma \rightarrow q\bar{q}$  process leads to a sizeable background contribution of approximately 10%.

Figure 4.11 shows a typical candidate for a semileptonic WW decay in the OPAL event display.

#### Advantages:

- High statistics (44% of all decays)
- Complete kinematic reconstruction possible
- Low background from other processes

- No combinatorial background (no wrong jet-W association possible)
- No influence of *Color Reconnection* and *Bose-Einstein Correlations* on the reconstructed mass  $M_W$

**Disadvantages:**

- No energy information for primary tau leptons (due to the additional neutrino emitted in the tau decay)
- Kinematic reconstruction less constrained than in the  $W^+W^- \rightarrow q\bar{q}q\bar{q}$  channel due to the undetected primary neutrino

### 4.6.3 The Hadronic Decay Channel, $W^+W^- \rightarrow q\bar{q}q\bar{q}$

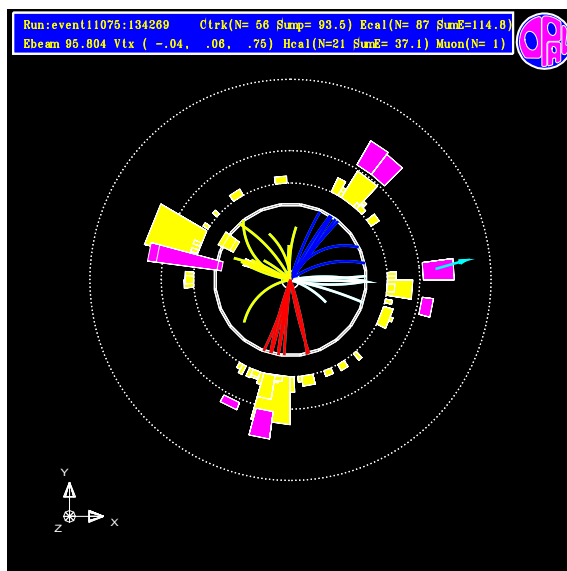


**Figure 4.12:** An event selected as  $W^+W^- \rightarrow q\bar{q}q\bar{q}$  with a 4-jet topology as seen in the OPAL event display, a schematic view of the detector and its response. The white, yellow (light grey), red (grey), and blue (dark grey) lines originating from the vertex are the tracks of the four reconstructed jets in the central tracking chambers, the yellow (light grey) and magenta (grey) blocks are entries in the electromagnetic and hadronic calorimeters, the cyan (light grey) arrow denotes a hit in the muon chambers.

The events in the hadronic decay channel,  $W^+W^- \rightarrow q\bar{q}q\bar{q}$ , are characterized by the complete conversion of the available center-of-mass energy into hadrons. The topology should be at least consistent with four jets, but can include five or more jets if hard gluon radiation is emitted by the primary quarks. Except for possible

losses in the beam pipe<sup>4</sup>, the events should satisfy energy and momentum conservation. One disadvantage of the  $W^+W^- \rightarrow q\bar{q}q\bar{q}$  channel with regard to the measurement of the mass of the W boson is the combinatorial background, since the four jets can be combined in three ways to form the two W bosons, with only one correct combination. In the case that a hard gluon is emitted by a primary parton and five jets are reconstructed, the jet association becomes even more complicated since there are now ten different combinations to form two W bosons [25]. The main background contribution in this decay channel are  $e^+e^- \rightarrow q\bar{q}$  events with a 4-jet like signature.

Figure 4.12 shows a typical candidates for a hadronic WW decays in the OPAL event display.

**Advantages:**

- High statistics (45% of all decays)
- Complete kinematic reconstruction possible (no missing information)

**Disadvantages:**

- Larger background contributions from other processes
- Combinatorial Background (wrong jet-W association)
- *Color Reconnection* and *Bose-Einstein Correlations* FSI can influence the reconstructed mass  $M_W$

---

<sup>4</sup>Small losses in the visible energy can also occur through long-lived neutral hadrons, e.g.  $K_L^0$  mesons, which have a lifetime long enough to leave the detector and escape unobserved.



## Chapter 5

# Simulation of Physics Events

This chapter briefly describes the programs used to simulate physics events. The different Monte Carlo (MC) generators that were used in the simulation of physics events for the  $W$ -pair production and background processes and the treatment of special fields, like the hadronization model and FSI models, are touched. A more complete discussion of the MC generators and a comparison of their performance can be found in [26].

The production of Monte Carlo events is carried out along the following scheme: The primary particles are generated according to the calculated matrix elements and the MC input parameters, as e.g. the  $W$  mass. After the primary particles have been generated, first a perturbative QCD phase takes place which can lead to the emission of gluons from the primary quarks. The resulting set of particles is called the parton level of the event. Next the fragmentation and hadronization of the partons in the non-perturbative QCD phase is performed according to a phenomenological model. The resulting particles are passed on to the GOPAL program [27], a GEANT [28] based simulation of the OPAL detector. Particles are traced through the detector with all their interactions, new particles are created, e.g. in pair production from photons, and unstable particles decay. The detector response to the passing particles is simulated and stored in the same format as for real physics events.

### 5.1 Monte Carlo Generators

- **KORALW** [29]  
is the standard Monte Carlo generator used for  $W$  studies at OPAL. It has an excellent implementation of QED effects like *Initial* and *Final State Radiation*. An interface to the GRACE library [30] to calculate multi-diagram matrix elements is also present. KORALW uses the program JETSET to perform the hadronization.
- **GRC4F** [30]  
allows the full set of 4f-diagrams, including interference effects, to be used.

Several options for the inclusion of *Initial State Radiation* exist. `grc4f` presently has the limitation that CKM matrix mixing (compare chapter 3.1) is not implemented (no W decays in `cd` or `us`)

- **EXCALIBUR** [31]  
allows the full set of 4f-diagrams, including interference effects, to be used or to use only selected diagrams. EXCALIBUR has presently the limitation that the fermions are considered massless. The version used by OPAL has an interface to JETSET with an *ad hoc* inclusion of fermion masses (which are needed for the simulation of the initial parton shower) to perform the hadronization of the events. The EXCALIBUR program allows the generation of events with anomalous triple gauge couplings.
- **PYTHIA** [32]  
does not include interference effects between different diagrams and is therefore no real 4-fermion generator. It is used to simulate  $W\nu\nu$ ,  $Z^0Z^0$ , and  $Z^0e\bar{e}$  backgrounds. PYTHIA is the standard Monte Carlo generator for the 2-fermion background simulation.

## 5.2 The Hadronization Model

For the fragmentation and hadronization of strongly interacting primary particles different models can be interfaced to the above mentioned generators.

- **JETSET** [32]  
describes the fragmentation/hadronization by the Lund String Model. The JETSET program has been extensively tuned to LEP1 data and provides a very good description of hadronic final states. For this reason the JETSET program has been chosen within the OPAL collaboration to perform the hadronization for the standard Monte Carlo data.
- **HERWIG** [33]  
uses an alternative approach to the string model, the cluster model. The HERWIG program is a full featured Monte Carlo generator, but is used in the most cases only as a *postgenerator*; it takes over from other Monte Carlo generators after the 4-vectors of the primary leptons and quarks have been produced.  
  
The HERWIG model is used in systematic studies of the fragmentation and hadronization.
- **ARIADNE** [34]  
is similar to the JETSET model, but uses a different parameter to describe the development of the parton shower.



## 5.3 Tau Decays

The decays of tau leptons were simulated with the TAUOLA [35] program, which implements hadronic decays including resonances.

## 5.4 Final State Interaction Models

Final state interactions are implemented in several Monte Carlo generators. As *Color Reconnection* and *Bose-Einstein Correlations* are currently not accessible in precise calculations, their description is based on phenomenological models.

### 5.4.1 Bose-Einstein Correlations

The *Bose-Einstein* effect can be implemented as a supplementary routine which uses the LUBOEI model [32] in the JETSET program. In this model, particles are shuffled after the hadronization between the two W bosons according to a simple phenomenological parameterization of the *Bose-Einstein Correlations*. Unfortunately, at present, this model has the shortcoming that the momentum conservation is violated locally and only the global momentum is conserved.

### 5.4.2 Color Reconnection

The *Color Reconnection* effect is implemented in a variety of models. Usually the Sjöstrand-Khoze [23] and the Ariadne [34] models are used to evaluate the systematic uncertainties on the measurement of the mass of the W boson.

The Sjöstrand-Khoze model offers two approaches both based on the JETSET string hadronization: In the SK1 model a reconnection takes place if the overlap of two color strings exceeds a certain (user defined) value, in the SK2 model a reconnection takes place if the color strings cross each other. The Sjöstrand-Khoze model exists as supplementary routine for the JETSET program.

The ARIADNE Monte Carlo generator has built-in *Color Reconnection* models based on the Gustaffson-Häkkinen model, in which all string combination between quarks and gluons are permitted; from these combinations the *shortest* string in momentum-space is chosen.

The HERWIG generator implements a *Color Reconnection* model as well; reconnections occur between quarks if they are close in coordinate space.



## Chapter 6

# From $W^+W^- \rightarrow q\bar{q}\ell\bar{\nu}$ Events to the $W$ Boson Mass $M_W$

Before we start with the description of the measurement of the mass of the  $W$  boson, this chapter briefly outlines the approach of the data recording in the OPAL experiment and gives an overview over the data analysis of this thesis. Figure 6.1 provides a diagram of the data flow from the physics events to the physics results.

### 6.1 On-Line Data Flow

The purpose of the OPAL detector is to record the maximum achievable amount of *interesting* events, to provide the data for physics analysis.

Unfortunately, the OPAL data acquisition system (DAQ) cannot handle the amount of data generated by the detector if all components are constantly read out with the bunch crossing frequency of 45 kHz of the electron-positron beams in the LEP accelerator.

To reduce the amount of data, a trigger logic analyses the *fast* signals provided by the subdetectors and a bunch-crossing signal to discriminate between physics events which originated from an  $e^+e^-$  collision and background events like beam-gas interactions and cosmic rays which randomly cross the detector. The decision of the trigger logic is based on *stand-alone* signals like track and cluster multiplicities and *correlated* signals of a rough segmentation of the OPAL detector in the  $\theta$  and  $\phi$  directions. The purpose of the trigger logic is to reduce the event rate to about 3–10 Hz, to minimize DAQ inefficiencies due to readout deadline.

In the case of a negative trigger decision the subdetectors are instructed to *forget* the currently collected information and to get ready for a new event in the next bunch crossing.

On the other hand, if an event is flagged as a physics event by the trigger logic, all further triggers are inhibited until the information of each subdetector is read out by the front-end electronics and processed by the DAQ system. The data col-

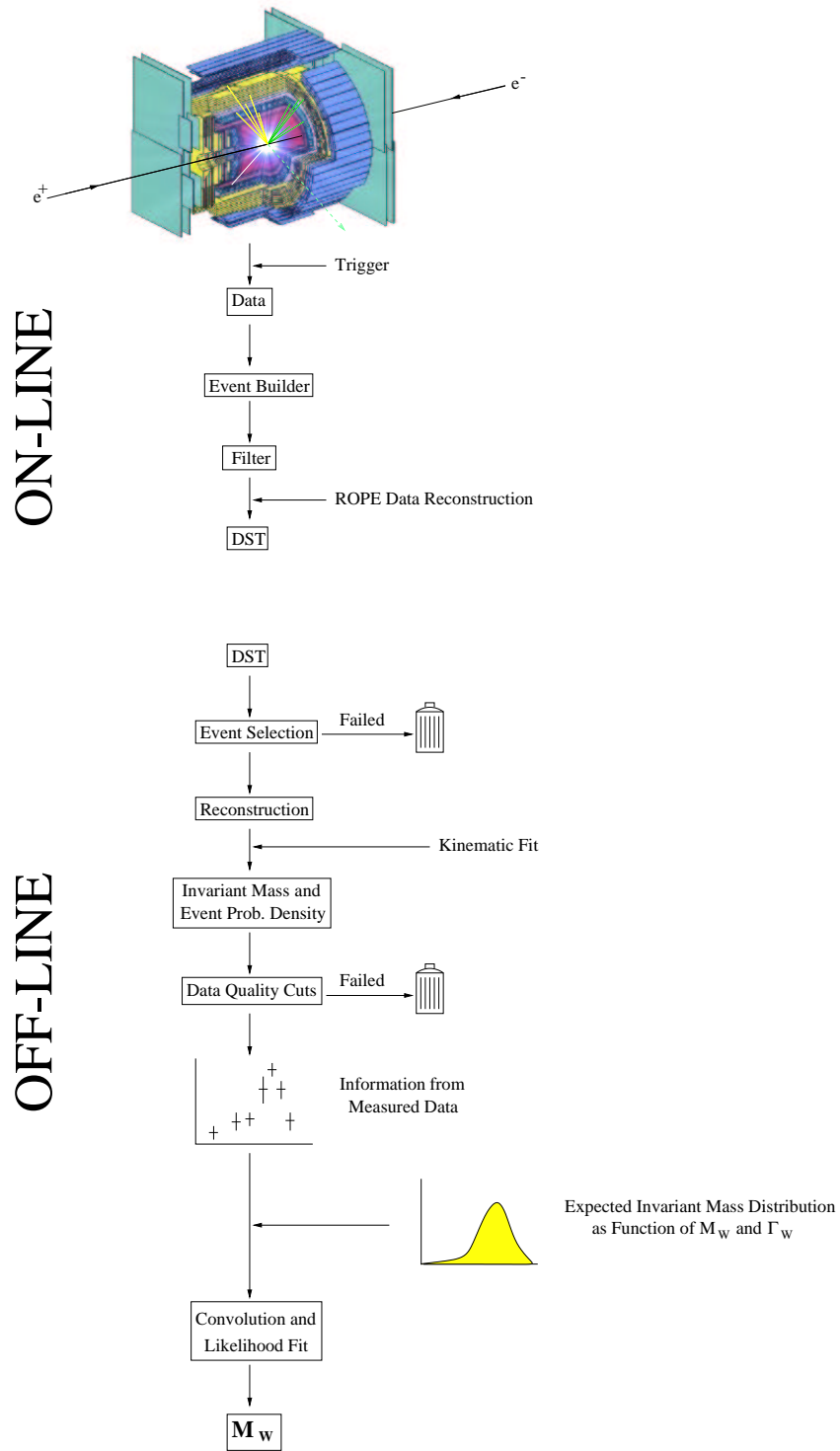


Figure 6.1: Data flow from the event recording to the physics result.

lected by the subdetectors is merged by the *Event-Builder* and passed to the *Filter*. An average  $W^+W^- \rightarrow q\bar{q}\ell\bar{\nu}$  event is composed of about 250 kBytes of data. The *Filter* monitors the data quality, classifies the events based on their topology and disposes obvious *junk events*. The data, event headers containing additional information, e.g. the beam energy, and calibration files are further passed to the ROPE computing farm which reconstructs the events. The ROPE [36] program analyzes the raw data from the subdetectors and e.g. calculates hit coordinates, reconstructs vertices, performs track fitting and merges calorimeter clusters.

The reconstructed event information is sent to the `shift` farm, located at the central computing facility at CERN, and is written to magnetic tapes. These tapes, called DSTs (Data Summary Tapes), can be used in the off-line analysis by the individual physicist.

## 6.2 Off-line Analysis

The off-line analysis in the OPAL experiment is based on the use of the information available on the DSTs (Data Summary Tapes).

In a first step of each analysis, candidate events are determined by applying an event selection (see chapter 7.1). The event selection tries to find events which match the expected signature of the requested types of events, in this analysis semileptonic W-pair decays. Only events which passed these selection are further considered.

After the events have been selected, they are further reconstructed (see chapter 7.2). Tracks and clusters are combined to jets, and lepton candidates are determined.

The reconstructed jet and lepton 4-momenta, together with their errors, are used as input values of a kinematic fit which calculates improved estimates for these quantities and allows the application of physical constraints like energy and momentum conservation. After the kinematic fit, the event is fully reconstructed and the best possible estimates for the momenta of the primary decay products of the original pair of W bosons are known. This information can be used to calculate the invariant masses of the W bosons in each individual event (see chapter 7.3).

The events used in the mass analysis then have to pass some additional data quality cuts.

The measurement of the mass of the W boson is based on a unbinned likelihood fit with a semi-analytical parent distribution as the expected invariant event W mass distribution; the parent distribution depends on the unknown parameters of the W boson, its mass  $M_W$  and its width  $\Gamma_W$ . The precision of the individual event W masses in the data is taken into account by a convolution of an event probability density, derived from the measurements, with the likelihood parent distribution (see chapter 8.2). By maximizing the total likelihood of the data sample, the best estimate for the W mass  $M_W$  can be determined, assuming the Standard Model relation between  $M_W$  and  $\Gamma_W$ .



## Chapter 7

# Selection and Reconstruction of $W^+W^- \rightarrow q\bar{q}\ell\bar{\nu}$ Events

This chapter describes the selection and reconstruction of  $W^+W^- \rightarrow q\bar{q}\ell\bar{\nu}$  events from the data recorded with the OPAL detector. The same procedure can, of course, be applied to simulated data from Monte Carlo samples.

For most tasks concerning the event reconstruction presented in this thesis, the WW analysis framework [37] was used. This analysis framework is a set of FORTRAN routines created by members of the OPAL collaboration. Its aim is to provide the tools to select W-pair candidate events and to reconstruct the jets and lepton information, thus putting different analysis approaches on a common ground.

The chapter starts with a description of the event selection, where we will concentrate on the  $W^+W^- \rightarrow q\bar{q}\ell\bar{\nu}$  selection and only briefly review the  $W^+W^- \rightarrow \bar{\ell}\nu\ell\bar{\nu}$  and  $W^+W^- \rightarrow q\bar{q}q\bar{q}$  selections. After an event is selected as a candidate for a  $W^+W^- \rightarrow q\bar{q}\ell\bar{\nu}$  decay, the measurements of the detector components have to be analyzed and the particle tracks and calorimeter clusters have to be combined to match this hypothesis. To this end, the track most likely originating from the lepton is identified and the non-leptonic part of the event is forced into two jets. Special care must be taken in the reconstruction of  $W^+W^- \rightarrow q\bar{q}\tau\bar{\nu}$  events, as the tau lepton cannot be measured directly, but only through its decay products. The reconstructed lepton and jet momenta are then improved by the application of a kinematic fit which incorporates a set of constraints motivated by physical considerations.

In the scope of this thesis, a version of the WW analysis framework [37] which is optimized for a center-of-mass energy of  $\sqrt{s} = 189$  GeV was used. It contains routines applicable to lower center-of-mass energies as well and was also used to analyze the data at  $\sqrt{s} = 183$  GeV.

## 7.1 The Event Selection

The selection of W-pair events follows the categorization of these events in the  $W^+W^- \rightarrow \bar{\ell}\nu\ell\bar{\nu}$ ,  $W^+W^- \rightarrow q\bar{q}\ell\bar{\nu}$ , and  $W^+W^- \rightarrow q\bar{q}q\bar{q}$  classes as described in chapter 4.6. The primary physics results extracted from the selections are the measurement of the W-pair production cross section and the relative W boson branching fractions [18].

The same event selections are also used in the analysis of the W mass measurement and in a wide variety of other analyses, either as a selection or a rejection tool of W-pair events.

The order in which the selections were applied to an event in the context of this thesis moves from the most clear signature to the most general case: First the events are matched against the hypothesis of a  $W^+W^- \rightarrow \bar{\ell}\nu\ell\bar{\nu}$  event, then against the assumption of a  $W^+W^- \rightarrow q\bar{q}\ell\bar{\nu}$  event—here it is tried to match a  $W^+W^- \rightarrow q\bar{q}e\bar{\nu}$  or  $W^+W^- \rightarrow q\bar{q}\mu\bar{\nu}$  event first, before it is considered as a  $W^+W^- \rightarrow q\bar{q}\tau\bar{\nu}$  candidate—and finally the event is tested against the  $W^+W^- \rightarrow q\bar{q}q\bar{q}$  hypothesis.

The description in this chapter summarizes the event selection on a non-technical level by motivating the cuts and classes of variables used on physical grounds. A complete discussion, including e.g. the exact definition of variables used in the likelihood selections, can be found in the OPAL reference publications [18, 38–40]. The emphasis of the discussion is placed on the  $W^+W^- \rightarrow q\bar{q}\ell\bar{\nu}$  selection.

### 7.1.1 Common Track and Cluster Quality Cuts

All selections use a common set of track and cluster quality cuts to remove fake signals from electronic noise in the tracking chambers and calorimeters from the data, before the actual selection takes place.

The track quality cuts require, for each individual track, a minimal transverse momentum in the x-y plane and a maximum allowed total momentum slightly higher than the beam energy (the latter serves to remove totally wrong measurements and cosmic rays). Two geometrical constraints remove tracks which do not originate close to the interaction point and a fit of a track to the measured signals in the r- $\phi$  and z direction in the central tracking system must be successful. A minimum number of signals in the Jet chamber based on the polar track angle is required, and tracks crossing an anode plane of the chamber must be well measured.

The cluster quality cuts for the calorimeter data require a minimum energy deposited in the cluster and a minimum number of responding blocks in a cluster.

### 7.1.2 The $W^+W^- \rightarrow \bar{\ell}\nu\ell\bar{\nu}$ Event Selection

The  $W^+W^- \rightarrow \bar{\ell}\nu\ell\bar{\nu}$  event selection [38] is the first selection applied to all events in this analysis, because the leptonic W-pair events are easily identified due to their very clear signature of two isolated high-energetic lepton tracks or low multiplicity



jets. For the analysis of this thesis, which deals exclusively with the semileptonic decay channel, the  $W^+W^- \rightarrow \bar{\ell}\nu\ell\bar{\nu}$  selection serves rather as a rejection: If an event is selected as  $W^+W^- \rightarrow \bar{\ell}\nu\ell\bar{\nu}$ , it is removed from the event sample and is not further considered as a candidate for the  $W^+W^- \rightarrow q\bar{q}\ell\bar{\nu}$  hypothesis.

In contrast to the two other selections, the  $W^+W^- \rightarrow \bar{\ell}\nu\ell\bar{\nu}$  selection is entirely cut based and does not use a likelihood discriminant.

To remove obvious non  $W^+W^- \rightarrow \bar{\ell}\nu\ell\bar{\nu}$  events, a preselection is applied which constrains the number of charged tracks, the sum of the number of tracks in the central tracking system and clusters in the electromagnetic calorimeter, and the number of jets found with a *cone algorithm*<sup>1</sup>. All these cuts are based on the fact that leptonic W-pair decays lead to only a small number of observable particles (two primary charged leptons, which may decay further in the case of tau leptons).

The main selection differentiates between three cases, corresponding to the number of jets found—one, two, or three—with the cone algorithm. Only the dijet case, the most common, will be described here as an example.

Since  $W^+W^- \rightarrow \bar{\ell}\nu\ell\bar{\nu}$  events are characterized by a large amount of missing momentum, which is carried away by the at least two unobserved neutrinos, cuts are made on the acolinearity, the acoplanarity and the minimum relative transverse momentum of the dijet system.

Further cuts concern requirements imposed on the observed jets, as the number of charged tracks and the number of hits in the Microvertex and Vertex detectors. This ensures that the leptons are well reconstructed.

The next set of cuts rejects particular background event classes, with specific cuts if geometric or energetic conditions are met.

A last set of cuts concentrates on the removal of the remaining background events. The jet charges are required to be different, as is expected from the decay of a pair of  $W^+$  and  $W^-$  bosons and constraints are imposed on the measurements made in the MIP-Plug and the Gamma-catcher, subdetectors situated close to the beam pipe in the endcap regions of the OPAL detector.

The 1- and 3-jet selections work in a similar way, but these event classes are less often encountered in the  $W^+W^- \rightarrow \bar{\ell}\nu\ell\bar{\nu}$  decay channel.

The  $W^+W^- \rightarrow \bar{\ell}\nu\ell\bar{\nu}$  selection achieves an efficiency of 82.2% and a purity of 97.4%.

### 7.1.3 The $W^+W^- \rightarrow q\bar{q}\ell\bar{\nu}$ Event Selection

This section provides an overview on the  $W^+W^- \rightarrow q\bar{q}\ell\bar{\nu}$  event selection. A full, if rather lengthy, description, in *Tolstoyesque detail*<sup>2</sup>, can be found in [39].

<sup>1</sup>The cone algorithm is a jet finding algorithm that combines tracks within certain cones around the highest momentum tracks to jets. The term *jet* does not imply that more than one track is associated with it. It is just used as a convenient name to tag the separate regions with tracks found by the cone algorithm.

<sup>2</sup>M. Thomson, author of [39]

The selection of  $W^+W^- \rightarrow q\bar{q}\ell\bar{\nu}$  events consists of three parts: A likelihood selection, a rejection of 4-fermion background and a *Trackless selection* which recovers events without a measured lepton track in the central tracking system.

In addition to the standard quality cuts on tracks and clusters events have to pass a very loose pre-preselection before they are considered as  $W^+W^- \rightarrow q\bar{q}\ell\bar{\nu}$  candidates. The events are required to have a minimum visible energy and a minimum number of charged tracks and clusters in the electromagnetic calorimeter. This pre-preselection removes 2-photon events and low multiplicity events which contradict the hypothesis of two primary quarks<sup>3</sup>.

The  $W^+W^- \rightarrow q\bar{q}\ell\bar{\nu}$  likelihood selection is composed of six selections which are carried out in parallel and are optimized for the following decay chains:  $W \rightarrow e\nu_e$ ,  $W \rightarrow \mu\nu_\mu$ ,  $W \rightarrow \tau\nu_\tau \rightarrow e\nu_e\nu_\tau$ ,  $W \rightarrow \tau\nu_\tau \rightarrow \mu\nu_\mu\nu_\tau$ ,  $W \rightarrow \tau\nu_\tau \rightarrow h(n\pi^0)\nu_\tau\nu_\tau$ <sup>4</sup>, and  $W \rightarrow \tau\nu_\tau \rightarrow 3h(n\pi^0)\nu_\tau\nu_\tau$ <sup>5</sup>.

The likelihood selection consists of four parts. First the best lepton candidates are identified from all measured tracks. A preselection then already removes a large part of the background. After the preselection the six likelihood selections for the different decays are applied. The relative likelihoods are designed to separate  $W^+W^- \rightarrow q\bar{q}\ell\bar{\nu}$  events from the dominant  $e^+e^- \rightarrow q\bar{q}(\gamma)$  background. In the end, events which have passed more than one of the six likelihood discriminants are reclassified by further relative likelihoods.

### The Lepton Candidate

The identification of the best lepton candidates out of all measured tracks proceeds in the following way: Six probabilities—corresponding to the six decay chains—are constructed from variables which take the energy or momentum and the spatial isolation of the track into account; up to eight variables are used. The track with the highest probability is taken as the lepton in each class. The correct track is identified in 98.1% and 99.1% of the events in the  $W^+W^- \rightarrow q\bar{q}e\bar{\nu}$  and  $W^+W^- \rightarrow q\bar{q}\mu\bar{\nu}$  cases. Even in the  $W^+W^- \rightarrow q\bar{q}\tau\bar{\nu}$  case a correct identification is achieved in 79.5% of the events (the identification in this decay channel is much more difficult, especially for the hadronic decays of the primary tau lepton, since hadrons originating from the tau decay can intermix with hadrons which belong to the two jets of the second W boson).

<sup>3</sup>At a center-of-mass energy of  $\sqrt{s} \approx 200$  GeV, the initial fragmentation creates on average about 10 tracks per primary quark [41]. Thus, events which have only a small number of hadronic tracks are unlikely to have originated from the semileptonic decay of a W boson pair.

<sup>4</sup>The tau lepton decays into one charged hadron h (usually a  $\pi^\pm$  or a  $K^\pm$ ), n neutral  $\pi^0$  mesons and the corresponding neutrino.

<sup>5</sup>The tau lepton decays into 3 charged hadrons h (usually  $\pi^\pm$  or  $K^\pm$ ), n neutral  $\pi^0$  mesons and the corresponding neutrino.

### The Preselection

The purpose of the preselection, which follows the lepton identification, is to remove events which originate clearly from the background source  $Z^0 \rightarrow q\bar{q}$ . The rejection of these events improves the performance of the subsequent likelihood selections.

For the preselection the event is reconstructed—individually in all six decay chains—to the required signature of a  $W^+W^- \rightarrow q\bar{q}\ell\bar{\nu}$  event by removing the best lepton candidates and forcing the remaining tracks and clusters to 2 jets<sup>6</sup>. The jet energies are globally corrected for double counting of the energy of charged particles which leave signals in the central tracking system as well as in the calorimeters [42].

After the reconstruction, cuts are applied on variables which describe the visible energy, the energy deposited in the ECAL, the lepton energy and momentum, the number of tracks and clusters, the energy registered in the Forward detector, the energy of the highest energetic isolated photon, the invariant mass, the angle between the missing momentum, and the lepton and the probability of the lepton identification. In the  $W^+W^- \rightarrow q\bar{q}e\bar{\nu}$  channel a further cut is made on the ISR energy to suppress single photon radiative  $Z^0$  returns in which the photon is converted to an electron-positron pair in the detector.

The preselection in the  $W^+W^- \rightarrow q\bar{q}\tau\bar{\nu}$  channels uses additional cuts on variables which describe the isolation and the polar angle of the lepton candidates, the polar angle of the missing momentum and the energy of the dijet system.

The preselection achieves a purity (efficiency) of 28% (97.7%), 22% (98.1%), and 17% (77.2%) in the  $W^+W^- \rightarrow q\bar{q}e\bar{\nu}$ ,  $W^+W^- \rightarrow q\bar{q}\mu\bar{\nu}$ , and  $W^+W^- \rightarrow q\bar{q}\tau\bar{\nu}$  channels, respectively.

### The Likelihood Selection

For events passing the preselection, a relative likelihood method is used to distinguish  $W^+W^- \rightarrow q\bar{q}\ell\bar{\nu}$  events from the dominant background  $Z^0 \rightarrow q\bar{q}$ . Only events failing the  $W^+W^- \rightarrow q\bar{q}e\bar{\nu}$  and  $W^+W^- \rightarrow q\bar{q}\mu\bar{\nu}$  likelihood selection are considered as  $W^+W^- \rightarrow q\bar{q}\tau\bar{\nu}$  candidates;  $W^+W^- \rightarrow q\bar{q}\tau\bar{\nu}$  events which have been selected by the  $W^+W^- \rightarrow q\bar{q}e\bar{\nu}$  and  $W^+W^- \rightarrow q\bar{q}\mu\bar{\nu}$  are recovered later at the event categorization stage.

Each of the six decay chains uses a certain set of variables to discriminate signal from background events. The likelihood used in each decay chain is given by the product of the relative likelihoods for the individual variables. The relative likelihood is defined as

$$\mathcal{L} = \frac{\mathcal{L}_{\text{signal}}}{\mathcal{L}_{\text{signal}} + f \times \mathcal{L}_{q\bar{q}}}, \quad (7.1)$$

<sup>6</sup>See section 7.2 for a detailed discussion of the event reconstruction.

where  $\mathcal{L}_{\text{signal}}$  is the signal probability,  $\mathcal{L}_{q\bar{q}}$  the background likelihood and the normalization factor  $f$  the ratio of the preselected background to signal cross section, as taken from Monte Carlo.

The six likelihood selections use up to 15 variables, which describe the energy and isolation of the lepton candidate, the visible and missing energy, the total transverse momentum, the polar angle of the missing momentum, the angle between the lepton and the missing momentum and the angle between the lepton and the nearest jet, the scale at which the jet finder splits the event from two to three jets, the probability of a fit to the  $Z^0 \rightarrow q\bar{q}(\gamma)$  hypothesis, the invariant mass, the energy of the dijet system, the minimum number of tracks in a jet, and the number of tracks in the jet which contains the lepton, when the whole event—including the lepton—is forced into three jets.

The likelihood distributions for the  $W^+W^- \rightarrow q\bar{q}e\bar{\nu}$ ,  $W^+W^- \rightarrow q\bar{q}\mu\bar{\nu}$ , and  $W^+W^- \rightarrow q\bar{q}\tau\bar{\nu}$  channels are shown in figure 7.1. In order to be selected an event's likelihood must exceed a value of 0.5.

After the likelihood selection, the 4-fermion background is rejected with cuts on certain variables which are specific for the background process. Five 4-fermion background processes are considered:  $e^+e^- \rightarrow q\bar{q}\mu^+\mu^-$ ,  $e^+e^- \rightarrow q\bar{q}\tau^+\tau^-$ ,  $e^+e^- \rightarrow q\bar{q}e^+e^-$ ,  $e^+e^- \rightarrow W\nu$ , and  $e^+e^- \rightarrow q\bar{q}\nu\bar{\nu}$ .

### The Event Classification

The final step in the  $W^+W^- \rightarrow q\bar{q}\ell\bar{\nu}$  selection is the event categorization, which proceeds in four steps:

1. Events passing both the  $W^+W^- \rightarrow q\bar{q}e\bar{\nu}$  and  $W^+W^- \rightarrow q\bar{q}\mu\bar{\nu}$  likelihood cuts are classified as either  $W^+W^- \rightarrow q\bar{q}e\bar{\nu}$  or  $W^+W^- \rightarrow q\bar{q}\mu\bar{\nu}$ .
2. Events passing the  $W^+W^- \rightarrow q\bar{q}e\bar{\nu}$  likelihood cut are classified either as  $W^+W^- \rightarrow q\bar{q}e\bar{\nu}$ ,  $W \rightarrow \tau\nu_\tau \rightarrow e\nu_e\nu_\tau$ , or  $W \rightarrow \tau\nu_\tau \rightarrow h(n\pi^0)\nu_\tau\nu_\tau$ .
3. Events passing the  $W^+W^- \rightarrow q\bar{q}\mu\bar{\nu}$  likelihood cut are classified either as  $W^+W^- \rightarrow q\bar{q}\mu\bar{\nu}$ ,  $W \rightarrow \tau\nu_\tau \rightarrow \mu\nu_\mu\nu_\tau$ , or  $W \rightarrow \tau\nu_\tau \rightarrow h(n\pi^0)\nu_\tau\nu_\tau$ .
4. Events selected by more than one of the four  $W^+W^- \rightarrow q\bar{q}\tau\bar{\nu}$  decay chains are categorized as one of them.

Each of the four categorizations uses one or more additional likelihood discriminants. As can be seen in the steps 2 and 3 the  $W^+W^- \rightarrow q\bar{q}\tau\bar{\nu}$  events which were wrongly selected as  $W^+W^- \rightarrow q\bar{q}e\bar{\nu}$  or  $W^+W^- \rightarrow q\bar{q}\mu\bar{\nu}$  candidates (about 33% of the  $W^+W^- \rightarrow q\bar{q}\tau\bar{\nu}$  events) can be recovered at this stage of the event selection.

### Trackless Events

The  $W^+W^- \rightarrow q\bar{q}\ell\bar{\nu}$  event selection also tries to recover events in which no lepton track has been found. This extends the selection beyond the tracking acceptance

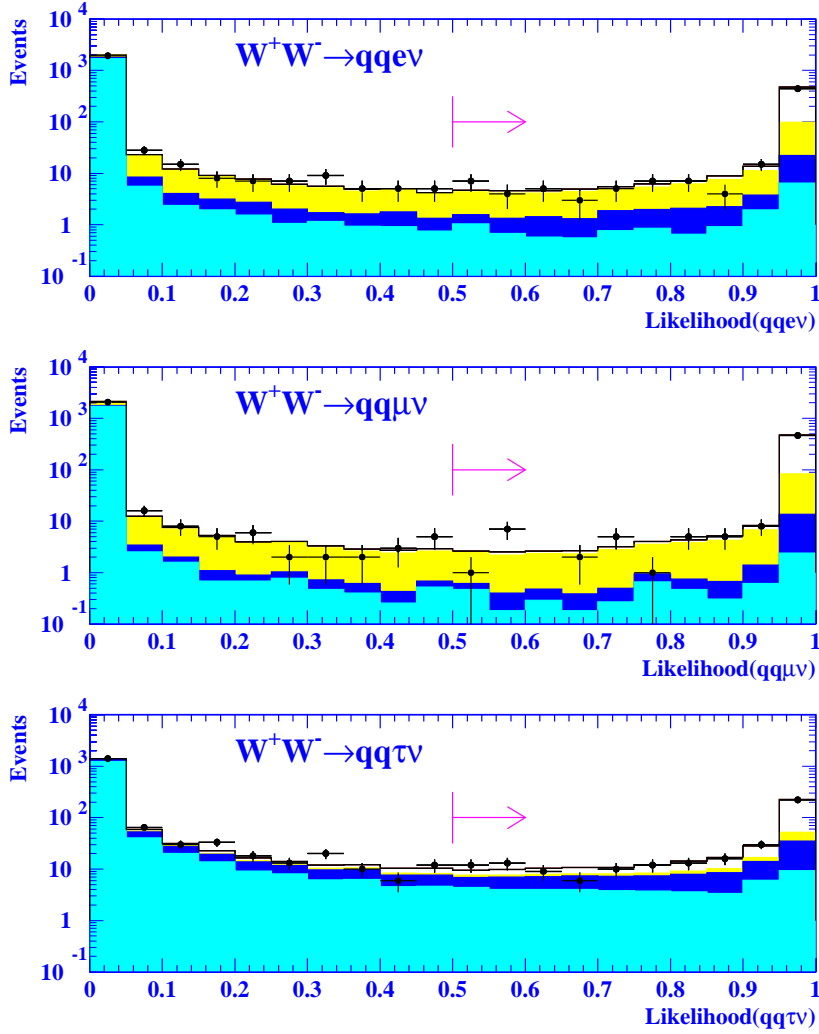


**Figure 7.1:** Likelihood distributions for the  $W^+W^- \rightarrow q\bar{q}\ell\bar{\nu}$  selections. The  $\sqrt{s} = 189$  GeV data (points) are compared to the Monte Carlo expectation (histograms). The open histograms show the signal contribution, the yellow (light grey) histograms the contamination from the other two decay channels, the dark blue (dark grey) histograms the non-WW four-fermion background, and the light blue (grey) histograms show the two-fermion background. The  $W^+W^- \rightarrow q\bar{q}\tau\bar{\nu}$  plot shows the largest of the discriminants of the different tau decay chains.

of the OPAL detector and recovers events in which the lepton is within the tracking acceptance, but no track was reconstructed.

Two different *Trackless selections*, one for  $W^+W^- \rightarrow q\bar{q}e\bar{\nu}$  events, the other for  $W^+W^- \rightarrow q\bar{q}\mu\bar{\nu}$  events are implemented.

The *Trackless selections* search for evidence of a lepton by looking for clusters in the electromagnetic calorimeter which are not associated with a track that passed the standard track quality cuts mentioned at the beginning of this chapter. Additional information is then used to tag such a cluster as a lepton candidate, termed a *blob*. For *electron blobs* only a significant isolated energy deposit in the electromagnetic calorimeter is required, while *muons blobs* require—in addition to a cluster in the ECAL—evidence of a Minimum Ionizing Particle (MIP) in the muon chambers or the pole-tip calorimeter.

The *Trackless  $W^+W^- \rightarrow q\bar{q}e\bar{\nu}$  selection* requires an *electron blob* with an ECAL energy in a certain range; several cuts on the number of tracks in the central tracker, the number of calorimeter blocks with hits, the energy in the forward detector, the visible energy, the angle of the missing momentum, the angle between the lepton candidate and the nearest jet, the probability of a fit to the  $Z^0 \rightarrow q\bar{q}(\gamma)$  hypothesis, and the mass of the 2-jet system are applied to reduce the  $Z^0 \rightarrow q\bar{q}$  background. This selection achieves a purity of 85%.

The *Trackless  $W^+W^- \rightarrow q\bar{q}\mu\bar{\nu}$  selection* requires a *muon blob* and applies cuts on the visible energy, the total transverse momentum, the angle between the lepton candidate and the missing momentum, and on the probability of a fit to the  $Z^0 \rightarrow q\bar{q}(\gamma)$  hypothesis. This selection achieves a purity of 95%.

### Selection Efficiency

The overall performance of the  $W^+W^- \rightarrow q\bar{q}\ell\bar{\nu}$  selection is summarized in the efficiency matrix, listed in table 7.1. The selection achieves purities of 94.0%, 97.3%, and 79.8% in the  $W^+W^- \rightarrow q\bar{q}e\bar{\nu}$ ,  $W^+W^- \rightarrow q\bar{q}\mu\bar{\nu}$ , and  $W^+W^- \rightarrow q\bar{q}\tau\bar{\nu}$  decay channels, respectively.

Selected as	Generated as		
	$W^+W^- \rightarrow q\bar{q}e\bar{\nu}$	$W^+W^- \rightarrow q\bar{q}\mu\bar{\nu}$	$W^+W^- \rightarrow q\bar{q}\tau\bar{\nu}$
$W^+W^- \rightarrow q\bar{q}e\bar{\nu}$	$85.42 \pm 0.84\%$	$0.12 \pm 0.01\%$	$3.80 \pm 0.50\%$
$W^+W^- \rightarrow q\bar{q}\mu\bar{\nu}$	$0.15 \pm 0.01\%$	$89.16 \pm 0.80\%$	$4.30 \pm 0.50\%$
$W^+W^- \rightarrow q\bar{q}\tau\bar{\nu}$	$4.55 \pm 0.50\%$	$4.41 \pm 0.50\%$	$68.44 \pm 1.44\%$

**Table 7.1:** Efficiency matrix for the OPAL  $W^+W^- \rightarrow q\bar{q}\ell\bar{\nu}$  selection at a center-of-mass energy of  $\sqrt{s} = 189$  GeV [39].

### 7.1.4 The $W^+W^- \rightarrow q\bar{q}q\bar{q}$ Event Selection

The  $W^+W^- \rightarrow q\bar{q}q\bar{q}$  event selection [40] is only described for completeness. Since it is only applied to events which have already failed the  $W^+W^- \rightarrow q\bar{q}\ell\bar{\nu}$

selection, it has no influence on the presented analysis. Therefore, the discussion will be kept very brief.

The  $W^+W^- \rightarrow q\bar{q}q\bar{q}$  selection aims to distinguish signal events from the dominant background of  $Z^0 \rightarrow q\bar{q}$  where the two quarks fragment into four jets. Since this final state has almost the same topology as the signal, cut based methods become very inefficient. Therefore, a likelihood selection is employed.

A preselection is used to remove obvious non  $W^+W^- \rightarrow q\bar{q}q\bar{q}$  events, by using cuts on the visible energy and invariant mass of the event, on the QCD matrix element for 4-jet production in  $Z^0 \rightarrow q\bar{q}$ , on the number and multiplicity of the jets, and by requiring a failed  $W^+W^- \rightarrow q\bar{q}\ell\bar{\nu}$  selection of this event. These variables are all based on the fact that in  $W^+W^- \rightarrow q\bar{q}q\bar{q}$  events the available center-of-mass energy is transformed into hadrons. The efficiency of this preselection is 93% while it removes over 96% of the  $Z^0 \rightarrow q\bar{q}$  background. A purity of 62.6% is achieved after the preselection.

The likelihood selection is based on only four variables. Instead of constructing a probability function (PDF) for individual variable, the selection uses a coordinate transformation to force each distribution to a Gaussian of width 1 and combines them to a multi-dimensional PDF. The likelihood variables are two matrix elements, the QCD matrix element from the preselection and a 4-fermion matrix element for the  $W$ -pair production of such an event, a variable which describes the topology, the sphericity and the scale at which the DURHAM jet finder [43] splits the event from four to five jets.

The  $W^+W^- \rightarrow q\bar{q}q\bar{q}$  selection reaches an efficiency of 86.4% and a purity of 78.5%.

## 7.2 Reconstruction of $W^+W^- \rightarrow q\bar{q}\ell\bar{\nu}$ Events

This section describes the reconstruction of semileptonic events. After an event has been identified as a  $W^+W^- \rightarrow q\bar{q}\ell\bar{\nu}$  candidate, it is reconstructed to be consistent with the hypothesis of two primary  $W$  bosons. In a semileptonic decay one  $W$  boson decays to a quark-antiquark pair and leads to two high multiplicity jets (containing approximately 10 charged hadronic tracks each [41]), the other  $W$  boson decays into a lepton-neutrino pair and leads to one charged track or a low multiplicity jet (1 or 3 charged hadronic tracks) in the case that the primary tau lepton decays hadronically.

### 7.2.1 The Lepton

The best lepton candidate is already determined in the  $W^+W^- \rightarrow q\bar{q}\ell\bar{\nu}$  event selection. For a primary electron or muon or for a tau lepton that decayed to a lepton-neutrino pair the lepton candidate is made of a single track and its *associated clus-*

ters<sup>7</sup> in the calorimeter. For the decay chains  $W \rightarrow \tau \nu_\tau \rightarrow h(n\pi^0) \nu_\tau \nu_\tau$  and  $W \rightarrow \tau \nu_\tau \rightarrow 3h(n\pi^0) \nu_\tau \nu_\tau$  the lepton candidate consists of one or three charged hadronic tracks and associated clusters in the calorimeters, as well as clusters which originate from  $\pi^0$  created in the tau decay<sup>8</sup>.

The following description applies to normal  $W^+W^- \rightarrow q\bar{q}\ell\bar{\nu}$  events, the procedure used for *Trackless events* is described in section 7.2.3.

The energy information for an electron originating either from a  $W \rightarrow e\nu_e$  or  $W \rightarrow \tau \nu_\tau \rightarrow e\nu_e \nu_\tau$  decay is obtained from the electromagnetic calorimeter, which has a superior resolution for high energy electrons than the central tracking system. The electron direction is taken from the tracking system.

For muons, originating either from a  $W \rightarrow \mu \nu_\mu$  or  $W \rightarrow \tau \nu_\tau \rightarrow \mu \nu_\mu \nu_\tau$  decay, both the momentum and the direction are taken from the tracking system, since the muon does not interact much with the calorimeters and generally escapes from the detector.

For hadronic decays of the tau lepton, i.e.  $W \rightarrow \tau \nu_\tau \rightarrow h(n\pi^0) \nu_\tau \nu_\tau$  and  $W \rightarrow \tau \nu_\tau \rightarrow 3h(n\pi^0) \nu_\tau \nu_\tau$  decays, the lepton energy is estimated by the sum of the momenta of the tau candidate tracks and any unassociated calorimeter clusters within a certain cone around the tau direction—thus taking into account the energy of  $\pi^0$  mesons and photons produced in the decay, which are preferentially emitted in the forward direction of the highly relativistic tau lepton; this leptonic energy is only used in the event selection—since the energy of the tau-neutrino in the tau decay is unknown, the energy of the primary tau lepton cannot be reconstructed. The tau direction is taken from the tracks measured in the central tracking system. This is justified by the high energy of the tau lepton which leads to a high boost value; all decay products are emitted in the direction of the tau momentum when observed in the laboratory frame.

### 7.2.2 Evil Taus

The reconstruction of  $W^+W^- \rightarrow q\bar{q}\tau\bar{\nu}$  events is complicated by the fact that the primary tau lepton cannot be measured directly<sup>9</sup>, but that only its decay products can be observed. Furthermore the decay products have less energy than a typical lepton candidate in  $W^+W^- \rightarrow q\bar{q}e\bar{\nu}$  or  $W^+W^- \rightarrow q\bar{q}\mu\bar{\nu}$  events, since unobservable neutrinos are emitted in the tau decays. The determination of the best lepton candidate track(s) by the event selection is therefore much more difficult, especially in the case that the tau lepton decays to hadrons which can intermix with the hadrons belonging to the two jets of the other W boson.

<sup>7</sup>The term *associated clusters* refers to clusters in the calorimeter with a track in the central tracking chambers pointed at them.

<sup>8</sup>The  $\pi^0$  immediately decays electromagnetically, the dominant decay modes are  $\pi^0 \rightarrow \gamma\gamma$  and  $\pi^0 \rightarrow e^+e^-\gamma$  with branching ratios of approximately 99% and 1%, respectively.

<sup>9</sup>The typical energy of the primary tau lepton is 1/2 of the beam energy; even at center-of-mass energies of 210 GeV this leads to a mean flight length of less than 3 mm from the interaction point, a distance in which no tracking is possible in the detector.



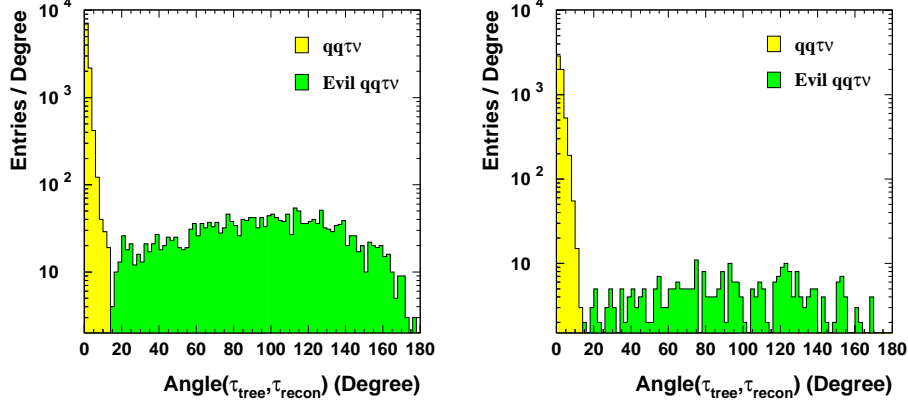


**Figure 7.2:** Deviation of the reconstructed direction of flight from the true direction of flight of the tau lepton in  $W^+W^- \rightarrow q\bar{q}\ell\bar{\nu}$  events. The left plot shows the distribution for the  $W \rightarrow \tau\nu_\tau \rightarrow h(n\pi^0)\nu_\tau\nu_\tau$  and  $W \rightarrow \tau\nu_\tau \rightarrow 3h(n\pi^0)\nu_\tau\nu_\tau$  event classes, the right plot for the  $W \rightarrow \tau\nu_\tau \rightarrow e\nu_e\nu_\tau$  and  $W \rightarrow \tau\nu_\tau \rightarrow \mu\nu_\mu\nu_\tau$  classes. In each case the yellow (light grey) histogram depicts properly identified lepton candidates, the green (grey) histogram corresponds to mis-identified lepton candidates by the event selection. The results are taken from a Monte Carlo study at  $\sqrt{s} = 189$  GeV.

Figure 7.2 shows the difference between the reconstructed direction of flight and the true direction of flight of the tau lepton. The left plot shows the distribution for taus that decay into hadrons,  $W \rightarrow \tau\nu_\tau \rightarrow h(n\pi^0)\nu_\tau\nu_\tau$  and  $W \rightarrow \tau\nu_\tau \rightarrow 3h(n\pi^0)\nu_\tau\nu_\tau$  (which comprise about 70% of the tau decays), the right plot for taus that decay into electrons or muons,  $W \rightarrow \tau\nu_\tau \rightarrow e\nu_e\nu_\tau$  and  $W \rightarrow \tau\nu_\tau \rightarrow \mu\nu_\mu\nu_\tau$ . Events for which the reconstructed direction of flight of the tau lepton deviates more than  $15^\circ$  from the true direction are dubbed *Evil taus*. These events carry no useful mass information.

For hadronic tau decays an additional likelihood selection was developed to reject *Evil taus* and to identify the correct lepton candidate in these event classes. *Evil taus* in the leptonic decay classes cannot be rejected, since their identification is already based on a single track and their energy is even less defined due to the second neutrino emitted in the tau decay.

Unrejected *Evil tau* events in hadronic tau decays and mis-identified candidates in leptonic tau decays distort the expected distribution of the event W masses and have to be considered as an additional background for the W mass measurement in the  $W^+W^- \rightarrow q\bar{q}\ell\bar{\nu}$  channel.

### A Rejection Scheme for Misidentified Tau Lepton Candidates

In approximately 22% of events the  $W^+W^- \rightarrow q\bar{q}\ell\bar{\nu}$  in which the tau further decays into hadrons,  $W \rightarrow \tau\nu_\tau \rightarrow h(n\pi^0)\nu_\tau\nu_\tau$  and  $W \rightarrow \tau\nu_\tau \rightarrow 3h(n\pi^0)\nu_\tau\nu_\tau$ , the

event selection algorithm incorrectly identifies the lepton candidate particles.

In order to recuperate some of these *Evil tau* events for the W mass analysis an additional specialized likelihood selection [44] is applied after the event selection to all  $W^+W^- \rightarrow q\bar{q}\tau\bar{\nu}$  events that have been identified as a member of either the  $W \rightarrow \tau\nu_\tau \rightarrow h(n\pi^0)\nu_\tau\nu_\tau$  or the  $W \rightarrow \tau\nu_\tau \rightarrow 3h(n\pi^0)\nu_\tau\nu_\tau$  decay chains.

The *Evil tau* likelihood is based on five variables:

- $(\cos \theta_W \cdot Q_W)$ , where  $\theta_W$  is the production angle of the hadronically decaying W boson and  $Q_W$  is the charge of the leptonically decaying W boson
- The cosine of the minimum angle between the tau track(s) assigned by the event selection and the nearest jet
- The cosine of the angle between the two jets of the hadronically decaying W boson
- The momentum of the tau track(s)
- The energy deposited by the tau candidate in the electromagnetic calorimeter

Events for which the event selection correctly identifies the tau track(s) tend to have high likelihood values. If the likelihood for a given  $W^+W^- \rightarrow q\bar{q}\tau\bar{\nu}$  decay is less than 0.4, the event is reclustered with the DURHAM algorithm [43] into three jets using all available tracks. The jet with the minimum mass is taken to be the tau jet. If it differs from the original tau track assignment and there are fewer than six charged tracks in the jet, then this jet is taken as the new best lepton candidate. Otherwise the best lepton candidate from the event selection is kept.

Monte Carlo studies show that the *Evil tau rejection* recuperates about 27% of genuine *Evil tau* events while it mistakenly transforms only 3% good events to *Evil taus*, leading to an overall gain of the reconstruction efficiency of about 3.5%. An improvement on the mass measurement in the  $W^+W^- \rightarrow q\bar{q}\tau\bar{\nu}$  channel of about 2% is estimated, compare appendix A.

Figure 7.3 shows a comparison of the distributions of the fitted event W mass in  $W^+W^- \rightarrow q\bar{q}\tau\bar{\nu}$  events before and after the *Evil tau rejection* has been applied to correct mis-identified tau lepton candidates, plotted as the histogram and the points, respectively. The mis-identification of the tau usually leads to a higher energy in the hadronic jet system. The increase in energy of the jet to which the tracks of the tau decay products were associated more than compensates the energy loss in the jet from which tracks were identified as the lepton candidate and thus excluded. The angle between the two jets usually changes only very little. In a kinematic fit, the overall increased jet energy leads to a higher reconstructed mass for the W boson, since the leptonic part in  $W^+W^- \rightarrow q\bar{q}\tau\bar{\nu}$  events has only negligible influence on the result of the fit.

The application of the *Evil tau rejection* results in a shift of events from the high mass tail of the distribution to the peak region, leading to an improved resolution for the mass measurement in the  $W^+W^- \rightarrow q\bar{q}\tau\bar{\nu}$  channel.

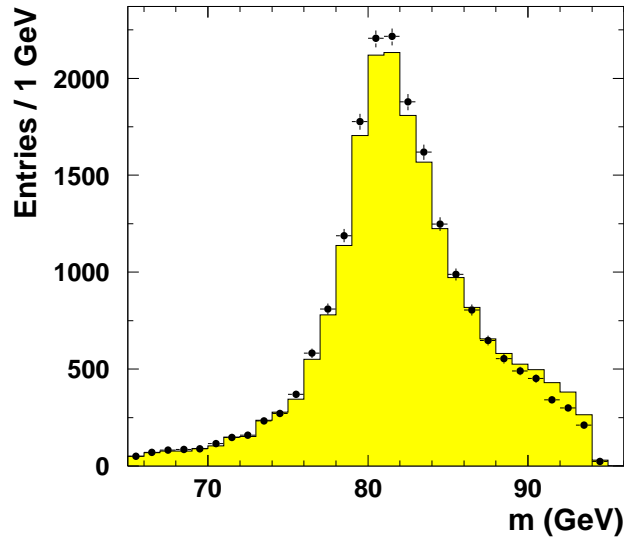


**Figure 7.3:** Distribution of the fitted  $W$  mass for  $W^+W^- \rightarrow q\bar{q}\tau\bar{\nu}$  events before—histogram—and after—points—the *Evil tau rejection* has been applied to correct mis-identified tau lepton candidates. The results are taken from a Monte Carlo study at  $\sqrt{s} = 189$  GeV; the error bars on the points were added to give an indication of the statistical uncertainty of the individual bin contents.

### Evil Tau Background

While the rejection scheme for mis-identified tau lepton candidates described above improves the reconstruction efficiency, a large fraction of about 15% of the  $W^+W^- \rightarrow q\bar{q}\tau\bar{\nu}$  events remains reconstructed wrongly, including events from the  $W \rightarrow \tau\nu_\tau \rightarrow e\nu_e\nu_\tau$  and  $W \rightarrow \tau\nu_\tau \rightarrow \mu\nu_\mu\nu_\tau$  decay chains. Approximately 66% of these events pass the data quality cuts (see chapter 8.2.4) and enter the data sample used in the mass analysis.

The *Evil tau* events carry no useful mass information and distort the distribution of the  $W$  event masses from the expected shape, as can be seen in figure 7.4 (left). The plot compares the  $W$  event mass distributions of properly reconstructed events (yellow/light grey histogram) with that of *Evil tau* events (green/grey histogram). The right side of figure 7.4 shows the  $W$  event mass distributions of *Evil taus* for different values of the  $W$  mass in the Monte Carlo generation. The shape of the mass distribution for *Evil taus* depends only weakly on the mass of the  $W$  boson and can thus be treated as an additional background source in the  $W^+W^- \rightarrow q\bar{q}\tau\bar{\nu}$  channel. The shape of the *Evil tau* event mass distribution and the fraction of *Evil taus* in the data sample can be estimated from Monte Carlo and can be taken

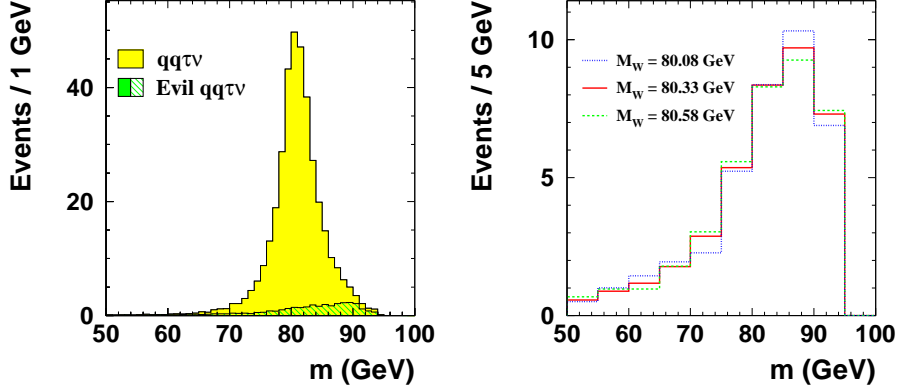


**Figure 7.4:** Left: Distribution of the fitted W mass for  $W^+W^- \rightarrow q\bar{q}\tau\nu$  events. The yellow (light grey) histogram shows the distribution for properly reconstructed events, the green (grey) histogram for *Evil tau* events. Right: Distributions of the fitted W mass for *Evil tau* events for different values of the W boson mass used in the generation of the Monte Carlo sample. Shown are the results of a Monte Carlo study at  $\sqrt{s} = 189$  GeV, normalized to the integrated data luminosity.

into account in the fit function used to determine the mass of the W boson, see chapter 8.2.3.

### 7.2.3 Events without a Lepton Track

Events which were classified as *Trackless*  $W^+W^- \rightarrow q\bar{q}e\nu$  and  $W^+W^- \rightarrow q\bar{q}\mu\nu$  events by the event selections, compare section 7.1.3, can still be used in the mass analysis.

*Trackless*  $W^+W^- \rightarrow q\bar{q}e\nu$  events are included in the  $W^+W^- \rightarrow q\bar{q}e\nu$  class for the mass extraction; the energy and direction of the primary electron are determined solely from the ECAL information.

*Trackless*  $W^+W^- \rightarrow q\bar{q}\mu\nu$  events are included in the  $W^+W^- \rightarrow q\bar{q}\tau\nu$  class, since as for  $W^+W^- \rightarrow q\bar{q}\tau\nu$  events there is essentially no energy information for the muon without the momentum measurement in the central tracking system. The direction of the primary muon is determined from the information of the electromagnetic and hadronic calorimeters.

Figure 7.5 shows the distributions of the reconstructed W mass for *Trackless*  $W^+W^- \rightarrow q\bar{q}e\nu$  and  $W^+W^- \rightarrow q\bar{q}\mu\nu$  events after a kinematic fit with an equal mass constraint has been applied compared to the distribution of  $W^+W^- \rightarrow q\bar{q}e\nu$  and  $W^+W^- \rightarrow q\bar{q}\mu\nu$  events with a properly reconstructed lepton track. The scale of the *Trackless* events has been magnified by a factor of 10. As can be seen the *Trackless* events contain almost as much mass information as events with properly reconstructed leptons.

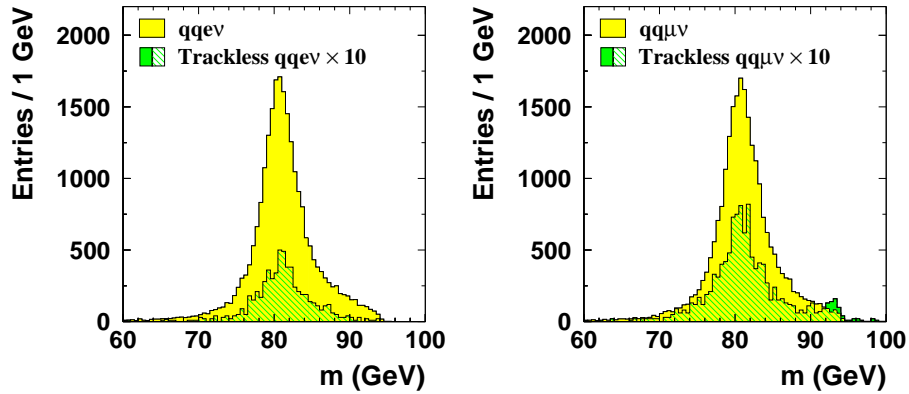


**Figure 7.5:** Distribution of the fitted  $W$  mass for  $W^+W^- \rightarrow q\bar{q}\ell\bar{\nu}$  (left) and  $W^+W^- \rightarrow q\bar{q}\mu\bar{\nu}$  (right) events. The green (grey) histogram corresponds to *Trackless events*, the yellow (light grey) histogram shows the distribution of events with a properly reconstructed lepton track. The histograms for the *Trackless events* have been magnified by a factor 10. Monte Carlo study at  $\sqrt{s} = 189$  GeV.

### 7.2.4 The Non-Leptonic Part

After excluding the tracks and clusters associated with the best lepton candidate the remainder of the event is forced into two jets by a jet finder using the DURHAM algorithm<sup>10</sup> [43].

The DURHAM jetfinder combines particles to jets in an iterative algorithm, based on the value

$$y_{ij} = \frac{2 \min(E_i^2, E_j^2)}{s} (1 - \cos \theta_{ij}), \quad (7.2)$$

of two jets  $i$  and  $j$ . Here  $E_i$  is the energy of the  $i$ -th jet,  $\sqrt{s}$  the center-of-mass energy,  $\theta_{ij}$  the angle between the  $i$ -th and  $j$ -th jet. The value of  $y_{ij}$  between two jets is small if the angle between them is small or one of them has a low energy.

The initial jets are the individually measured particles themselves. The two jets with the smallest value  $y$  are combined to form a new jet by adding their 4-momenta; the calculation is iterated until only two jets remain. The value of  $y$  at which a  $n$  jet configuration is reduced an  $n - 1$  jets,

$$y_{(n-1)n} = \min_{1 \leq i, j \leq n, i \neq j} \left( \frac{2 \min(E_i^2, E_j^2)}{s} (1 - \cos \theta_{ij}) \right), \quad (7.3)$$

is called the  $(n - 1)n$  splitting scale and is often used as an input to selection likelihoods or cuts.

<sup>10</sup>The DURHAM algorithm is the standard jet finder used in the  $W$ -pair analyses in the OPAL collaboration. Studies within the  $WW$  working group have shown no advantage of other jet finders over the DURHAM scheme.

To obtain the energy and momentum of the jets from the combined information of the tracking system and the calorimeters, one has to avoid double counting of the momenta of charged hadrons, which leave a track as well as an energy deposit in the ECAL and HCAL system.

In a hadronic final state (e.g. in the hadronic decay of a W boson) about 2/3 of the total energy is carried by charged particles, which are usually measured with better momentum and angular resolution in the central tracking system than in the calorimeters—except for high energy electrons which rarely belong to a jet—while the energy of neutral particles can only be measured in the latter system.

To obtain the best energy resolution, the momenta of charged particles should therefore be determined from the information of the tracking chambers.

Unfortunately the charged and neutral particles of a jet are intermixed in a narrow space region and cannot be separated by the calorimeters. To use the energy information from the calorimeters for the neutral particles, the contribution of the charged particles in a calorimeter cluster has to be removed to avoid a wrong result.

For the OPAL detector two different approaches to correct the jet energies have been developed: the GCE (Globally Corrected Energy) algorithm [42] and the MT (Matching) algorithm [45–47]. The GCE algorithm performs a global correction of the jet energy, based only on its value and the geometric location of the jet, while the MT algorithm corrects the energy for each track in a jet separately.

This work uses the more advanced MT algorithm to correct the energies of jets. The algorithm starts by matching tracks to calorimeter clusters by using the extrapolated track to the electromagnetic or hadronic calorimeter, the cluster center and boundaries as well as the energy of the cluster and the expected calorimeter response as calculated from the track momentum. Three cases can now occur for the calculation of the total jet energy:

- A track and a cluster are not associated. In this case both the track and the cluster are accepted.
- The energy of an associated cluster matches the expectation from the track momentum within a certain tolerance. In this case only the track is accepted.
- The energy of an associated cluster exceeds the expectation from the track momentum. In this case the track and the cluster energy reduced by the expected energy are accepted.

The MT algorithm also implements compensations for the different response of the electromagnetic and hadronic calorimeters to hadrons and thus further improves the energy measurement of the jets.

After each track has been corrected for double counting, the 4-momenta of the jets are calculated as the sum of the 4-momenta of the individual tracks belonging to them; the track-jet association is defined by the jet-finder.

In principle it is possible to calculate the mass of the W boson which has decayed into hadrons from this information; the W mass is given by the invariant

mass of the dijet system, see section 7.3.1. Nevertheless, if the jet momenta are used together with the momentum of the lepton and the estimated errors of these quantities as the input of a kinematic fitting routine, see section 7.3.2, a better resolution on the W mass can be obtained.

### 7.2.5 Monte Carlo Detector Recalibration

The simulation of physics events is based on a detailed description of the detector and the response of its different components. The agreement between real and simulated data is very good, but slight discrepancies between the actual measurements and the Monte Carlo description introduced e.g. by mis-adjustments or aging of detector components cannot be ruled out. To calibrate the detector and to tune the Monte Carlo simulation, data collected at the  $Z^0$  resonance peak<sup>11</sup> can be used. The precise knowledge of the properties of the  $Z^0$  boson, as determined in the six years of the LEP1 era, allows the comparison with the simulation with high precision.

Within the scope of the WW analysis framework, the results of the analysis of the  $Z^0$  data taken in 1998 are used to correct the energy scale, the energy resolution (the error of the energy measurement), the angular offsets and the angular resolutions of jets and leptons as a function of the  $\theta$  and  $\phi$  angles [48]. Only simulated events are modified, the actual data collected with OPAL is left unchanged.

The study of systematic uncertainties related to the detector calibration is also standardized using the results of the  $Z^0$  data: Instead of applying the fixed corrections to the simulated Monte Carlo events, they are varied randomly within their statistical errors (as determined from the finite statistics of recorded  $Z^0$  data) from event to event, thus imprinting the uncertainties in the calibration on the simulated data. A comparison with the same set of Monte Carlo data corrected with the nominal calibration coefficients then yields an estimate of the systematic uncertainty associated with the individual calibration issues.

## 7.3 Determination of the Invariant Mass

After an event has been reconstructed—tracks and clusters have been identified and combined as lepton candidates or jets, and the jet energies have been corrected for double counting in the calorimeters—the masses of the two W bosons in that particular event can be determined by calculating the invariant masses of the decay products associated with each W boson. The distribution of the W event masses can then be used in a measurement of the mass of the W boson itself.

In semileptonic W-pair decays,  $W^+W^- \rightarrow q\bar{q}\ell\bar{\nu}$ , the reconstruction of the event at the detector level is not complete, since the neutrino is not observed directly. Additional physical constraints, like energy and momentum conservation, must be imposed to restore the missing information and to arrive at a complete reconstruction

---

<sup>11</sup>To provide this data to the experiments, the LEP accelerator is running at center-of-mass energies of  $\sqrt{s} \approx 91$  GeV for short times each year.

of these events.

We start the discussion with the description of the scaled hadronic mass which uses only the measured jet direction and energies, the energy conservation and an equal mass constraint. The scaled hadronic mass can be also be used to estimate the behavior of the reconstructed event  $W$  mass to changes of the input parameters as the calculation is very simple and straightforward.

A more complete reconstruction of the event is possible by applying a kinematic fit, which uses the jet and lepton momenta, their directions, and their errors as input variables to determine the best estimates of the measured quantities by applying energy and momentum conservation in a least-square minimization. An additional equal mass constraint can be used to further improve the mass resolution.

### 7.3.1 Scaled Hadronic Mass

The most simple, albeit not the best way, to reconstruct the mass of the  $W$  boson in a semileptonic event is to use only the information available from the two hadronic jets and to disregard the information carried by the lepton, which in any case is incomplete for  $W^+W^- \rightarrow q\bar{q}\tau\bar{\nu}$  events.

The invariant mass  $m_{\text{dijet}}$  of the dijet system can be calculated from the measured 4-momenta,

$$\begin{pmatrix} E_1 \\ \mathbf{p}_1 \end{pmatrix}, \begin{pmatrix} E_2 \\ \mathbf{p}_2 \end{pmatrix}$$

and is given by

$$m_{\text{dijet}} = \sqrt{2E_1E_2(1 - \cos\theta)}. \quad (7.4)$$

Its error is given by

$$\frac{\delta m_{\text{dijet}}}{m_{\text{dijet}}} \approx \sqrt{\left(\frac{\delta E_1}{E_1}\right)^2 + \left(\frac{\delta E_2}{E_2}\right)^2}, \quad (7.5)$$

where  $E_1$  denotes the energy of the first jet and  $E_2$  the energy of the second jet and  $\theta$  the angle between the two jets; in this calculation we assume massless jets, i.e.  $m_{1,2} = \sqrt{E_{1,2}^2 - \mathbf{p}_{1,2}^2} = 0$ . For the error estimate the uncertainty on the jet angle can be neglected compared to the uncertainty of the energy measurements. At jet energies of approximately 45 GeV the error is about 10% of the  $W$  mass. The event  $W$  boson mass calculated from the jet momenta is called the hadronic mass.

Energy conservation and an equal mass constraint can be implemented in the calculation by a scaling factor which ensures that the total energy of each  $W$  boson equals the beam energy  $\sqrt{s}/2$ ,

$$E_{1,2} \rightarrow E_{1,2} \frac{\sqrt{s}/2}{E_1 + E_2}. \quad (7.6)$$



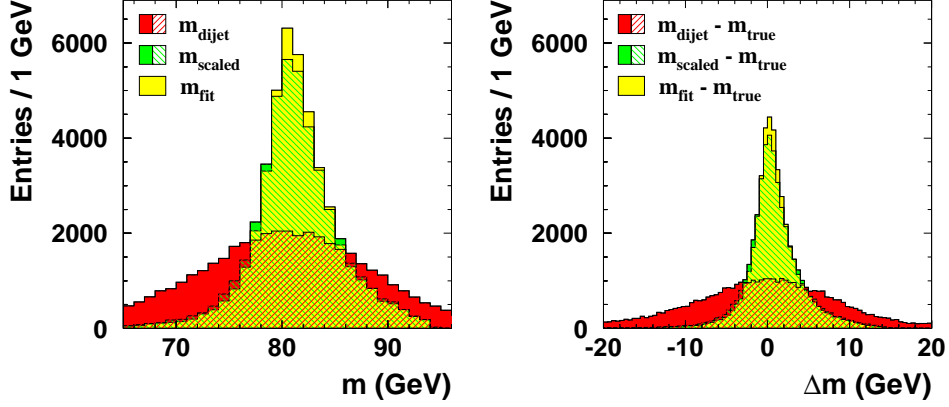


**Figure 7.6:** Left: Distribution of the hadronic mass—red (dark grey) histogram—the scaled hadronic mass—green (grey) histogram—and the fitted mass—yellow (light grey) histogram, see section 7.3.2—for Monte Carlo data at a center-of-mass energy of  $\sqrt{s} = 189$  GeV for  $W^+W^- \rightarrow q\bar{q}\ell\bar{\nu}$  events. Right: Resolution of the event  $W$  mass measurement for the three reconstruction methods.

We arrive at the formula for the scaled hadronic mass,

$$m_{\text{scaled}} = \sqrt{2E_1E_2 \left( \frac{\sqrt{s}/2}{E_1 + E_2} \right)^2 (1 - \cos \theta)}, \quad (7.7)$$

and its error,

$$\frac{\delta m_{\text{scaled}}}{m_{\text{scaled}}} \approx \frac{1}{E_1 + E_2} \sqrt{\left( \frac{E_2}{E_1} \delta E_1 \right)^2 + \left( \frac{E_1}{E_2} \delta E_2 \right)^2}. \quad (7.8)$$

The energy and equal mass constraint improve the resolution of the reconstructed  $W$  mass by a factor of 2–3.

As an example, the left side of figure 7.6 shows the distribution of the scaled hadronic mass compared to the hadronic mass for  $W^+W^- \rightarrow q\bar{q}\ell\bar{\nu}$  Monte Carlo events at a center-of-mass energy of  $\sqrt{s} = 189$  GeV. On the right side the difference between the true (mean)  $W$  mass in the event and the reconstructed mass is plotted for both methods; the RMS width of these distributions is a measure for the achievable resolution in the event  $W$  mass determination and decreases from 8 GeV for the hadronic mass to 3.5 GeV for the scaled hadronic mass.

### 7.3.2 Constrained Kinematic Fits

A different and better approach of the calculation of the invariant mass is based on a constrained kinematic fit which allows the exact implementation of equations of

constraints. The kinematic fit has the advantage that it provides the means to calculate the exact shape of the probability density function which allows a derivation of the confidence intervals for the event  $W$  mass. This error information can be further used, e.g. in the *Convolution method* which is described in chapter 8, to improve the measurement of the mass of the  $W$  boson. In addition the fit returns a probability value for its result that can be used to discriminate events which do not match the hypothesis of a semileptonic  $W$ -pair decay well, as e.g. background events. Furthermore, the kinematic fit also improves the resolution of the event  $W$  mass by about 10% compared to the scaled hadronic mass.

In a constrained fit, the best estimates to a set of parameters is determined by minimizing simultaneously the deviations of the estimated parameters from their measured values; the deviations are weighted by the measurement errors, taking into account possible correlations between the parameters. Constraints are implemented as additional terms in the  $\chi^2$ -function and allow the consideration of unmeasured parameters. Thus, the  $\chi^2$ -function is given by

$$\chi^2 = (\mathbf{p} - \hat{\mathbf{p}})_i G(\mathbf{p})_{ij} (\mathbf{p} - \hat{\mathbf{p}})_j + \text{terms for constraints}, \quad (7.9)$$

where  $\mathbf{p}$  denotes the vector of measured parameters,  $\hat{\mathbf{p}}$  the vector of the estimates and  $G$  the inverse covariance matrix of the measured parameters.

The minimization of the  $\chi^2$ -functions with respect to the parameter set ( $\hat{\mathbf{p}}$ ) yields the best estimates for the parameters, which at the same time satisfy the equations of constraint. The calculation of the parameter errors is a straightforward application of the laws of error propagation.

The number of degrees of freedom  $N_{\text{DoF}}$  of the kinematic fit is given by

$$N_{\text{DoF}} = N_{\text{meas}} - N_{\text{par}} + N_C, \quad (7.10)$$

where  $N_{\text{meas}}$  is the number of measured parameters,  $N_{\text{par}}$  the number fitted of parameters and  $N_C$  is the number of constraints.

The value of the  $\chi^2$ -function at the minimum can be used as criterion of the *goodness-of-fit*. If the error estimates are well modeled and follow Gaussian distributions, one expects  $\chi^2/N_{\text{DoF}} \approx 1$ . The probability  $P_{\chi^2}(N_{\text{DoF}})$  that a larger value than the measured  $\chi^2$  is observed in a fit with  $N_{\text{DoF}}$  degrees of freedom is:

$$P_{\chi^2}(N_{\text{DoF}}) = \int_{\chi^2}^{\infty} \frac{x^{(N_{\text{DoF}}-2)} \exp(x/2)}{\sqrt{2^{N_{\text{DoF}}}} \Gamma(N_{\text{DoF}}/2)} dx. \quad (7.11)$$

The distribution of the probability  $P_{\chi^2}(N_{\text{DoF}})$  should be uniform between 0 and 1 if correct and Gaussian distributed errors are used.

In the semileptonic channel,  $W^+W^- \rightarrow q\bar{q}\ell\bar{\nu}$ , the constrained kinematic fit uses the measured momenta of the two jets and the lepton and their covariance matrix as input parameters.

In the case of  $W^+W^- \rightarrow q\bar{q}e\bar{\nu}$  and  $W^+W^- \rightarrow q\bar{q}\mu\bar{\nu}$  events, the input variables are the measured jet momenta and directions and the lepton momentum and

direction. In the case of  $W^+W^- \rightarrow q\bar{q}\tau\bar{\nu}$  events, the measured input values are the jet momenta and directions and the lepton direction<sup>12</sup>. The absolute value of the lepton momentum is unknown due to the emission of an unobserved neutrino from the decay of the—also unobserved—primary tau lepton.

Intermittent energy calculations in the fit, as e.g. for the energy constraint, use the masses returned by the DURHAM jet clustering algorithm [43] for the jets, the lepton masses are taken from [49].

The kinematic fit allows the complete reconstruction of  $W^+W^- \rightarrow q\bar{q}\ell\bar{\nu}$  events if energy and momentum conservation are applied,

$$\sum_{i=1}^4 (E_i, \mathbf{p}_i) = (\sqrt{s}, \mathbf{0}), \quad (7.12)$$

which gives 4 equations of constraints. Here,  $E_i$  denotes the energy of the  $i$ -th particle (jet, lepton or neutrino),  $\mathbf{p}_i$  its 3-momentum and  $\sqrt{s}$  the center-of-mass energy.

It has been shown [50] that the event mass resolution can be further improved by using an equal-mass constraint, that is by imposing the constraint that the two bosons of the W-pair have the same mass,

$$m_{W^+} = m_{W^-}, \quad (7.13)$$

although this constraint is less well motivated by physics—the W boson has a finite width of approximately 2 GeV.

The exact form of the additional terms for the equations of constraint in equation (7.9) depends on their implementation, two alternative methods are described below.

If energy and momentum conservation and an equal mass constraint are applied, the number of degrees of freedom for a kinematic fit—as calculated from equation (7.10)—for  $W^+W^- \rightarrow q\bar{q}e\bar{\nu}$  and  $W^+W^- \rightarrow q\bar{q}\mu\bar{\nu}$  events is 2, since we have 9 measured quantities (the jet and lepton 3-momenta), 12 fit parameters (the jet, lepton, and neutrino 3-momenta), and 5 equations of constraint; for  $W^+W^- \rightarrow q\bar{q}\tau\bar{\nu}$  events the number of degrees of freedom is reduced to 1, since only 8 quantities (the two jet 3-momenta and the direction of the tau lepton) are now measured.

After the minimization of the  $\chi^2$ -function the invariant masses of the two W bosons in the event can be calculated from the best momentum estimates of the two jets, the lepton and the neutrino. The momentum of the unmeasured neutrino is calculated from the equations of constraint.

The fit probability, as defined by equation (7.11), can be used to reject badly reconstructed events and background processes from the data sample.

<sup>12</sup>Due to the high energy of the tau lepton in  $W \rightarrow \tau\nu_\tau$  decays, the decay products are emitted preferentially in its direction of flight.  $W^+W^- \rightarrow q\bar{q}\tau\bar{\nu}$  events in which the lepton candidate was misidentified or for which there is no correspondence between the direction of the primary tau lepton and the associated decay products are treated as an additional background source in the  $W^+W^- \rightarrow q\bar{q}\tau\bar{\nu}$  channel, see chapter 8.2.3.

### Constrained Kinematic Fit with Lagrange Multipliers

The OPAL WW analysis framework [37] provides a kinematic fit in which the equations of constraint are implemented by Lagrange multipliers [51]. In this case the  $\chi^2$ -function, equation (7.9), takes the form

$$\chi^2 = \sum_{i=1}^{N_{\text{meas}}} \sum_{j=1}^{N_{\text{meas}}} (\mathbf{p} - \hat{\mathbf{p}})_i G(\mathbf{p})_{ij} (\mathbf{p} - \hat{\mathbf{p}})_j + 2 \sum_{i=1}^{N_C} \lambda_i f_i(\hat{\mathbf{p}}), \quad (7.14)$$

where  $G$  denotes the inverse covariance matrix of the measured momenta  $\mathbf{p}$ ,  $N_{\text{meas}}$  is the number of measured momentum components and  $N_C$  is the number of constraints;  $\lambda_i$  is the Lagrange multiplier of the  $i$ -th equation of constraint

$$f_i(\hat{\mathbf{p}}) = 0. \quad (7.15)$$

The minimization is carried out with respect to the estimated momentum components and the Lagrangian multipliers which leads to the following set of conditions:

$$\frac{\partial \chi^2}{\partial \hat{p}_i} = 2 \sum_{j=1}^{N_{\text{meas}}} G(\hat{\mathbf{p}})_{ij} (\hat{p}_j - \hat{p}_i) + 2 \sum_{i=1}^{N_C} \lambda_i \frac{\partial f_i(\hat{\mathbf{p}})}{\partial \hat{p}_i} = 0 \quad (7.16)$$

$$\frac{\partial \chi^2}{\partial \lambda_i} = f_i(\hat{\mathbf{p}}) = 0. \quad (7.17)$$

The solution of these equations determine the best estimates of the momenta, as well as the Lagrange multipliers for the equations of constraint. The best estimates satisfy the equations of constraint exactly, which allows the calculation of the unmeasured momentum components of the neutrino and in the case of  $W^+W^- \rightarrow q\bar{q}\tau\bar{\nu}$  events of the absolute value of tau momentum.

In the WW analysis framework the kinematic fit is implemented as an iterative procedure since the equations of constraint are non-linear. In each iteration, a linear approximation based on the derivatives of the  $\chi^2$ -function with respect to the individual parameters is used to improve the estimates.

The standard kinematic fit of the WW analysis framework provides an important cross-check for the kinematic fit routine used with the *Convolution method*, see below and chapter 8.2, and was also used in initial studies.

### Constrained Kinematic Fit with Penalty Functions

The standard kinematic fit of the OPAL WW analysis framework described above proved to be too unstable to be used for the W mass measurement with *Convolution method* (see chapter 8.2). While the fit works reliably if the W mass is unconstrained, it often fails if the W mass is required to have a specific value, as it is needed in the computation of the event probability density used in the *Convolution method*. The instability is inherent in the computational implementation

of the iterative method and the use of the linearized approximations and cannot be avoided on a general bases<sup>13</sup>.

An alternative kinematic fit method for  $W^+W^- \rightarrow q\bar{q}\ell\bar{\nu}$  events was developed, based on the minimization of a  $\chi^2$ -function with the MINUIT program [52]. In this  $\chi^2$ -function the energy and equal mass constraints are implemented as penalty functions instead of using Lagrange multipliers. The momentum conservation is used directly to calculate the neutrino momentum in each step of the minimization.

Mathematically the  $\chi^2$ -function is given by

$$\chi^2 = \sum_{i=1}^{N_{\text{meas}}} \sum_{j=1}^{N_{\text{meas}}} (\mathbf{p} - \hat{\mathbf{p}})_i G(\mathbf{p})_{ij} (\mathbf{p} - \hat{\mathbf{p}})_j + \frac{(\sum_i E_i - \sqrt{s})^2}{\delta_E^2} + \frac{(m_{12} - m_{34})^2}{\delta_m^2}, \quad (7.18)$$

where  $\hat{\mathbf{p}}_i$  denotes the estimate of the kinematic variable  $i$ ,  $\mathbf{p}_i$  its measured value, and  $G$  the inverse covariance matrix of the measured variables.  $E_i$  is the energy of the  $i$ -th jet/lepton,

$$E_i = \sqrt{m_i^2 + \hat{\mathbf{p}}_i^2}, \quad (7.19)$$

with either  $m_i$  the measured jet mass or the mass corresponding to the identified lepton; neutrinos are regarded as massless.  $\sqrt{s}$  denotes the center-of-mass energy. The invariant masses of the two  $W$ -systems (jet-jet and lepton-neutrino),  $m_{12}$  and  $m_{34}$ , are calculated as

$$m_{ij} = \sqrt{(E_i + E_j)^2 - (\hat{\mathbf{p}}_i + \hat{\mathbf{p}}_j)^2}, \quad (7.20)$$

where the indices  $i$  and  $j$  denote the jets or leptons. The momentum conservation is used to calculate the missing neutrino momentum,

$$\hat{\mathbf{p}}_\nu = - \sum_{i=1}^2 \hat{\mathbf{p}}_{\text{jet},i} - \hat{\mathbf{p}}_{\text{lepton}}, \quad (7.21)$$

and  $\delta_E$  and  $\delta_m$  denote the penalty factors for the energy and mass constraints.

The penalty factors are chosen such that the minimization of the  $\chi^2$ -function yields the same mass value as the standard kinematic fit as implemented in the WW analysis framework and that a flat probability distribution is obtained. Figure 7.7 shows the distribution of the fit probabilities for all three classes of semileptonic events at a center-of-mass energy of  $\sqrt{s} = 189$  GeV. The histogram depicts the Monte Carlo expectation, the points with error bars denote the OPAL data at  $\sqrt{s} = 189$  GeV. Monte Carlo and data are in good agreement with each other.

<sup>13</sup>A complete independent implementation of the kinematic fit based on Lagrange multipliers and linear approximation suffered the same problems.

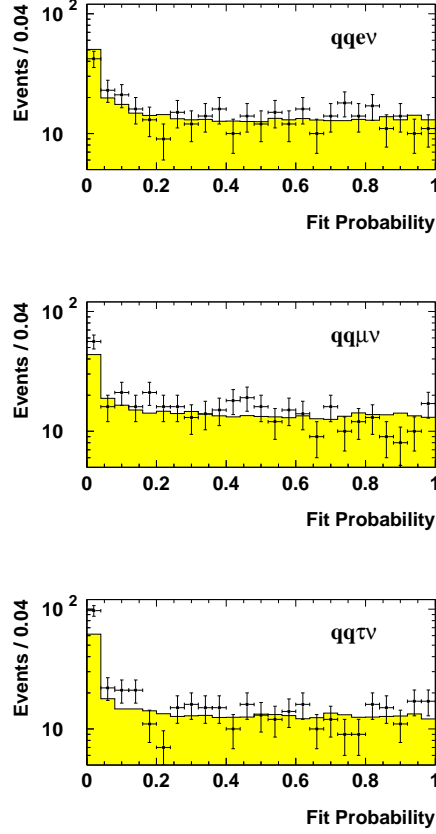


**Figure 7.7:** Distribution of the fit probabilities for Monte Carlo (histogram) and OPAL data (points with error bars) at a center-of-mass energy of  $\sqrt{s} = 189$  GeV.

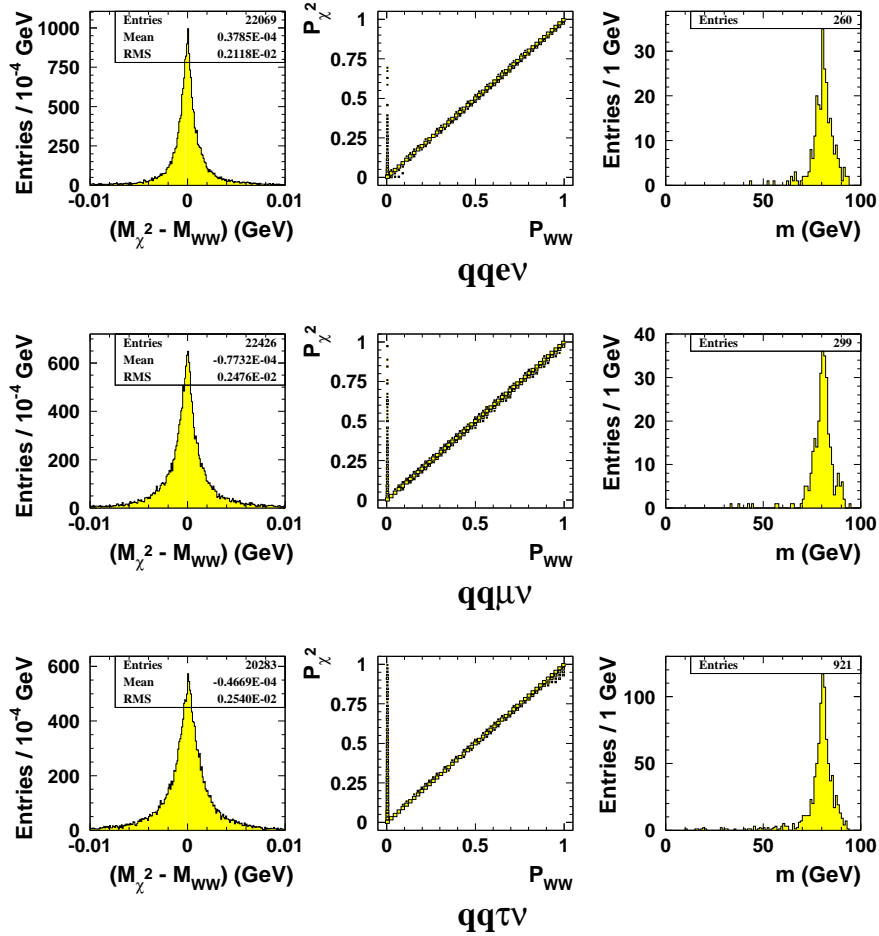
### Comparison of the Constrained Kinematic Fits

Figure 7.8 shows a comparison of the results of the standard kinematic fit as implemented in the OPAL WW analysis framework [37] and the  $\chi^2$ -minimization using equation (7.18) for all three semileptonic event classes,  $W^+W^- \rightarrow q\bar{q}e\bar{\nu}$ ,  $W^+W^- \rightarrow q\bar{q}\mu\bar{\nu}$ , and  $W^+W^- \rightarrow q\bar{q}\tau\bar{\nu}$ . This study uses Monte Carlo events generated at a center-of-mass energy of  $\sqrt{s} = 189$  GeV. The probability distributions were calculated using equation (7.11).

The deviation of the fitted mass  $M_W$  and the fit probabilities of the  $\chi^2$ -minimization from the values obtained with the standard kinematic fit is negligible: The mean difference for the event mass is less than 0.05 MeV, the RMS less than 3 MeV. For the fit probability the mean difference is less than  $1 \times 10^{-4}$  and the RMS less than  $2 \times 10^{-4}$ .

The  $\chi^2$ -minimization is more stable, resulting in a small overall increase in the

selected number of events compared to the standard kinematic fit. This stability becomes more important when the additional constraint of a fixed event mass is used in the computation of the  $\chi^2$ -relations, where a kinematic fit with Lagrange multipliers often fails. The number of selected events increases by 1.2%, 1.3% and 4.5% for the  $W^+W^- \rightarrow q\bar{q}e\bar{\nu}$ ,  $W^+W^- \rightarrow q\bar{q}\mu\bar{\nu}$  and  $W^+W^- \rightarrow q\bar{q}\tau\bar{\nu}$  channel, respectively.



**Figure 7.8:** Comparison of the results of the standard kinematic fit as implemented in the WW analysis framework [37] and the  $\chi^2$ -minimization used in the *Convolution method*. Plotted are the results of a Monte Carlo study at  $\sqrt{s} = 189$  GeV using four-fermion  $W^+W^-$  final states. Left: Difference between the event W mass  $M_{\chi^2}$  obtained from the  $\chi^2$ -minimization and the event W mass  $M_{WW}$  from the standard kinematic fit. Center: Fit probability  $P_{\chi^2}$  of the  $\chi^2$ -minimization versus fit probability  $P_{WW}$  of the standard kinematic fit. A logarithmic dependence of the box sizes on the number of entries has been chosen to enhance the small deviations. Additional events which pass the  $\chi^2$ -minimization selection but fail the probability cut for the standard kinematic fit are situated in the band at  $P_{WW} = 0$ . Right: Mass distribution of the additional events which are selected by the *Convolution method*, but failed the probability cut on the standard kinematic fit.





## Chapter 8

# Measurement of the Mass of the W Boson using a Convolution Method

In this chapter, a new way to extract the mass of the W boson from the data, the *Convolution method* [53], will be discussed in detail. The method is complementary to the two alternative approaches, the *Breit-Wigner fit* and the *Reweighting method*, also used within the OPAL collaboration to measure the W mass.

We start the presentation with a short introduction which recapitulates the properties and advantages of the semileptonic decay of W boson pairs,  $W^+W^- \rightarrow q\bar{q}\ell\bar{\nu}$ , for the W mass measurement and provides an overview of the method and a motivation for the use of a *Convolution method* in favor of a standard unbinned maximum likelihood fit.

We then describe the technical details of the *Convolution method*, the kinematic reconstruction routine, the calculation of the event probability densities, and the construction of the physics function which is used as a best estimate of the expected mass distribution and forms the basis of the likelihood.

The calibration of the *Convolution method* to correct residual biases in the W mass determination is discussed, estimates of the statistical error for a data-sized sample are presented and the systematic uncertainty of the W mass measurement with the *Convolution method* is determined.

### 8.1 Overview

The *Convolution method* tries to use all the available information of each single event in an unbinned maximum likelihood fit of a theoretical distribution to the data sample. For each event, a probability density which represents the probability that a W boson with a particular reconstructed mass has generated the event, is convolved with a physics function to yield the likelihood; the physics function represents the probability that for a given value of the W mass  $M_W$  and width  $\Gamma_W$

a pair of W bosons with a particular reconstructed mean mass is produced in the  $e^+e^-$  collision. The *Convolution method* was developed to improve the precision of the W mass measurement in the semileptonic decay channel,  $W^+W^- \rightarrow q\bar{q}\ell\bar{\nu}$ .

The semileptonic decay of a W boson pair is well suited for the determination of the mass of the W boson as it has high statistics (44% of all W boson pair decays, comparable to the  $W^+W^- \rightarrow q\bar{q}q\bar{q}$  channel), a clear event signature, only low background contributions from other processes, and a complete kinematic event reconstruction is possible. It does not suffer from systematic uncertainties on the reconstructed W boson mass from final state interactions like *Bose-Einstein Correlations* or *Color Reconnection* and has no combinatorial background as the two observed jets belong to same W boson.

The main disadvantage of the  $W^+W^- \rightarrow q\bar{q}\ell\bar{\nu}$  events is the presence of one unobserved primary neutrino. A kinematic fit, which improves the mass resolution, is therefore less constraint as in the case of  $W^+W^- \rightarrow q\bar{q}q\bar{q}$  decays where all primary partons lead to observable hadronic jets; this results in larger errors on the reconstructed W mass in each individual event in semileptonic decays of W boson pairs.

A standard method to extract the mass of the W boson from a data sample is to use an unbinned maximum likelihood fit, in which the likelihood for each event is given by the value of a probability density function, also called a physics function,  $f(m_i; M_W, \Gamma_W, \sqrt{s})$  evaluated at the reconstructed event mass  $m_i$ . The physics function  $f(m_i; M_W, \Gamma_W, \sqrt{s})$  should be the best conceivable estimate of the expected distribution of the reconstructed event masses, and depends on the parameters of the W boson—its mass  $M_W$  and its width  $\Gamma_W$ —and the center-of-mass energy  $\sqrt{s}$ . The total likelihood which is maximized to obtain  $M_W$  is given by the product of the event likelihoods, as the individual events represent independent measurements of the properties of the W boson.

The simple method of an unbinned maximum likelihood fit is only applicable if the precision with which the individual event masses  $m_i$  are reconstructed are comparable to each other or the errors are smaller than the natural width of the W boson ( $\Gamma_W \approx 2$  GeV), otherwise badly measured events have too large a weight in the fit. These two requirements are fulfilled for hadronic decays, but not in the case of semileptonic decays. Figure 8.1 compares the event error distributions for  $W^+W^- \rightarrow q\bar{q}q\bar{q}$  (left) and  $W^+W^- \rightarrow q\bar{q}\ell\bar{\nu}$  events (right) as obtained from a kinematic fit with energy and momentum conservation and an equal mass constraint; the histograms show the Monte Carlo expectations, the points with error bars denote the OPAL data at a center-of-mass energy of  $\sqrt{s} = 189$  GeV. Monte Carlo and data are in good agreement.

While the errors for  $W^+W^- \rightarrow q\bar{q}q\bar{q}$  events are small compared to the width of the W boson and their distribution is sharply peaked, the errors for  $W^+W^- \rightarrow q\bar{q}\ell\bar{\nu}$  events follow a broad distribution which exceeds by far the natural W width. Therefore a convolution method, which includes the individual measurement errors and weights the events correctly, should improve the precision of the measurement of the W boson mass in the semileptonic channel.

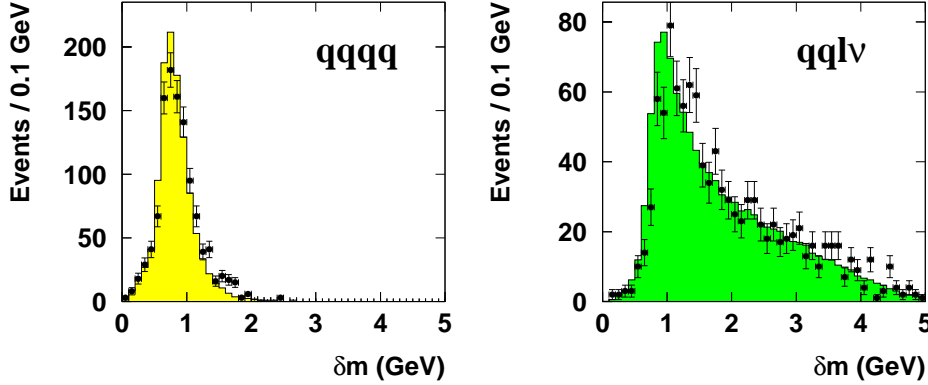


**Figure 8.1:** Distribution of the event mass errors for  $W^+W^- \rightarrow q\bar{q}q\bar{q}$  (left) and  $W^+W^- \rightarrow q\bar{q}\ell\bar{\nu}$  events (right) at a center-of-mass energy of  $\sqrt{s} = 189$  GeV. The histogram shows the Monte Carlo expectation, the points with error bars denote the OPAL data.

The analysis follows the approach outlined in chapter 6.2. In each event the non-leptonic part is forced into two jets using the DURHAM algorithm [43] after the best lepton candidate has been identified. The jet and lepton momenta are then improved by a kinematical reconstruction of the event by applying energy and momentum conservation and an equal mass constraint.

The kinematical reconstruction routine is also used to obtain the, in general asymmetric, probability density of the mean event W mass (see section 8.2.1). This probability density is then convolved with the physics function to yield the event likelihood, thus taking into account the precision of the individual W mass measurements.

The physics function is based on relativistic Breit-Wigner functions which contain a phase space factor to describe the cut-off due to the maximum available center-of-mass energy. One difficulty in the choice of the physics functions comes from the fact that *Initial State Radiation*—the emission of photons just before the  $e^+e^-$  collision—can alter the available center-of-mass energy from event to event. The ISR photons remain almost always undetected as they are emitted in the direction of the beam pipe from the highly relativistic incoming electrons and positrons; thus a proper inclusion of ISR in the energy conservation constraint in the kinematic fit is not feasible. This problem is solved by the inclusion of ISR on a statistical level in the physics function to compensate its effects on the reconstructed event W masses (see section 8.2.3).

The physics function also contains parts to describe the reconstructed mass distributions of the important background processes.

An unbinned maximum likelihood fit then yields the value of the mass of the W boson which describes the measured data best.

## 8.2 The Convolution Method

### 8.2.1 Calculation of the Event Probability Density

After an event has been selected as a  $W^+W^- \rightarrow q\bar{q}\ell\bar{\nu}$  decay, the most probable lepton candidate has been identified and the non-leptonic part is forced into two jets using the DURHAM jetfinder, compare chapter 7.2. The jet energies are corrected for double counting in the calorimeters by applying the MT algorithm [45–47]. See chapter 7 for further information and section 8.2.4 for additional applied cuts to improve the data quality.

The energy corrected lepton and jet momenta are then used as input for a kinematic fit routine which is used to obtain the event probability density.

The event probability density  $P(m)$  assigns each W mass value  $m$  a probability that a W boson with that reconstructed mass generated this particular event. It is closely related to the usually quoted measured mean W mass  $m_i$  in the event, and its error. The mean W mass  $m_i$  is the most probable value of  $m$ , while the in general asymmetric error interval  $[m_i - \delta_i^-, m_i + \delta_i^+]$  can be calculated from the 68% confidence level  $CL_{68\%}$  [54] as the shortest interval which satisfies

$$CL_{68\%} = \int_{m_i - \delta_i^-}^{m_i + \delta_i^+} P(m) dm. \quad (8.1)$$

The kinematic fit applies constraints for energy and momentum conservation in order to obtain better estimates for the measured quantities. In addition to these physically motivated constraints—they are given by the fact that electrons and positrons have no substructure and that the two colliding beams have equal energy and opposite directions at the interaction point—an equal mass constraint ( $m_{W^+} = m_{W^-}$ ) is used to further improve the mass resolution [50]. The equal mass constraint also serves to reduce a 2-dimensional problem to one dimension, thus greatly simplifying and speeding up the necessary calculations. Since both the event probability and the physics function, which have to be convolved to yield the event likelihood, cannot be expressed in analytic forms, but have to be calculated numerically, this saves approximately a factor of 1000 in the analysis time. The typical time to process one event is 0.2 seconds on a Intel PIII™ 600 MHz CPU based system; the analysis uses roughly 750000 Monte Carlo events at each value of the center-of-mass energy for systematic studies.

The calculation of the event probability density is based on a kinematic fit using a  $\chi^2$ -function with penalty functions to implement the equations of constraint, see chapter 7.3.2.

#### Fit Input Variables and their Parameterization

The input variables of the kinematic fit are the jet and lepton 3-momenta and their covariance matrix. In the case of  $W^+W^- \rightarrow q\bar{q}\tau\bar{\nu}$  events only the direction of flight of the tau lepton is used, as reconstructed from its decay products.

Particle type	Parameterization		
	Momentum	Polar angle	Azimuthal angle
Jet	$\log p$	$\theta$	$\phi$
Electron	$p$	$\cot \theta$	$\phi$
Muon	$1/p_T$	$\cot \theta$	$\phi$
Tau lepton	$(p)$	$\theta$	$\phi$

**Table 8.1:** Parameterization of the input of the kinematic fit routine for the different particle types. The parameterizations are chosen to yield approximative Gaussian errors.  $p$  denotes the total momentum,  $p_T$  the transverse momentum in the x-y plane. The momentum of the tau lepton is not used in the kinematic fit.

The input variables for the kinematic fit routine are parameterized to yield approximative Gaussian errors and negligible correlations; the former is necessary to obtain a valid  $\chi^2$ -function<sup>1</sup>, while the latter simplifies the calculations as the covariance matrix is then diagonal and thus easily inverted.

Table 8.1 lists the parameterizations used for the different particle types. The parameterization for the leptons is a direct result of the way their momenta are measured: the electron momentum is derived from its energy measurement in the electromagnetic calorimeter ( $E \approx p$ ) while the muon momentum is determined from the curvature of its track in the central drift chambers ( $\propto 1/p_T$ ).

### The Kinematic Fit and the Underlying $\chi^2$ -Function

The usual way to exploit a kinematic fit is to use it to determine the best possible estimates to the measured and unmeasured parameters by minimizing a  $\chi^2$ -function of the measured momenta subject to some constraints. The estimated momenta then yield the W mass(es) in the event and the  $\chi^2$  value can be used as a measure of the *goodness-of-fit* and can be converted to a fit probability, compare chapter 7.3.2.

The *Convolution method* takes this concept one step further, by inverting the above reasoning: For a given mass  $m$  of the W boson we wish to obtain the best estimates of the parameter set  $\hat{\mathbf{p}}$ . The value  $\chi^2(m)$  that corresponds to these estimates under the fixed mass constraint is then converted to a probability. This probability describes the likelihood that a pair of W boson with a particular reconstructed mean mass  $m$  has generated the event<sup>2</sup>.

The  $\chi^2$ -function used to obtain the event probability density is based on equation (7.18). To achieve our goal of minimizing the  $\chi^2$  at a fixed mass  $m$  of the W

<sup>1</sup>The concept of the fit probability as defined by equation (7.11) is based on the assumption of Gaussian distributed errors of the parameters.

<sup>2</sup>To avoid the cumbersome construct *mean mass of a pair of W bosons* throughout the text, most of the time the simple singular form *mass of a W boson* will be used. As the kinematic fit used in the analysis *always* applies an equal-mass constraint it should be clear that only the mean mass of the two W bosons involved in the event can be calculated and all reasonings concern this mean mass.

boson, the penalty term for the equal mass constraint in equation (7.18),

$$\frac{(m_{12} - m_{34})^2}{\delta_m^2},$$

is replaced by

$$\frac{(m_{12} - m)^2}{\delta_m^2} + \frac{(m_{34} - m)^2}{\delta_m^2}. \quad (8.2)$$

The sought value  $\chi^2(m)$  is then given by the minimum value of the  $\chi^2$ -function with respect to the best estimates  $\hat{\mathbf{p}}$ ,

$$\begin{aligned} \chi^2(m) = \min_{\hat{\mathbf{p}}} & \left( \sum_{i,j} (\mathbf{p} - \hat{\mathbf{p}})_i G_{ij} (\mathbf{p} - \hat{\mathbf{p}})_j \right. \\ & + \frac{(\sum_i E_i - \sqrt{s})^2}{\delta_E^2} \\ & \left. + \frac{(m_{12} - m)^2}{\delta_m^2} + \frac{(m_{34} - m)^2}{\delta_m^2} \right). \end{aligned} \quad (8.3)$$

In these equations  $m_{12}$  denotes the invariant mass of the dijet system,  $m_{34}$  the mass of the lepton-antineutrino system,  $m$  the value of the W mass at which the function is evaluated,  $\mathbf{p}$  the set of measured parameters,  $G$  their inverse covariance matrix,  $\hat{\mathbf{p}}$  the current estimates to the measured parameters,  $E_i$  the energy of the  $i$ -th jet or lepton (compare equation (7.19)) and  $\delta_E$  and  $\delta_m$  the penalty factors for the energy and equal mass constraints. The second and third line in equation (8.3) are the energy and mass constraints, respectively.

The absolute value of the  $\chi^2$ -function at the minimum,  $\chi_i^2(m_i)$  for each event, converted to a fit-probability, is used in the data quality cuts to reject events which do not match the  $W^+W^- \rightarrow q\bar{q}\ell\bar{\nu}$  hypothesis well, see section 8.2.4.

It should be noted that the  $\chi^2$ -function does *not* take the effect of *Initial State Radiation* (ISR) into account, since the *possible* inclusion of the—often unobserved—photon is rather difficult. Instead, the energy is always constrained to the nominal value of  $\sqrt{s}$  and the inclusion of ISR is deferred to the physics function, see section 8.2.3.

### The Event Probability Density

The event probability density  $P_i(m)$  is calculated by transforming the values of the  $\chi^2(m)$ -function by

$$P_i(m) = \frac{1}{N} \exp \left( -\frac{\chi_i^2(m) - \chi_i^2(m_i)}{2} \right), \quad (8.4)$$

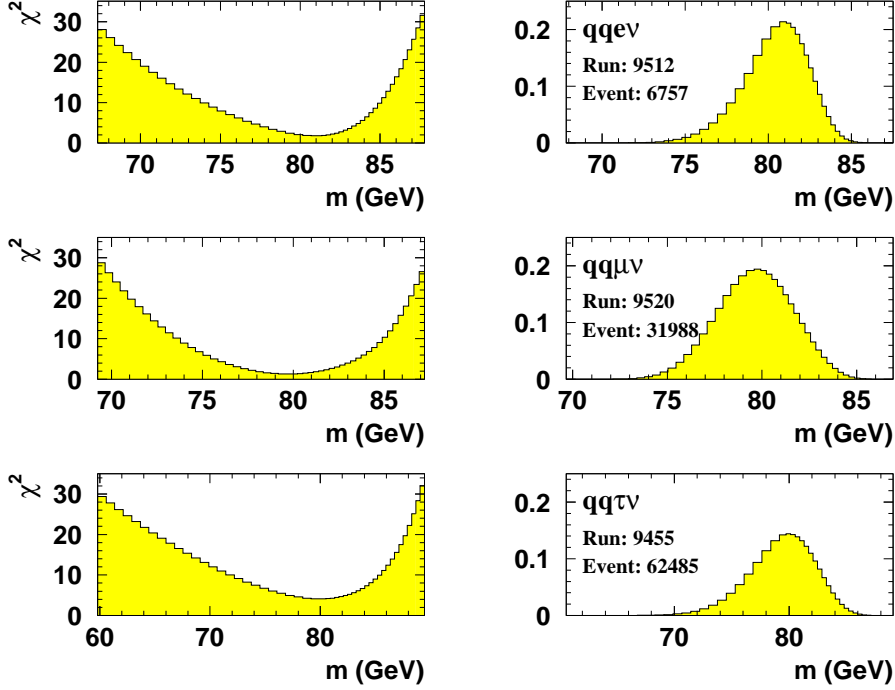


**Figure 8.2:** Examples of  $\chi_i^2(m)$  (left) and corresponding event probability densities  $P_i(m)$  (right) for data events at  $\sqrt{s} = 189$  GeV. The symmetric form for the  $W^+W^- \rightarrow q\bar{q}\mu\bar{\nu}$  event is not representative. Please note the different scales on the abscissas.

where  $m_i$  denotes the value of  $m$  at the absolute minimum of the  $\chi^2$ -function.  $N$  is the normalization factor, given by

$$N = \int_{-\infty}^{\infty} \exp\left(-\frac{\chi_i^2(m) - \chi_i^2(m_i)}{2}\right) dm. \quad (8.5)$$

For the calculation of the event probability density only the change of the  $\chi^2$  with respect to the value  $\chi_i^2(m_i)$  at the minimum is important. The masses at which a change of 1, 4, and 9 occurs in the  $\chi^2$  mark the ranges of the 68%, 96%, and 99.5% confidence level intervals. The conversion in equation (8.4) ensures that we obtain a Gaussian distribution for a parabolic shape of the  $\chi^2(m)$ -function. Figure 8.2 shows examples of the  $\chi^2(m)$ -relations and the corresponding probability densities  $P_i(m)$  for some data events at  $\sqrt{s} = 189$  GeV.

The event probability density usually has an asymmetric shape. It is more probable that a W boson with a lower mass produces a given event than a W boson with a high mass. To explain this asymmetry let us consider the situation after a kinematic fit with energy and momentum conservation and an equal mass constraint

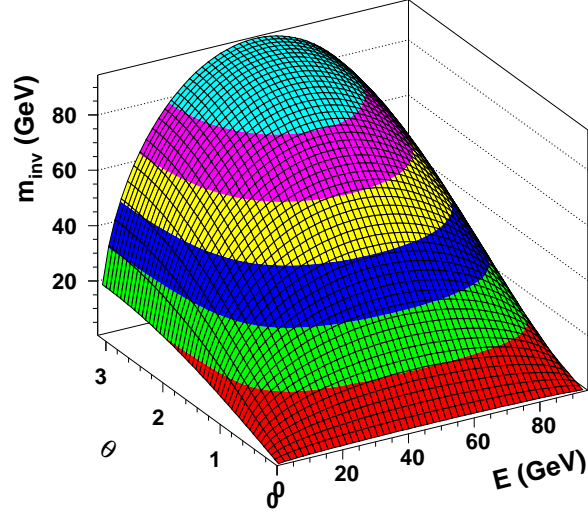


**Figure 8.3:** Invariant mass of the W boson as a function of the energy  $E$  of one decay product and the inter-particle angle  $\theta$  as calculated from equation (8.8) at  $\sqrt{s} = 189$  GeV.

has been applied. The energy conservation and the equal mass constraint together restrict the energy  $E_W$  of each W boson to

$$E_W = \sqrt{s}/2, \quad (8.6)$$

where  $\sqrt{s}$  denotes the center-of-mass energy. Using the energy constraint

$$E_1 + E_2 = \sqrt{s}/2 \quad (8.7)$$

to eliminate one of the energies, and neglecting the particle masses, the invariant mass of the dijet pair or the lepton-neutrino pair can be calculated as

$$m_{\text{inv}} = \sqrt{2E_1E_2(1 - \cos \theta)} = \sqrt{2E_1(\sqrt{s}/2 - E_1)(1 - \cos \theta)}; \quad (8.8)$$

here  $E_i$  denotes the energy of the  $i$ -th particle of the pair and  $\theta$  the angle between the them.

Figure 8.3 shows the invariant mass  $m_{\text{inv}}$  of the W boson as a function of the energy  $E$  of one of its decay products and the inter-particle angle  $\theta$ . For each fixed value of  $\theta$  the invariant mass has a maximum at  $E = \sqrt{s}/4$ , while for each fixed value of the energy  $E$  a maximum and minimum invariant mass exist for  $\theta = \pi$  and  $\theta = 0$ , respectively, as can be seen by setting the derivatives of equation (8.8) with respect to  $E$  and  $\theta$  to zero.



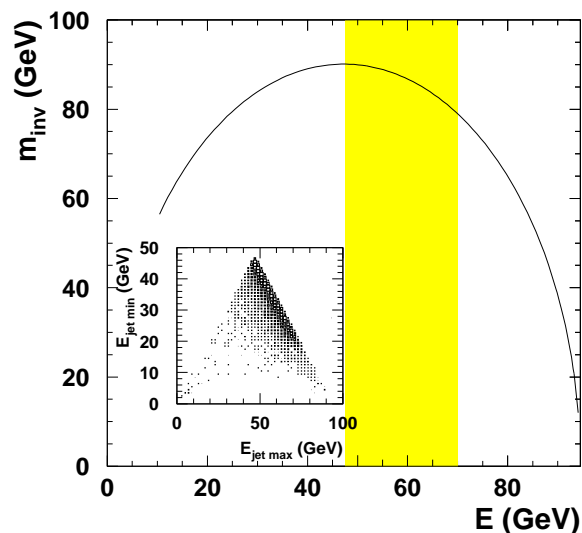


**Figure 8.4:** Invariant mass of the W boson as a function of the energy  $E$  of the higher energetic jet as calculated from equation (8.8) at  $\sqrt{s} = 189$  GeV ( $\theta = 140^\circ$ ). The inset shows the distribution of the lower energetic jet versus the energy of the higher energetic jet. The yellow (light grey) area corresponds to the most likely values of the energy of the higher energetic jet.

Figure 8.4 depicts the invariant mass as a function of the energy  $E$  for a fixed angle ( $140^\circ$ —which is the expected angle between the decay products of a W boson of  $M_W = 80.33$  GeV at  $\sqrt{s} = 189$  GeV) between the particles, the small inset shows the distribution of the two jet energies after the kinematic fit has been applied, the anti-correlation caused by the energy and equal mass constraint is clearly visible. Almost always the energy of the higher energetic jet lies in the range of 45 to 70 GeV, which is in the vicinity of the maximum of the invariant mass, depicted as the yellow (light grey) band in the plot.

Now we wish to add the additional constraint of a fixed invariant mass in the calculation. The direction of the jets and the lepton are measured with very high precision compared to their energy. Thus the kinematic fit will not modify the directions very much, as the  $\chi^2$  value would increase rapidly with any deviation from the measured values. The only way to satisfy the fixed mass constraint is to alter the energies. As can be seen in figure 8.4 the absolute value of the derivative increases with the jet energy as we go further from the maximum, as the function is nonlinear. To achieve a change of the invariant mass towards higher values a larger change in the jet energies is required than for a change towards lower mass values. The energy change results in an increased  $\chi^2$  value, which corresponds to

a lower value of the event probability density at that particular mass. The event probability density therefore decreases more rapidly towards higher masses than towards lower ones.

The interpretation of  $P_i(m)$  as a probability density is only valid if the normalization factor  $N$  cancels out the dependence of  $\chi^2$  on the penalty factors for the energy and equal mass constraint. This point is discussed further in appendix B.

### 8.2.2 ISR and Effects on the Event Mass Reconstruction

The  $\chi^2$ -function defined in equation (7.9) assumes that each event takes place at the nominal center-of-mass energy  $\sqrt{s}$ . It does not take into account the effects of *Initial State Radiation* (ISR), the emission of photons by the electrons and positrons just before the collision. The ISR emission leads to a lower center-of-mass energy  $\sqrt{s'}$  which is actually available for the production of the W boson pair and thus causes a shift in the reconstructed mass to higher values. This mass shift has to be taken into account in the measurement of the mass of the W boson.

The detection of *Initial State Radiation* photons in the detector is extremely difficult. In most cases the photon escapes unnoticed in the uninstrumented beam pipe, since it is emitted preferentially in the forward direction of the highly relativistic electrons and positrons. If all other decay products in the reaction are visible, the reduced center-of-mass energy  $\sqrt{s'}$  can be calculated as invariant mass of the total event, and could be taken into account. In semileptonic decays of W-pair,  $W^+W^- \rightarrow q\bar{q}\ell\bar{\nu}$ , this measurement of  $\sqrt{s'}$  is impossible, since the neutrino escapes unobserved and the remaining visible decay products do not satisfy the energy and momentum conservation. The inclusion of ISR in the W mass reconstruction in this channel can only be based on statistical arguments. Figure 8.5 shows the spectrum of ISR photons in selected  $e^+e^- \rightarrow W^+W^- \rightarrow q\bar{q}\ell\bar{\nu}$  events at a center-of-mass energy of  $\sqrt{s} = 189$  GeV, simulated with the KORALW program with an  $\mathcal{O}(\alpha^3)$  QED calculation. Only about 50% of the events have a negligible ISR energy, about 70% an ISR photon with less than 1 GeV and 85% an ISR photon with less than 5 GeV energy. The cut-off of the spectrum at 30 GeV is caused by the energy threshold for the W-pair production of two times the W mass.

It is rather involved and difficult to calculate the influence of the ISR photon and the reduced center-of-mass energy  $\sqrt{s'}$  on the result of the kinematic fit, due to the nonlinear equations of constraint for energy and momentum. But the mass shift can be estimated in a intuitive manner using the scaled hadronic mass<sup>3</sup> introduced in chapter 7.3.1.

We want to compare the value of the reconstructed W mass in the event if we knew the actual value of the center-of-mass energy,  $\sqrt{s'}$ , with the result that we obtain if we use the nominal value of the center-of-mass energy,  $\sqrt{s}$ .

Let  $E_1$  denote the measured energy of the first jet,  $E_2$  the energy of the second jet and  $\theta$  the angle between the two jets in the  $W^+W^- \rightarrow q\bar{q}\ell\bar{\nu}$  event.

<sup>3</sup>The scaled hadronic mass is highly correlated with the W mass obtained in a kinematic fit, as is shown in appendix C. Thus the reasoning provides a very good estimate of the actual mass shift.

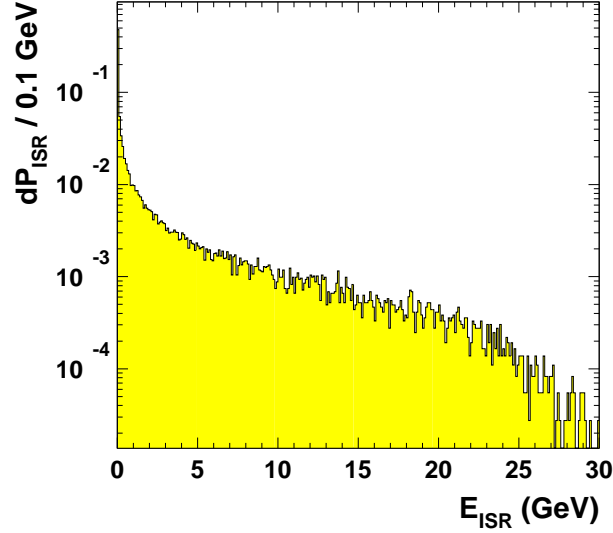


**Figure 8.5:** Spectrum of the ISR photons in selected  $e^+e^- \rightarrow W^+W^- \rightarrow q\bar{q}\ell\bar{\nu}$  events at a center-of-mass energy of  $\sqrt{s} = 189$  GeV as taken from a KORALW Monte Carlo sample with an  $\mathcal{O}(\alpha^3)$  treatment of the *Initial State Radiation*.

Using the actual center-of-mass energy  $\sqrt{s'}$ , we would obtain the best approximation to the true mean W mass in the event from equation (7.7) as

$$m'_{\text{scaled}} = \sqrt{2E_1E_2 \left( \frac{\sqrt{s'}/2}{E_1 + E_2} \right)^2 (1 - \cos \theta)}. \quad (8.9)$$

On the other hand, assuming that the nominal center-of-mass energy of  $\sqrt{s}$  is available in the event, the scaled hadronic mass  $m_{\text{scaled}}$  is given as

$$m_{\text{scaled}} = \sqrt{2E_1E_2 \left( \frac{\sqrt{s}/2}{E_1 + E_2} \right)^2 (1 - \cos \theta)}. \quad (8.10)$$

From these two equations, it follows that

$$m_{\text{scaled}} = m'_{\text{scaled}} \sqrt{\frac{s}{s'}}, \quad (8.11)$$

and further that the mass difference  $\Delta m_{\text{scaled}}$  between the reconstructed mass with the actual center-of-mass energy and the reconstructed mass under the assumption that the event took place at the nominal center-of-mass energy, is given by

$$\Delta m_{\text{scaled}} = m'_{\text{scaled}} - m_{\text{scaled}} = -(\sqrt{s} - \sqrt{s'}) \frac{m'_{\text{scaled}}}{\sqrt{s'}}. \quad (8.12)$$

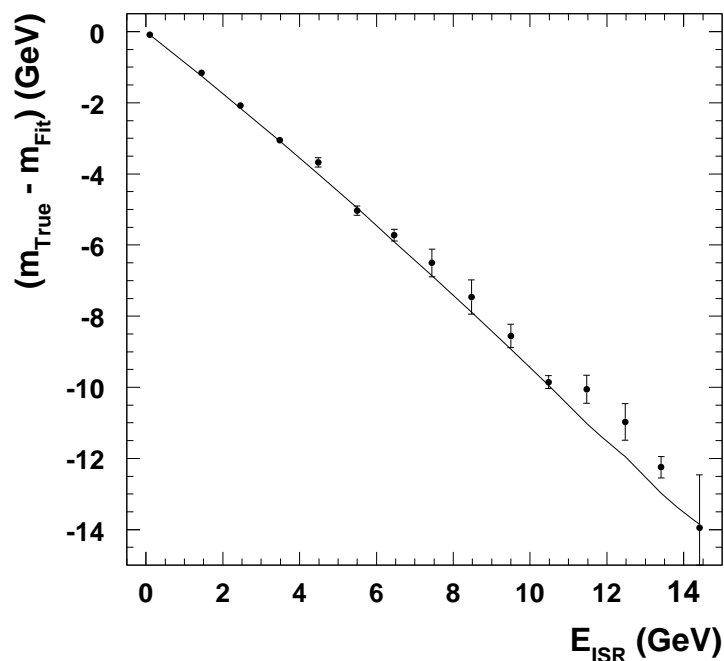


**Figure 8.6:** Mean shift between the true mean W mass in an event and the fitted mass as a function of the ISR photon energy  $E_{\text{ISR}}$ . The solid line connects the expectation of the mass shift as calculated from equation (8.12) for each bin, the points with error bars show the results of a Monte Carlo simulation at a center-of-mass energy of  $\sqrt{s} = 189$  GeV. The points are plotted at the mean ISR energy in each bin.

The mass shift is proportional to the difference of the nominal and actual center-of-mass energy, scaled by the ratio of the reconstructed mass at  $\sqrt{s'}$  to the actual center-of-mass energy. The reconstructed mass under the assumption that the event took place at the nominal center-of-mass energy is always higher than the mass that would be reconstructed if the actual center-of-mass energy had been known.

Figure 8.6 shows a comparison between the expectation of the mass shift (solid line) from equation (8.12) and the results of a Monte Carlo simulation (points with error bars). Instead of using the reconstructed mass at the actual center-of-mass energy  $\sqrt{s'}$  as an approximation of the true mean W boson mass, the Monte Carlo allows the direct use of the latter value. Equation (8.12) describes the mass shift rather well, and this result will be used in the calculation of the physics function to take into account the effects of the *Initial State Radiation* on the reconstructed W boson mass, see below.

### 8.2.3 The Physics Function

The physics function  $f(m; M_W, \Gamma_W, \sqrt{s})$  forms the basis of the likelihood calculation and depends on the parameters of the W boson, its mass  $M_W$ , its width  $\Gamma_W$  and the center-of-mass energy  $\sqrt{s}$ . The physics function is the weighted sum of a signal function  $f_{\text{signal}}(m; M_W, \Gamma_W, \sqrt{s})$ , which represents the expected mass distribution of true  $W^+W^-$  events, and background functions  $f_{\text{bg},i}(m)$  which describe the expected mass distributions of the important irreducible background processes.

The signal function is based on a relativistic Breit-Wigner function,

$$\mathcal{BW}(m; M_W, \Gamma_W) \propto \frac{m^2}{(m^2 - M_W^2)^2 + m^2\Gamma_W^2}. \quad (8.13)$$

The Breit-Wigner function  $\mathcal{BW}$  is extended by a phase space factor  $\mathcal{P}(m; \sqrt{s})$  which describes the cut-off of the production of W bosons at high mass values due to the maximum available center-of-mass energy in the experiment,

$$\mathcal{F}(m; M_W, \Gamma_W, \sqrt{s}) \propto \frac{m^2}{(m^2 - M_W^2)^2 + m^2\Gamma_W^2} \times \mathcal{P}(m; \sqrt{s}). \quad (8.14)$$

The phase space factor is given by the ratio of the momentum and the energy of the W boson,  $p/E$ ,

$$\mathcal{P}(m; \sqrt{s}) = \frac{p}{E} = \frac{\sqrt{s/4 - m^2}}{\sqrt{s}/2} \quad (8.15)$$

where  $\sqrt{s}$  denotes the center-of-mass energy and  $m$  the mass of the W boson; here an implicit equal mass constraint has been applied which leads to an energy of  $\sqrt{s}/2$  for each W boson.

To illustrate the good agreement between the function  $\mathcal{F}(m; M_W, \Gamma_W, \sqrt{s})$  and the generated mean W boson masses, figure 8.7 shows the results of a Monte Carlo study. The open histogram depicts the mean generated mass of the two W bosons in the Monte Carlo events, the solid line corresponds to the function  $\mathcal{F}(m; M_W, \Gamma_W, \sqrt{s})$ . To ensure the correct center-of-mass energy  $\sqrt{s}$ , only events with an ISR energy of less than 100 MeV were used.

The effects of the *Initial State Radiation* (ISR) on the mass reconstruction (compare chapter 8.2.2) can be included on a statistical level in the physics function.

The signal part of the physics function is constructed as a weighted superposition of Breit-Wigner functions at different center-of-mass energies  $\sqrt{s}$ . The Breit-Wigner function give the probability of the occurrence of a particular (mean) W mass in the event. The weight of each function is given by the probability that an event occurs at that particular center-of-mass energy and is determined from Monte Carlo.

The energy constraint to the nominal center-of-mass energy  $\sqrt{s}$  in the kinematic fit results in a shift of the reconstructed event W mass towards higher mass

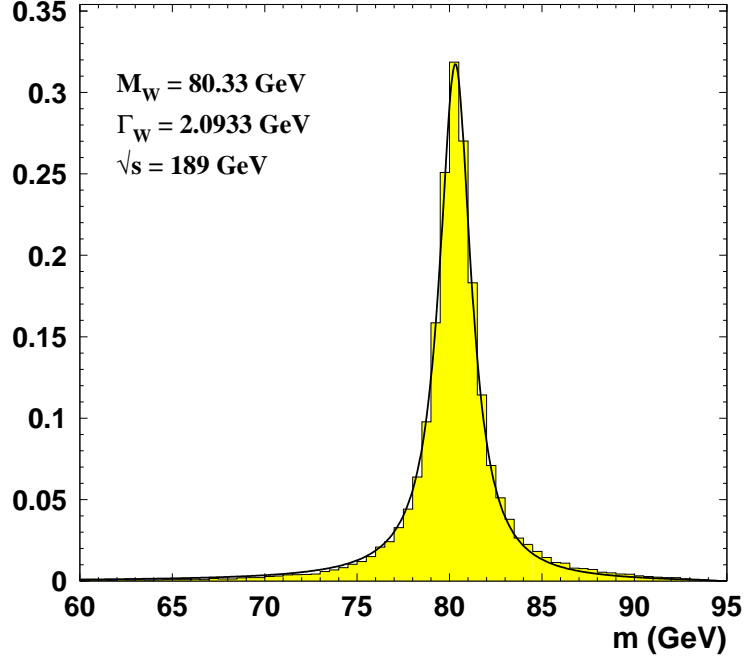


**Figure 8.7:** Comparison of the mean generated mass of the two W bosons in Monte Carlo events at a center-of-mass energy of  $\sqrt{s} = 189$  GeV with an ISR energy less than 100 MeV (histogram) with the function  $\mathcal{F}(m; M_W, \Gamma_W, \sqrt{s})$  as defined in equation (8.14) — a Breit-Wigner function which includes a phase space factor (solid line).

values. To take this into account, the individual Breit-Wigner functions have to be evaluated at the value of the corresponding true mass. Inverting equation (8.11), we obtain

$$m_{\text{true}} = m - \left(1 - \sqrt{\frac{s'}{s}}\right) m = m \sqrt{\frac{s'}{s}}. \quad (8.16)$$

where  $m_{\text{true}}$  denotes the true mass and  $m$  the measured mass. The probability that an event occurs with a (mean) W mass  $m_{\text{true}}$  is described by  $\mathcal{F}(m_{\text{true}}; M_W, \Gamma_W, \sqrt{s'})$ ; thus the probability that a (mean) W mass  $m$  is reconstructed for the event is given by  $\mathcal{F}(m\sqrt{s'/s}; M_W, \Gamma_W, \sqrt{s'})$ .

The signal function  $f_{\text{signal}}$  is given by

$$f_{\text{signal}}(m; M_W, \Gamma_W, \sqrt{s}) = \frac{1}{N} \int_0^s \mathcal{F}(m\sqrt{s'/s}; M_W, \Gamma_W, \sqrt{s'}) \times Q(s'; s) ds', \quad (8.17)$$

where  $N$  denotes the normalization factor of the function in the interval  $[0, s]$  and  $Q(s'; s)$  the probability that the event occurred at a center-of-mass energy of  $\sqrt{s'}$ .

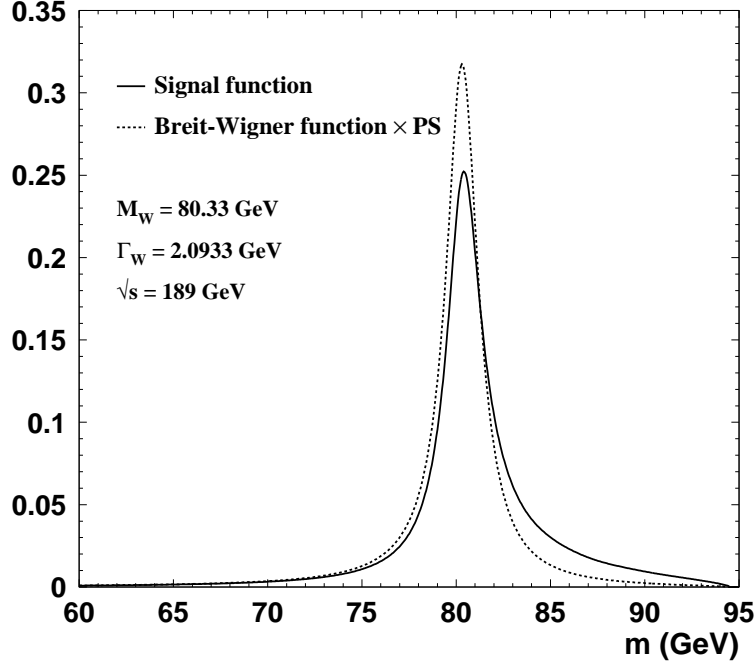


**Figure 8.8:** Comparison of the signal function  $f_{\text{signal}}(m; M_W, \Gamma_W, \sqrt{s})$  (solid line) with a relativistic Breit-Wigner function which includes a phase space factor (dashed line).

Figure 8.8 shows a comparison of the signal function  $f_{\text{signal}}$  with a Breit-Wigner function. The inclusion of ISR leads to an increased probability for high mass events in the signal function, as is expected from the reconstruction with a kinematic fit that assumes too high an energy in most cases.

The normalized physics function  $f$  is then given by

$$f(m; M_W, \Gamma_W, \sqrt{s}) = \left(1 - \sum_i \frac{\langle N_{\text{bg},i} \rangle}{N_{\text{exp}}}\right) f_{\text{signal}}(m; M_W, \Gamma_W, \sqrt{s}) + \sum_i \frac{\langle N_{\text{bg},i} \rangle}{N_{\text{exp}}} f_{\text{bg},i}(m), \quad (8.18)$$

where  $N_{\text{exp}}$  denotes the total number of expected events,  $\langle N_{\text{bg},i} \rangle$  the expected mean number of events for background  $i$ ,  $f_{\text{signal}}$  and  $f_{\text{bg},i}$  the normalized signal and the background functions.

The following background sources were included in the physics function:

- $e^-e^+ \rightarrow Z^0/\gamma \rightarrow q\bar{q}$
- $e^-e^+ \rightarrow 4f$  (e.g.  $e^+e^- \rightarrow Z^0Z^0$  or  $e^+e^- \rightarrow W\nu_e$  background)

- *Evil taus* (reconstructed tau-direction outside a cone of 15 degrees around true tau-direction)

For each background and each channel ( $W^+W^- \rightarrow q\bar{q}e\bar{\nu}$ ,  $W^+W^- \rightarrow q\bar{q}\mu\bar{\nu}$  and  $W^+W^- \rightarrow q\bar{q}\tau\bar{\nu}$ ) the shape and the mean number of events for a data-sized sample was obtained by analyzing a corresponding Monte Carlo sample using the same selections and cuts as for the data and scaling the number of accepted events to the data luminosity.

The background shapes are determined from the mass distributions obtained from a 2C-fit for the  $W^+W^- \rightarrow q\bar{q}e\bar{\nu}$  and  $W^+W^- \rightarrow q\bar{q}\mu\bar{\nu}$  channels and a 1C-fit for the  $W^+W^- \rightarrow q\bar{q}\tau\bar{\nu}$  channel; since the number of background events is very small, a large bin size (5–10 GeV) is used and an analytical representation is approximated by a linear interpolation between the bin contents. The use of the 2C/1C fit masses in conjunction with the large bin size—which is larger than the detector resolution—also approximately takes into account the influence of the *Initial State Radiation* on the background mass distributions, which are independent ( $Z^0/\gamma$ ,  $Z^0Z^0$  background) or only depend weakly on the W mass ( $W\nu_e$  background).

Table 8.2 lists the mean number of background events for a center-of-mass energy of  $\sqrt{s} = 183$  GeV, taken from Monte Carlo samples for  $e^+e^- \rightarrow Z^0/\gamma$ , for  $e^+e^- \rightarrow W\nu_e$ , for  $e^+e^- \rightarrow Z^0Z^0$ , and  $W^+W^-$  final states from the CC03 diagrams for the *Evil tau* background. Figure 8.9 shows the mass distributions for the  $e^+e^- \rightarrow Z^0/\gamma$ , the  $e^+e^- \rightarrow W\nu_e$ , the  $e^+e^- \rightarrow Z^0Z^0$  backgrounds, and the background shape for *Evil tau* events compared to  $W^+W^- \rightarrow q\bar{q}\tau\bar{\nu}$  events.

Table 8.3 lists the mean number of background events for a center-of-mass energy of  $\sqrt{s} = 189$  GeV, taken from Monte Carlo samples for  $e^+e^- \rightarrow Z^0/\gamma$ , four-fermion non- $W^+W^-$  final states<sup>4</sup>, and four-fermion  $W^+W^-$  final states<sup>5</sup> for the *Evil tau* background. Figure 8.10 shows the background shapes for the  $e^+e^- \rightarrow Z^0/\gamma$  and the four-fermion non- $W^+W^-$  and  $W^+W^-$  final states backgrounds and the background shape for *Evil tau* events compared to  $W^+W^- \rightarrow q\bar{q}\tau\bar{\nu}$  events.

#### 8.2.4 Data Quality Cuts

The events used in the measurement of the W boson mass have to pass the following data quality cuts:

- Fit probability  $P(m_{\min}) > 0.001$

<sup>4</sup>The four-fermion non- $W^+W^-$  final state Monte Carlo samples contain only events with final states that *cannot* be produced by W-pairs.

<sup>5</sup>The four-fermion  $W^+W^-$  final state Monte Carlo samples contain events with final states that correspond to a possible final state from a W-pair decay, independent of the actual production mechanism of the event. Included are e.g.  $e^+e^- \rightarrow W^+W^-$ ,  $e^+e^- \rightarrow W\nu_e$  and  $e^+e^- \rightarrow Z^0Z^0$  with *suitable* decays of the  $Z^0$  bosons.



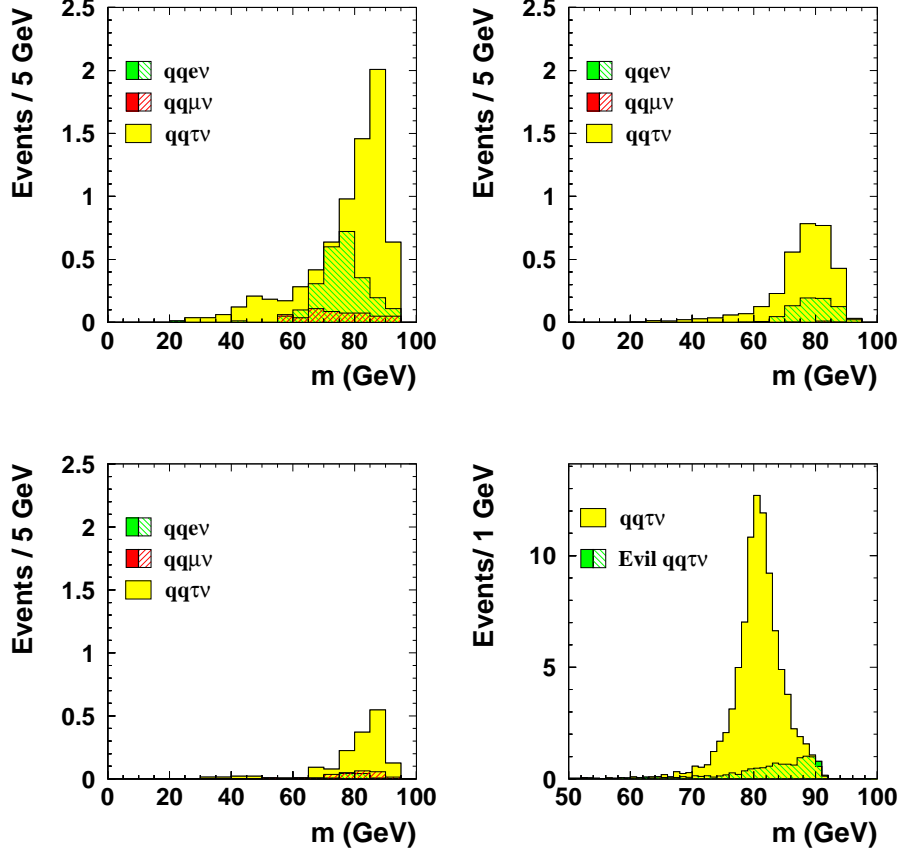


**Figure 8.9:** Top left: Shape of the  $Z^0/\gamma$  background at  $\sqrt{s} = 183$  GeV. Top right: Shape of the  $W\nu_e$  background at  $\sqrt{s} = 183$  GeV. Bottom left: Shape of the  $Z^0 Z^0$  background at  $\sqrt{s} = 183$  GeV. Bottom right: Distribution of the reconstructed mass for *Evil tau* events (green/grey) compared to  $W^+W^- \rightarrow q\bar{q}\tau\nu$  events (yellow/light grey) at  $\sqrt{s} = 183$  GeV; note the different bin size and scale compared to the other figures. The number of events are normalized to the integrated data luminosity of  $57 \text{ pb}^{-1}$ .

Channel	Background events				Data events
	$Z^0/\gamma$	$W\nu_e$	$Z^0 Z^0$	Evil taus	
$W^+W^- \rightarrow q\bar{q}e\bar{\nu}$	2.44	0.71	0.10	0	120
$W^+W^- \rightarrow q\bar{q}\mu\bar{\nu}$	0.54	0.02	0.24	0	112
$W^+W^- \rightarrow q\bar{q}\tau\bar{\nu}$	7.18	3.14	1.52	13.21	104

**Table 8.2:** Mean number of background events at  $\sqrt{s} = 183$  GeV, normalized to the integrated data luminosity of  $57 \text{ pb}^{-1}$ . For comparison, the number of selected events in the OPAL data at  $\sqrt{s} = 183$  GeV is also listed.

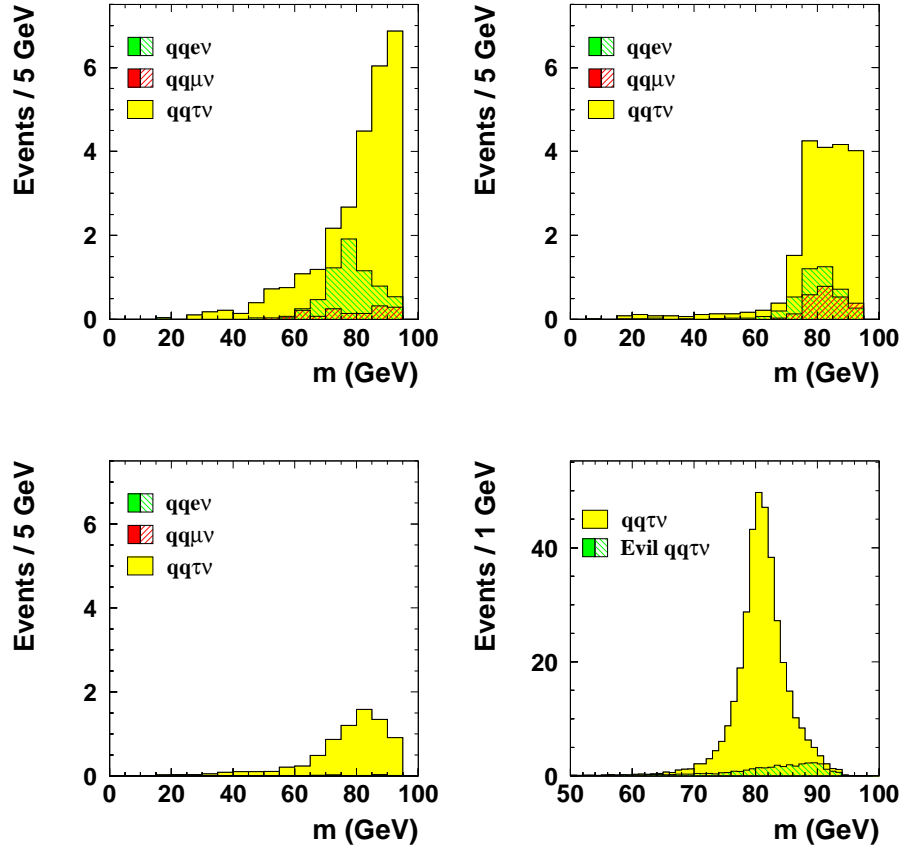


**Figure 8.10:** Top left: Shape of the  $Z^0/\gamma$  background at  $\sqrt{s} = 189$  GeV. Top right: Shape of the 4f background (non-WW final states) at  $\sqrt{s} = 189$  GeV. Bottom left: Shape of the 4f background (WW final states) at  $\sqrt{s} = 189$  GeV. Bottom right: Distribution of the reconstructed mass for *Evil tau* events (green/grey) compared to  $W^+W^- \rightarrow q\bar{q}\tau\bar{\nu}$  events (yellow/light grey); note the different bin size and scale compared to the other figures on this page. The number of events are normalized to the integrated data luminosity of  $183 \text{ pb}^{-1}$ .

Channel	$Z^0/\gamma$	Background events			Data events
		4f non-WW final states	4f WW	Evil taus	
$W^+W^- \rightarrow q\bar{q}e\bar{\nu}$	6.47	4.40	0.08	0	360
$W^+W^- \rightarrow q\bar{q}\mu\bar{\nu}$	1.55	2.49	0.01	0	370
$W^+W^- \rightarrow q\bar{q}\tau\bar{\nu}$	27.08	19.66	7.37	38.50	411

**Table 8.3:** Mean number of background events at  $\sqrt{s} = 189$  GeV, normalized to the integrated data luminosity of  $183 \text{ pb}^{-1}$ . For comparison, the number of selected events in the OPAL data at  $\sqrt{s} = 189$  GeV is also listed.

- $\Delta\chi^2 > 25$ ; a mass range  $[m_a, m_b]$  with  $\Delta\chi^2 = \chi^2(m_{a/b}) - \chi^2(m_{\min})$  around the minimal value  $\chi^2(m_{\min})$  is required to be found to ensure the proper normalization of the event probability density.
- $\chi^2$  smoothness;  $\chi^2(m)$  is required to be a continuous function.

The cut on the fit probability, as calculated with equation (7.11) from the input values and best estimates returned by the kinematic fit at the absolute minimum at  $m_{\min}$ , is a standard cut to reject badly reconstructed events which were selected as semileptonic W-pair decays, but do not match the hypothesis of two jets and a lepton-neutrino pair well. It is used by all W mass analyses in OPAL.

The last two cuts are used to reject events for which the calculation of the event probability density failed for technical reasons.

The number of selected events found in the data at  $\sqrt{s} = 183$  GeV ( $\sqrt{s} = 189$  GeV) after each consecutive cut is listed in table 8.4 (table 8.5).

Table 8.6 (table 8.7) lists the acceptance of the consecutive quality cuts at a center-of-mass energy of  $\sqrt{s} = 183$  GeV ( $\sqrt{s} = 189$  GeV). The acceptance as determined from the selected data events is in excellent agreement with the expected acceptance (in parentheses) as determined from a weighted average for the signal and background acceptances taken from Monte Carlo. The calculation of the expected acceptance is described in detail in appendix D.

The cut on the fit probability leads to the greatest loss of events, in the order of 5–10% of the signal events. Background events are rejected in a stronger manner, with a loss between 20–50%. Thus the cut on the fit probability further reduces the already small background contributions in the  $W^+W^- \rightarrow q\bar{q}\ell\bar{\nu}$  channel.

The combined loss from the other two cuts is less than 1% in all channels for the signal events and less than 2% for the background. The technical implementation of the analysis method therefore leads only to a negligible loss of statistics.

Contrary to other analysis methods no cut on the valid mass range for the W boson mass was applied.

### 8.2.5 Maximum Likelihood Fit

In the *Convolution method*, the mass of the W boson is determined with an unbinned maximum likelihood fit.

In a maximum likelihood fit the occurrence of the data is compared with a parent distribution which depends on the parameters that one likes to determine. Each event is assigned a probability that describes its likelihood of occurrence (hence the name of the method) assuming it originates from the parent distribution. For uncorrelated data, the total likelihood that the observed data sample originates from this distribution is given by the product of the individual probabilities. By varying the parameters of the distribution, the parameter set that maximizes the total likelihood and therefore describes the data best, can be determined. However, the method does not provide a *goodness-of-fit* value, as it is e.g. the case in  $\chi^2$ -fits; no absolute measure for the quality of the fit result exists. The choice of a sound parent distribution

Channel	Selected Events	$P > 0.001$	$\Delta\chi^2 \geq 25$	$\chi^2$ smoothness
$W^+W^- \rightarrow q\bar{q}e\bar{\nu}$	128	120	120	120
$W^+W^- \rightarrow q\bar{q}\mu\bar{\nu}$	116	113	112	112
$W^+W^- \rightarrow q\bar{q}\tau\bar{\nu}$	110	96	96	96

**Table 8.4:** Number of data events after consecutive cuts in the analysis at a center-of-mass energy of  $\sqrt{s} = 183$  GeV.

Channel	Selected Events	$P > 0.001$	$\Delta\chi^2 \geq 25$	$\chi^2$ smoothness
$W^+W^- \rightarrow q\bar{q}e\bar{\nu}$	396	364	362	360
$W^+W^- \rightarrow q\bar{q}\mu\bar{\nu}$	402	372	372	370
$W^+W^- \rightarrow q\bar{q}\tau\bar{\nu}$	455	413	411	411

**Table 8.5:** Number of data events after consecutive cuts in the analysis at a center-of-mass energy of  $\sqrt{s} = 189$  GeV.

Channel	Fit-Prob.	Cut	
		$\Delta\chi^2 > 25$	$\chi^2$ smoothness
$W^+W^- \rightarrow q\bar{q}e\bar{\nu}$	$93.8 \pm 3.0\%$ ( $94.9 \pm 0.3\%$ )	100% ( $99.6 \pm 0.1\%$ )	100% ( $99.2 \pm 0.1\%$ )
$W^+W^- \rightarrow q\bar{q}\mu\bar{\nu}$	$97.4 \pm 2.1\%$ ( $94.7 \pm 0.3\%$ )	$99.1 \pm 1.2\%$ ( $99.6 \pm 0.1\%$ )	100% ( $99.8 \pm 0.1\%$ )
$W^+W^- \rightarrow q\bar{q}\tau\bar{\nu}$	$87.3 \pm 4.4\%$ ( $88.1 \pm 0.4\%$ )	100% ( $99.8 \pm 0.1\%$ )	100% ( $99.4 \pm 0.1\%$ )

**Table 8.6:** Acceptance of the consecutive data quality cuts for data and the expected acceptance (in parentheses) as determined from Monte Carlo samples at a center-of-mass energy of  $\sqrt{s} = 183$  GeV.

Channel	Fit-Prob.	Cut	
		$\Delta\chi^2 > 25$	$\chi^2$ smoothness
$W^+W^- \rightarrow q\bar{q}e\bar{\nu}$	$91.9 \pm 1.9\%$ ( $92.2 \pm 0.2\%$ )	$99.5 \pm 0.5\%$ ( $99.7 \pm 0.1\%$ )	$99.4 \pm 0.6\%$ ( $99.5 \pm 0.1\%$ )
$W^+W^- \rightarrow q\bar{q}\mu\bar{\nu}$	$92.5 \pm 1.8\%$ ( $93.8 \pm 0.2\%$ )	100% ( $99.7 \pm 0.1\%$ )	$99.5 \pm 0.5\%$ ( $99.9 \pm 0.1\%$ )
$W^+W^- \rightarrow q\bar{q}\tau\bar{\nu}$	$90.8 \pm 1.9\%$ ( $90.3 \pm 0.3\%$ )	$99.5 \pm 0.5\%$ ( $99.6 \pm 0.1\%$ )	100% ( $99.8 \pm 0.1\%$ )

**Table 8.7:** Acceptance of the consecutive data quality cuts for data and the expected acceptance (in parentheses) as determined from Monte Carlo samples at a center-of-mass energy of  $\sqrt{s} = 189$  GeV.

that describes the expected distribution of the data is therefore essential to obtain sensible results. In computational implementations of the method, the logarithm of the likelihood is maximized instead the likelihood itself. The logarithm transforms the likelihood to a function that varies more slowly with its parameters, in order to avoid problems due to the finite numerical precision and therefore limited minimum step-size available in computers. The maximum likelihood fit also allows the calculation of the covariance matrix of the parameters by tracing the contour of the likelihood in the vicinity of the maximum. A paraboloid shape of the likelihood corresponds to Gaussian errors.

The *Convolution method* only uses a 1-dimensional likelihood, the only free parameter is the mass of the W boson as its width is constraint to the Standard model value. The 68% confidence level of the estimated parameters corresponds to the range of the parameters for which the likelihood value is reduced to  $\mathcal{L} = \exp(-1/2) \mathcal{L}_{\max}$ ; in the case of Gaussian parameter errors this value is equivalent to the  $1 \sigma$  error interval.

In the *Convolution method* the event likelihood  $\mathcal{L}_i(M_W, \Gamma_W)$  is given by the convolution of the event probability density  $P_i(m)$  with the physics function  $f(m; M_W, \Gamma_W, \sqrt{s})$ :

$$\mathcal{L}_i(M_W, \Gamma_W) = \int f(m'; M_W, \Gamma_W, \sqrt{s}) P_i(m') dm'. \quad (8.19)$$

The total likelihood-function is the product of the event likelihoods, as the individual events represent independent measurements of the properties of the W boson,

$$\mathcal{L}(M_W, \Gamma_W) = \prod_{i=1}^{N_{\text{obs}}} \mathcal{L}_i(M_W, \Gamma_W), \quad (8.20)$$

where  $N_{\text{obs}}$  denotes the number of events in the data sample.

To obtain the  $M_W$  and its error for the data sample, the total likelihood function is maximized using the Standard Model relation between  $M_W$  and  $\Gamma_W$  [11, 55],

$$\Gamma_W = 2.0817 \left( \frac{M_W}{80.26 \text{ GeV}} \right)^3. \quad (8.21)$$

The measurement of the mass of the W boson is carried out separately in each of the three decay channels,  $W^+W^- \rightarrow q\bar{q}e\bar{\nu}$ ,  $W^+W^- \rightarrow q\bar{q}\mu\bar{\nu}$ , and  $W^+W^- \rightarrow q\bar{q}\tau\bar{\nu}$ , since systematic uncertainties, the statistical precision of the measurements and the background contributions vary widely; furthermore the individual fits allow a comparison and consistency check of the results for the different decay channels.

The combined result  $M_W$  for all channels is determined with a minimization of the  $\chi^2$ -function

$$\chi^2 = (M_{W,i} - M_W) G_{ij} (M_{W,i} - M_W) \quad (8.22)$$

where  $M_{W,i}$  denotes the measured mass in the  $i$ -th decay channel and G the inverse of the covariance matrix C of the measurements. The covariance matrix C is given

by the sum of the covariance matrices for the statistical errors and the systematic errors,

$$C = C_{\text{stat}} + \sum_{\text{all syst. errors}} C_{\text{sys}}. \quad (8.23)$$

For the statistical errors and uncorrelated systematic errors the covariance matrices are diagonal and the entries are the squared errors. In the case of correlated errors the additional off-diagonal elements are given by the product of the correlation coefficient and the errors in the corresponding channels.

The above described method takes correlated systematic errors correctly into account, but has the drawback that the distinction between the statistical and systematic error is lost, only the calculation of the total error on the combined value is possible.

As an alternative combination method the correlation between the systematic uncertainties are neglected in the combination and only the diagonal elements of the covariance matrix are taken into account. This is justified by the fact that only a small number of systematic uncertainties are correlated and that the statistical error dominates the overall uncertainty of the measurements. The advantage of this method is that it allows to retain the distinction between the statistical and the systematic error. Considering only the diagonal elements of the covariance matrix, the  $\chi^2$ -minimization reduces to a weighted average,

$$M_W = \frac{1}{\sum_{i=1}^3 1/\sigma_i^2} \sum_{i=1}^3 \frac{M_{W,i}}{\sigma_i^2}, \quad (8.24)$$

with the weights  $\sigma_i$  given by the quadratic sum of the statistical and the systematic errors,

$$\sigma_i^2 = \sigma_{i, \text{stat}}^2 + \sum_{\text{all syst. errors}} \sigma_{i, \text{sys}}^2. \quad (8.25)$$

The total statistic error  $\delta_{M_W}$  of the combined mass  $M_W$  is estimated by

$$\delta_{M_W, \text{stat}} = \frac{1}{\sum_{i=1}^3 1/\sigma_i^2} \sqrt{\sum_{i=1}^3 \left( \frac{\sigma_{i, \text{stat}}}{\sigma_i^2} \right)^2}, \quad (8.26)$$

while the total systematic error is calculated as described in section 8.6, taking into account possible correlations between the decay channels to avoid an under- or overestimation of these errors.

Both methods yield consistent results, see chapter 9.

### 8.3 Ensemble Tests

Ensemble tests provide a powerful method to determine the validity and quality of analyses. The analysis method is tested against an ensemble of data-sized Monte Carlo experiments and statistical methods can be applied to interpret the results.

This section describes the general method used in ensemble tests. In subsequent sections, ensemble tests are used to study the bias of the analysis method, to estimate the expected statistical error, and to obtain errors for systematic effects.

As is the case for the actual analysis, the ensemble tests are carried out separately for each decay channel,  $W^+W^- \rightarrow q\bar{q}e\bar{\nu}$ ,  $W^+W^- \rightarrow q\bar{q}\mu\bar{\nu}$ , and  $W^+W^- \rightarrow q\bar{q}\tau\bar{\nu}$ . The individual samples of the ensemble are obtained from Monte Carlo simulations in the following way: The data taken with the OPAL detector is analyzed to determine the number of selected events in each of the three semileptonic decay channels,  $W^+W^- \rightarrow q\bar{q}e\bar{\nu}$ ,  $W^+W^- \rightarrow q\bar{q}\mu\bar{\nu}$ , and  $W^+W^- \rightarrow q\bar{q}\tau\bar{\nu}$ . If required for the purpose of the analysis<sup>6</sup>, the mean number of background events and their mass distribution is determined for each different background source by analyzing corresponding Monte Carlo data using the same selections and cuts as for the data events and scaling the number of accepted events to the integrated data luminosity. The mean number and background shape are then used to complete the description and normalization of the physics function, compare equation (8.18). In each sample the number of included background events for the  $Z^0/\gamma$  and four-fermion backgrounds is determined randomly from a Poisson distribution with the corresponding mean value; for the *Evil tau* background no additional events are included as they are part of the signal Monte Carlo. To minimize correlations between the individual samples of the ensemble the background events are used only once<sup>7</sup>. After the number of background events is known, the missing number of events are taken from a signal Monte Carlo, thus completing the sample.

The *Convolution method* is then applied to the samples of the ensemble and yields for each sample a value of the mass of the W boson. The mean reconstructed mass  $M_{\text{Fit}}$  of the W boson and its error are extracted by a Gaussian fit to the mass distribution of the samples of the ensemble.

For the bias test and systematic studies the events from the signal Monte Carlos are used only once, and the number of samples in the ensemble is given by the ratio  $R = n_{\text{MC}}/n_{\text{Data}}$  of Monte Carlo events to data events in each channel. For a center-of-mass energy of  $\sqrt{s} = 183$  GeV this ratio is around 100 which limits the precision of the ensemble test to a statistical error of 10% while for a center-of-mass energy of  $\sqrt{s} = 189$  GeV the ratio is around 50 which limits the precision to 14%.

The expected statistical error of the analysis is also obtained from an ensemble test. It has been shown [56] that the number of samples in an ensemble can be increased up to  $R^2$  if the events in each sample are chosen randomly from the signal Monte Carlo. The price for this method is a possible bias in the mean value of the obtained distributions; the width of the distribution should, however, remain unbiased. Since the determination of the expected statistical error is solely based on the width of the mass distribution of the ensemble, we use this method to improve

<sup>6</sup>E.g. for the determination of the calibration functions, the expected statistical error or the study of systematic uncertainties associated with the background.

<sup>7</sup>Due to the finite statistics of the background Monte Carlo samples it can happen that the number of selected background events is not sufficient for all the samples in the ensemble. In this case, events are reused from a randomly chosen event onwards.

the statistical precision of the test to 1% for a center-of-mass energy of  $\sqrt{s} = 183$  GeV and to 2% for a center-of-mass energy of  $\sqrt{s} = 189$  GeV.

## 8.4 Bias Correction and Calibration

The *Convolution method* cannot be expected to be totally bias free. While the signal part of the physics function describes the expected mass distribution well, it does not take into account the effects of the event selection which lead to deviations from the Breit-Wigner shape. The background modeling in the physics function is based on Monte Carlo simulations and depends for some of the four-fermion backgrounds on the mass of the W boson. Furthermore the radiator function  $Q(s', s)$ , which describes the probability of ISR emission, is taken from a single Monte Carlo simulation with a value  $M_W = 80.33$  GeV for the mass of the W boson for each center-of-mass energy.

All these effects, for which no analytical description exists and which thus cannot be included properly in the physics function, can introduce small deviations from the true mass of the W boson and can bias the measurement.

To calibrate the *Convolution method* samples containing the same number of events as observed in the data were selected from Monte-Carlo with different input masses  $M_{\text{True}}$ ; background was included in the samples on a random basis as described in section 8.3. The mean reconstructed W mass  $M_{\text{Fit}}$  and its error were determined from the mass distribution of the ensemble for each Monte Carlo simulation. A straight line fit

$$(M_{\text{Fit}} - 80.33 \text{ GeV}) = \alpha + \beta (M_{\text{True}} - 80.33 \text{ GeV}) \quad (8.27)$$

was used to determine the bias correction function. The evaluation is carried out around a central mass value of 80.33 GeV to minimize the correlation between the offset  $\alpha$  and the slope parameter  $\beta$  of the fit.

The bias correction of the mass measurement is based on the inverse calibration functions  $M_{\text{True}}(M_{\text{Fit}})$ , evaluated at the measured mass,

$$M_{\text{True}} = \frac{M_{\text{Meas}} - \alpha}{\beta} + \left(1 - \frac{1}{\beta}\right) 80.33 \text{ GeV} \quad (8.28)$$

The finite number of Monte Carlo events used in the determination of the calibration functions leads to an error on the bias correction. This error is included in the systematic uncertainties of the results, see section 8.6.

The calibration function is also used to correct the estimates of the statistical error of the W mass measurement with the *Convolution method*. The statistical errors obtained from the maximum likelihood fit are scaled by the inverse derivatives of the calibration functions  $1/\beta$ , to take into account a possible loss of sensitivity introduced by residual effects, e.g. the ISR spectrum used in the calculation of the physics function, which can bias the measurement towards particular mass values of Monte Carlo generation.



Channel	$\alpha$ / GeV	$\beta$
$W^+W^- \rightarrow q\bar{q}e\bar{\nu}$	$-0.071 \pm 0.015$	$0.952 \pm 0.024$
$W^+W^- \rightarrow q\bar{q}\mu\bar{\nu}$	$-0.069 \pm 0.017$	$0.924 \pm 0.026$
$W^+W^- \rightarrow q\bar{q}\tau\bar{\nu}$	$-0.052 \pm 0.021$	$0.948 \pm 0.030$

**Table 8.8:** Coefficients of the calibration functions at a center-of-mass energy of  $\sqrt{s} = 183$  GeV.  $\alpha$  is the (negative) bias at  $M_{\text{True}} = 80.33$  GeV,  $\beta$  is the slope of the straight line fit.

Channel	$\alpha$ / GeV	$\beta$
$W^+W^- \rightarrow q\bar{q}e\bar{\nu}$	$0.056 \pm 0.019$	$0.988 \pm 0.051$
$W^+W^- \rightarrow q\bar{q}\mu\bar{\nu}$	$-0.001 \pm 0.020$	$0.977 \pm 0.056$
$W^+W^- \rightarrow q\bar{q}\tau\bar{\nu}$	$-0.030 \pm 0.017$	$0.995 \pm 0.055$

**Table 8.9:** Coefficients of the calibration functions at a center-of-mass energy of  $\sqrt{s} = 189$  GeV.  $\alpha$  is the (negative) bias at  $M_{\text{True}} = 80.33$  GeV,  $\beta$  is the slope of the straight line fit.

Figure 8.11 and figure 8.12 show the calibration function for the center-of-mass energies of  $\sqrt{s} = 183$  GeV and  $\sqrt{s} = 189$  GeV, table 8.8 and table 8.9 list the coefficients of the obtained calibration functions.

For all decay channels and for both center-of-mass energies, the calibration is well described by a straight line fit. The *Convolution method* is found to exhibit only a small bias of less than 100 MeV and the slopes of the calibration functions are consistent with unity.

## 8.5 Expected Statistical Errors

To obtain the expected statistical error of the *Convolution method*, an ensemble test was performed with Monte-Carlo data.

To improve the statistical precision of this ensemble test, the number of samples was increased to the square of the ratio of Monte Carlo to data events by using randomly picked events in each sample [56]. For a center-of-mass energy of  $\sqrt{s} = 183$  GeV this ratio is greater than 100 and 10000 samples were created to form the ensemble, for a center-of-mass energy of  $\sqrt{s} = 189$  GeV the ratio is greater than 50 and 2500 samples were created.

The number of  $W^+W^- \rightarrow q\bar{q}e\bar{\nu}$ ,  $W^+W^- \rightarrow q\bar{q}\mu\bar{\nu}$  and  $W^+W^- \rightarrow q\bar{q}\tau\bar{\nu}$  events in each subsample was chosen to be equal to the observed number of events in the data sample for each channel, background events were included randomly as detailed in section 8.3.

The estimated statistical error is given by the width of the mass distribution of the ensemble.

A further useful quantity that can be calculated from the individual results and their errors is the width of the pull distribution.

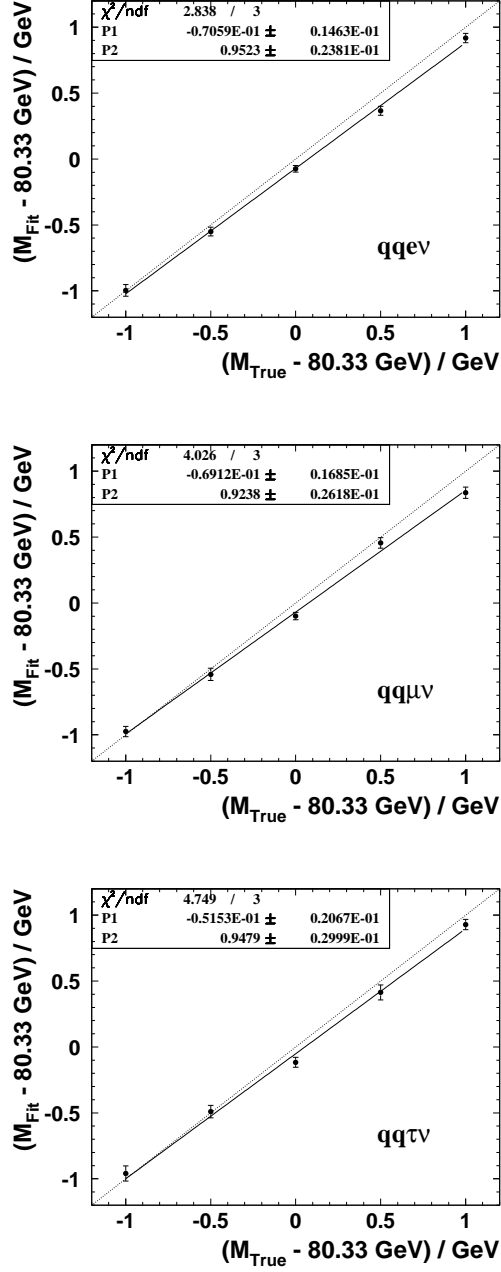


**Figure 8.11:** Calibration functions for  $M_W$  in the  $W^+W^- \rightarrow q\bar{q}e\bar{\nu}$ ,  $W^+W^- \rightarrow q\bar{q}\mu\bar{\nu}$ , and  $W^+W^- \rightarrow q\bar{q}\tau\bar{\nu}$  decay channels at  $\sqrt{s} = 183 \text{ GeV}$ .  $M_{\text{True}}$  denotes the Monte Carlo input value,  $M_{\text{Fit}}$  the fitted value.

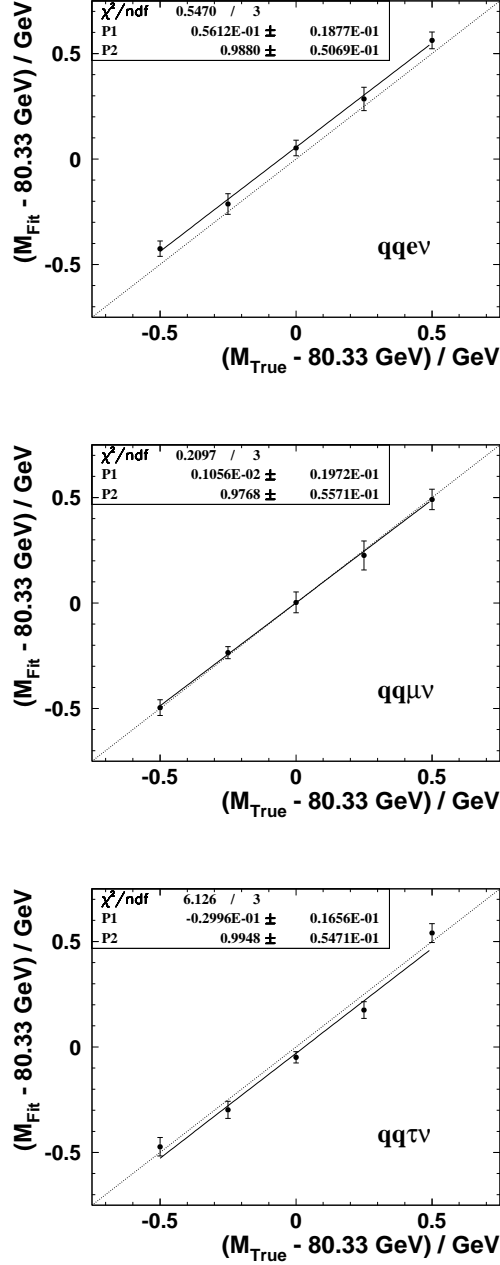


**Figure 8.12:** Calibration functions for  $M_W$  in the  $W^+W^- \rightarrow q\bar{q}e\bar{\nu}$ ,  $W^+W^- \rightarrow q\bar{q}\mu\bar{\nu}$ , and  $W^+W^- \rightarrow q\bar{q}\tau\bar{\nu}$  decay channels at  $\sqrt{s} = 189 \text{ GeV}$ .  $M_{\text{True}}$  denotes the Monte Carlo input value,  $M_{\text{Fit}}$  the fitted value.

The pull value  $P$  is defined by the deviation of the measured value  $x_{\text{Meas}}$  from the true value  $x_{\text{True}}$  compared to the error  $\sigma_{\text{Meas}}$  of the measurement,

$$P = \frac{x_{\text{Meas}} - x_{\text{True}}}{\sigma_{\text{Meas}}}. \quad (8.29)$$

If the measured values exhibit only statistical fluctuations and their errors are calculated or estimated correctly, the pulls are distributed according to a Gaussian with mean 0 and a unit width. A deviation of the mean value of the pull distribution from 0 points to systematic shifts in the measurement process, while a deviation of the pull width from unity occurs if the individual errors are too large (pull width smaller than one) or too small (pull width larger than one). If the pull distribution does not correspond to a Gaussian, the method has inherent problems and the results do not only have statistical fluctuations.

The pull distribution is calculated from the mass and the error of the individual mass measurements in the ensemble. As for the mass distributions themselves, the mean value of the pull distributions is not further used in this ensemble test because the events were reused and the samples are no longer uncorrelated. Nevertheless the width information can be used to check the error estimates returned by the *Convolution method*; systematic shifts are already determined and corrected for by the calibration functions, see section 8.4.

For both center-of-mass energies,  $\sqrt{s} = 183$  GeV and  $\sqrt{s} = 189$  GeV, and all decay channels,  $W^+W^- \rightarrow q\bar{q}e\bar{\nu}$ ,  $W^+W^- \rightarrow q\bar{q}\mu\bar{\nu}$ , and  $W^+W^- \rightarrow q\bar{q}\tau\bar{\nu}$ , the width of the pull distribution is consistent with unity and the shape of the distributions is well described by a Gaussian. The error estimate on the W mass in a single measurement returned by the *Convolution method* is reliable. As for the slope of the calibration function, a correction factor for the statistical error is applied by multiplying the error with the width of the corresponding pull distribution, which only leads to small corrections less than 3%. Figure 8.13 and figure 8.14 show the results of the ensemble test with 10000 samples for a center-of-mass energy of  $\sqrt{s} = 183$  GeV and 2500 samples for a center-of-mass energy of  $\sqrt{s} = 189$  GeV. On the left side the mass distributions for the three semileptonic decay channels are plotted, on the right side the pull distributions of the measured W masses; in both cases the distributions have been fitted with a Gaussian. Table 8.10 and table 8.11 list the expected statistical errors and the width of the pull distributions for the center-of-mass energies of  $\sqrt{s} = 183$  GeV and  $\sqrt{s} = 189$  GeV. The statistical errors have already been corrected by the inverse slope of the corresponding calibration function and scaled with the width of the pull distribution.

## 8.6 Systematic Uncertainties

The accuracy of a measurement of the mass of the W boson is not only determined by the statistical precision due to the finite number of recorded events, but also by systematic uncertainties. Sources of systematic errors are other measurements

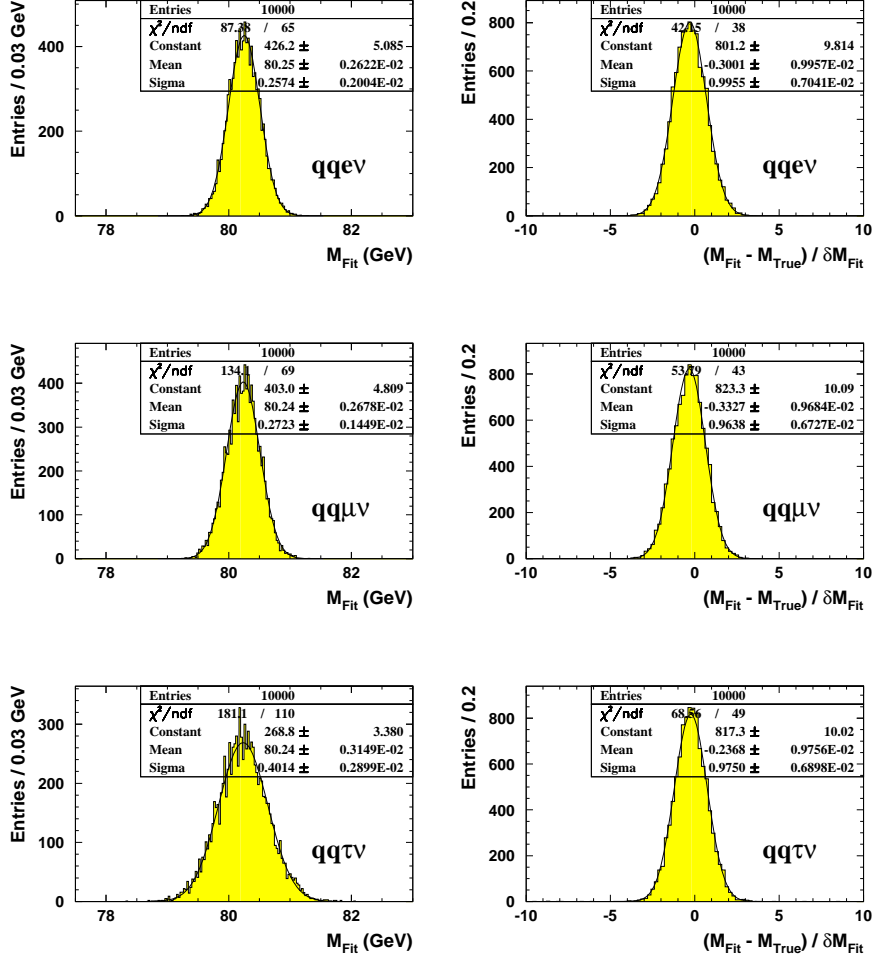


**Figure 8.13:**  $W$  mass (left) and pull (right) distributions of the ensemble test for a center-of-mass energy  $\sqrt{s} = 183$  GeV. The expected statistical error (before scaling with the inverse slope of the calibration function) is given by the width of the  $M_W$  distribution.

Channel	Exp. error / GeV	Pull width
$W^+W^- \rightarrow q\bar{q}e\bar{\nu}$	$0.269 \pm 0.003$	$1.00 \pm 0.01$
$W^+W^- \rightarrow q\bar{q}\mu\bar{\nu}$	$0.284 \pm 0.002$	$0.96 \pm 0.01$
$W^+W^- \rightarrow q\bar{q}\tau\bar{\nu}$	$0.413 \pm 0.004$	$0.98 \pm 0.01$
$W^+W^- \rightarrow q\bar{q}\ell\bar{\nu}$	$0.177 \pm 0.001$	

**Table 8.10:** Expected statistical error and pull width for the ensemble test at a center-of-mass energy of  $\sqrt{s} = 183$  GeV (MC input values  $M_W = 80.33$  GeV and  $\Gamma_W = 2.0933$  GeV). The results are scaled with the inverse slope of the calibration function (compare table 8.8) and the pull width.

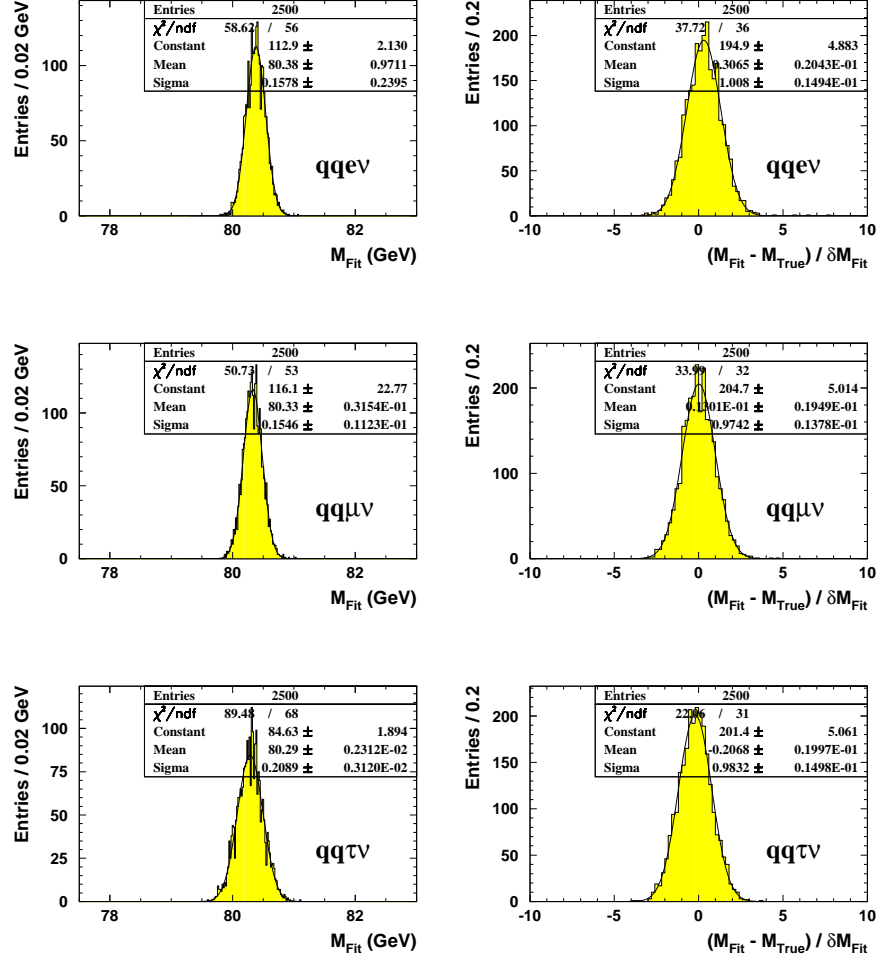


**Figure 8.14:** W mass (left) and pull (right) distributions of the ensemble test for a center-of-mass energy  $\sqrt{s} = 189$  GeV. The expected statistical error (before scaling with the inverse slope of the calibration function) is given by the width of the  $M_W$  distribution.

Channel	Exp. error / GeV	Pull width
$W^+W^- \rightarrow q\bar{q}e\bar{\nu}$	$0.161 \pm 0.002$	$1.01 \pm 0.01$
$W^+W^- \rightarrow q\bar{q}\mu\bar{\nu}$	$0.154 \pm 0.002$	$0.97 \pm 0.01$
$W^+W^- \rightarrow q\bar{q}\tau\bar{\nu}$	$0.206 \pm 0.003$	$0.98 \pm 0.01$
$W^+W^- \rightarrow q\bar{q}\ell\bar{\nu}$	$0.098 \pm 0.003$	

**Table 8.11:** Expected statistical error and pull width for the ensemble test at a center-of-mass energy of  $\sqrt{s} = 189$  GeV (MC input values  $M_W = 80.33$  GeV and  $\Gamma_W = 2.0933$  GeV). The results are scaled with the inverse slope of the calibration (compare table 8.9) function and the pull width.

which influence parameters used in the mass measurement (e.g. the beam energy or background acceptance measurements), uncertainties and incomplete modeling in the Monte Carlo simulation (e.g. detector response, hadronization and four-fermion interference effects) as well as the finite Monte Carlo statistics and changes to the fit procedure.

The study of systematic errors is based in most cases on the comparison of an ensemble of Monte-Carlo samples which include corrections for one effect, henceforth called *systematic ensemble*, with an unaltered set of samples, called *reference ensemble*. Details on the Monte Carlo samples used in the study of the systematic uncertainties can be found in appendix E. Each sample contains the same number of events as observed for the data. The systematic uncertainties are evaluated for each decay channel,  $W^+W^- \rightarrow q\bar{q}e\bar{\nu}$ ,  $W^+W^- \rightarrow q\bar{q}\mu\bar{\nu}$ , and  $W^+W^- \rightarrow q\bar{q}\tau\bar{\nu}$  separately.

For the *systematic* as well as for the *reference ensemble* the mean value  $\langle M \rangle$  of the measured W boson mass is calculated as

$$\langle M \rangle = \frac{1}{N_{\text{Sample}}} \sum_{i=1}^{N_{\text{Sample}}} M_i, \quad (8.30)$$

where  $M_i$  denotes the value of the W mass obtained from the fit to the  $i$ -th sample and  $N_{\text{Sample}}$  is the number of samples in the ensemble.

The error  $\delta\langle M \rangle$  of the mean measured W mass is given by

$$(\delta\langle M \rangle)^2 = \frac{1}{N_{\text{Sample}}(N_{\text{Sample}} - 1)} \sum_{i=1}^{N_{\text{Sample}}} (M_i - \langle M \rangle)^2. \quad (8.31)$$

The bias  $\Delta M_W$  on the measurement of the mass of the W boson is estimated by

$$\Delta M_W = \langle M^s \rangle - \langle M^r \rangle, \quad (8.32)$$

where  $\langle M^s \rangle$  is the mean measured W mass of the *systematic ensemble* and  $\langle M^r \rangle$  the mean measured W mass of the *reference ensemble*.

The ensemble test also allows the calculation of the correlation coefficient  $\rho$  between the systematic and the reference sets:

$$\rho = \frac{1}{N_{\text{Sample}} - 1} \sum_{i=1}^{N_{\text{Sample}}} \frac{(M_i^s - \langle M^s \rangle)(M_i^r - \langle M^r \rangle)}{\delta\langle M^s \rangle \delta\langle M^r \rangle}, \quad (8.33)$$

where  $M_i^s$  is the measured W mass of the  $i$ -th sample in the *systematic ensemble* and  $M_i^r$  that of the  $i$ -th sample in the *reference ensemble*. Many systematic studies use the *postgenerator* scheme—the events in the *reference* and the *systematic sample* are identical up to the parton level and differences are introduced in the *systematic sample* only afterwards, thus decoupling the event generation from the systematic effect under study—which leads to a high correlation. For uncorrelated

systematic uncertainties the correlation coefficient is 0, for fully correlated systematic uncertainties it is 1.

The error  $\delta\Delta M_W$  of the bias is calculated—taking into account the correlation of the ensembles—as

$$(\delta\Delta M_W)^2 = (\delta\langle M^s \rangle)^2 + (\delta\langle M^r \rangle)^2 - 2\rho \delta\langle M^s \rangle \delta\langle M^r \rangle. \quad (8.34)$$

The systematic uncertainty assigned to a specific source is the bias of the mean measured W mass; in the case that this bias is consistent with 0 within the  $1\sigma$  error interval, the error on the bias is taken as a conservative estimate of the systematic uncertainty.

The calculation of the systematic uncertainty that is given for the combined result of all three decay channels depends on whether the source is correlated or uncorrelated between the different decays modes. In the case of an uncorrelated source<sup>8</sup>, the three systematic errors are combined in a weighted average, using the statistical errors of the mass measurement of the data sample and their systematic uncertainties in the decay channels as weights. In the case of a correlated source<sup>9</sup>, the results of the three decay channels are combined in a weighted average, again using the statistical errors of the mass measurement of the data sample and their systematic uncertainties in the decay channels as weights, before the bias and its error are calculated.

The total systematic uncertainty  $\delta_{\text{sys}}$  of the measurement of the W mass is calculated as the sum of the squares of the individual systematic uncertainties,

$$\delta_{\text{sys}}^2 = \sum_i \delta_{i, \text{sys}}^2. \quad (8.35)$$

The following systematic uncertainties were considered. Table 8.13 summarizes the results for the different channels and the combined result for a center-of-mass energy of  $\sqrt{s} = 183$  GeV, table 8.13 for a center-of-mass energy of  $\sqrt{s} = 189$  GeV.

- **Beam Energy Uncertainty:**

The average LEP beam energy  $E_{\text{Beam}}$  is currently known with a precision of  $\delta E_{\text{Beam}} = 25$  MeV for a center-of-mass energy of  $\sqrt{s} = 183$  GeV [57] and with a precision of  $\delta E_{\text{Beam}} = 20$  MeV for a center-of-mass energy of  $\sqrt{s} = 189$  GeV [58].

To estimate the systematic uncertainty, 25 MeV were added to the nominal beam energy used in the kinematic fit routine for the *systematic ensembles*. The results were scaled to the quoted beam energy uncertainties and are consistent with the expected shift of  $\delta M_W = \delta E_{\text{Beam}} M_W / E_{\text{Beam}}$ , that can

<sup>8</sup>Uncorrelated sources are the lepton energy scale, the lepton errors, 4-fermion effects, and the background scale.

<sup>9</sup>Correlated sources are the beam energy uncertainty, the jet energy scale, the jet errors, the *Initial State Radiation* modeling, the hadronization model, and the fit procedure.



be derived from equation (8.12) by rewriting it in terms of the beam energy  $E_{\text{Beam}} = \sqrt{s}/2$ .

The influence of the spread of the beam energy [57, 58] on the mass measurement has also been studied and can be neglected.

- **Bias Correction Error:**

The precision in the determination of the coefficients of the calibration functions (compare chapter 8.4, equation (8.27)) is limited by the available number of Monte Carlo data to form the samples of the ensemble test. The uncertainty of the coefficients of the calibration function was translated to an error  $\delta_{\text{Bias}}$  on the bias correction,

$$\delta_{\text{Bias}}^2 = \left( \frac{\delta\alpha}{\beta} \right)^2 + \left( \frac{M_{\text{Meas}} - 80.33 \text{ GeV} - \alpha}{\beta^2} \delta\beta \right)^2, \quad (8.36)$$

where  $\alpha$  denotes the offset of the calibration function,  $\delta\alpha$  the error on the offset,  $\beta$  the slope,  $\delta\beta$  the error on the slope and  $M_{\text{Meas}}$  the measured mass in the data.

- **Initial State Radiation Modeling:**

For the data taken at a center-of-mass energy of  $\sqrt{s} = 189 \text{ GeV}$  the estimate of the uncertainty associated with the modeling of the *Initial State Radiation* (ISR) is based on an ensemble test. A KORALW Monte Carlo sample with an  $\mathcal{O}(\alpha^3)$  treatment of the ISR forms the *reference ensemble*. In the *systematic ensemble* the event likelihoods  $\mathcal{L}_i$  are reweighted to correspond to an  $\mathcal{O}(\alpha^1)$  treatment, using the ratio  $p_i$  of the matrix elements  $|M_{1,i}|^2$  for 1st and  $|M_{3,i}|^2$  for 3rd order ISR of the event as calculated in KORALW,

$$\mathcal{L}_i \rightarrow \mathcal{L}_i^{p_i} = \mathcal{L}_i^{|M_{1,i}|^2/|M_{3,i}|^2}. \quad (8.37)$$

For a center-of-mass energy of  $\sqrt{s} = 183 \text{ GeV}$  these relative probabilities are not included in the currently available Monte Carlo samples. The uncertainty is derived from the difference in the mean photon energy of the ISR spectrum for an  $\mathcal{O}(\alpha^2)$  calculation with a  $\mathcal{O}(\alpha^1)$  calculation. This difference is scaled by the ratio of the beam energy to the mass of the W boson to estimate the uncertainty on the mass measurement.

- **Detector Calibration and Simulation:**

The effects of detector mis-calibrations and deficiencies in the detector simulation are investigated by varying the jet and lepton energy scales and resolutions over reasonable ranges as estimated from a detailed comparison of  $Z^0$  calibration data and Monte Carlo.

For a center-of-mass energy of  $\sqrt{s} = 189 \text{ GeV}$  the study is based on the implementation of these variations in the OPAL WW analysis framework [37,

Quantity	Scaling factor
Jet energy scale	1.01
Jet energy resolution	1.03
Jet angular resolution	1.05
Lepton energy scale	1.005
Lepton energy resolution	1.03
Lepton angular resolution	1.05

**Table 8.12:** Scaling factors for the study of detector calibration and simulation effects at a center-of-mass energy of  $\sqrt{s} = 183$  GeV.

48]; corrections applied to the Monte-Carlo data were changed within their uncertainties and used to assign a systematic error.

Each correction (jet/lepton energy scale, jet/lepton energy errors and angular errors) was varied separately.

For a center-of-mass energy of  $\sqrt{s} = 183$  GeV a less sophisticated approach was used, as the corresponding routine [48] of the WW analysis framework cannot be applied. The energy scales and energy and angular resolutions are scaled by global correction factors as listed table 8.12.

- **Hadronization Model:**

The simulation of the hadronization in the Monte Carlo samples that are used as a reference for the mass measurement is based on the JETSET string fragmentation scheme for  $W \rightarrow q\bar{q}$  decays. As a test of the fragmentation uncertainties the JETSET string model is replaced by the HERWIG cluster model in the generation of the *systematic ensemble*.

- **Four-fermion Effects:**

Possible systematic effects associated with the modeling of the four-fermion final states, especially interference effects between the  $W^+W^-$  diagrams and other four-fermion processes, are investigated.

For a center-of-mass energy of  $\sqrt{s} = 189$  GeV the uncertainties are estimated by reweighting the event likelihoods  $\mathcal{L}_i$  from `grc4f` matrix elements  $|M_{\text{grc}}|^2$  to correspond to EXCALIBUR matrix elements  $|M_{\text{exc}}|^2$ ,

$$\mathcal{L}_i \rightarrow \mathcal{L}_i^{p_i} = \mathcal{L}_i \frac{|M_{\text{exc},i}|^2}{|M_{\text{grc},i}|^2}. \quad (8.38)$$

where  $p_i$  is the ratio of the EXCALIBUR and the `grc4f` matrix elements for the event. This corresponds effectively to an implementation of a different four-fermion Monte Carlo generator.

For a center-of-mass energy of  $\sqrt{s} = 183$  GeV the uncertainties are estimated by comparing the results of `grc4f` Monte Carlos using only CC03 diagrams and using the full set of interfering diagrams.

- **Fit Procedure:**

The validity of the fit procedure used in the *Convolution method* was tested.

The uncertainty introduced by the numerical normalization of the event probability density was evaluated by comparing ensembles with a convolution range corresponding to a  $\Delta\chi^2 = 25$  and  $\Delta\chi^2 = 16$  (for Gaussian event probability densities this would correspond to change from a "5 $\sigma$ " range to a "4 $\sigma$ " range). No perceptible change in the results was observed.

The weight of the penalty factors for the energy and equal mass constraint in the calculation of the  $\chi^2(m)$ -function was increased by a factor 10. No perceptible change was observed in the results for the  $W^+W^- \rightarrow q\bar{q}e\bar{\nu}$  and  $W^+W^- \rightarrow q\bar{q}\mu\bar{\nu}$  channels. The  $W^+W^- \rightarrow q\bar{q}\tau\bar{\nu}$  channel, which uses a less stringent penalty factor for the equal mass constraint, shows a slight dependency on the value of the penalty factors. For details compare appendix B.

- **Background Treatment:**

To estimate the systematic error associated with the background normalization the mean number of  $Z^0/\gamma$  and four-fermion background events was increased according to the uncertainty in the accepted cross section in the event selections [18, 59].

The systematic uncertainties related with the description of the underlying physics—hadronization, four-fermion effects and background normalization—are all compatible with 0 MeV within their statistical errors induced by the available number of Monte Carlo events or are negligible. The only exception is the estimate of the effect of the ISR modeling at  $\sqrt{s} = 183$  GeV, which is calculated in a very conservative way.

The detector calibration and uncertainties in the simulation give raise to only small errors on the W mass measurement in the  $W^+W^- \rightarrow q\bar{q}\ell\bar{\nu}$  channel, the only non-negligible errors are caused by the uncertainty in the energy scale of the jet and lepton energies.

The systematic uncertainty caused by changes in the fit procedure are negligible or, in the case of the  $W^+W^- \rightarrow q\bar{q}\tau\bar{\nu}$  channel, small. Together with the small bias, the unity slope of the calibration function and the unity width of the pull distributions obtained from ensemble tests, it can be stated that the *Convolution method* offers a sound analysis approach for the determination of the mass of the W boson.

Systematic	qqe $\nu$ channel	qq $\mu\nu$ channel	qq $\tau\nu$ channel	qq $\ell\nu$ combined
Beam energy	<b>22</b> $\pm$ 1	<b>22</b> $\pm$ 1	<b>22</b> $\pm$ 1	<b>22</b> $\pm$ 1
Bias Correction	<b>15</b>	<b>19</b>	<b>22</b>	<b>11</b>
ISR	<b>11</b> $\pm$ 0	<b>11</b> $\pm$ 0	<b>11</b> $\pm$ 0	<b>11</b> $\pm$ 0
Jet energy scale	<b>12</b> $\pm$ 1	<b>17</b> $\pm$ 1	<b>23</b> $\pm$ 1	<b>16</b> $\pm$ 1
Jet energy resolution	-3 $\pm$ 1	-6 $\pm$ 1	-11 $\pm$ 1	6 $\pm$ 0
Jet angular resolution	3 $\pm$ 1	6 $\pm$ 1	7 $\pm$ 1	5 $\pm$ 1
Lepton energy scale	<b>20</b> $\pm$ 2	-24 $\pm$ 1	0 $\pm$ 0	<b>13</b> $\pm$ 1
Lepton energy resolution	1 $\pm$ 0	0 $\pm$ 1	0 $\pm$ 1	0 $\pm$ 1
Lepton angular resolution	0 $\pm$ 0	0 $\pm$ 0	-1 $\pm$ 1	0 $\pm$ 1
Hadronization	23 $\pm$ <b>51</b>	-47 $\pm$ 46	-11 $\pm$ <b>77</b>	9 $\pm$ <b>31</b>
4-fermion effects	-36 $\pm$ <b>43</b>	31 $\pm$ <b>42</b>	-12 $\pm$ <b>55</b>	19 $\pm$ <b>26</b>
Fit Procedure	-1 $\pm$ 1	-1 $\pm$ 1	-6 $\pm$ 0	3 $\pm$ 1
Background	-5 $\pm$ <b>28</b>	-1 $\pm$ <b>31</b>	4 $\pm$ <b>47</b>	2 $\pm$ <b>19</b>
Total	81	83	114	57

**Table 8.13:** Systematic uncertainties for  $M_W$  at the center-of-mass energy of  $\sqrt{s} = 183$  GeV. See text for the combined  $W^+W^- \rightarrow q\bar{q}\ell\nu$  systematic error calculation (only the absolute values are given for these uncertainties). The total error is the quadratic sum of the bold entries in each column. All entries are in MeV.

Systematic	qqe $\nu$ channel	qq $\mu\nu$ channel	qq $\tau\nu$ channel	qq $\ell\nu$ combined
Beam energy	<b>16</b> $\pm$ 1	<b>16</b> $\pm$ 1	<b>16</b> $\pm$ 1	<b>16</b> $\pm$ 1
Bias Correction	<b>22</b>	<b>22</b>	<b>24</b>	<b>13</b>
ISR	<b>1</b> $\pm$ 0	<b>1</b> $\pm$ 0	<b>1</b> $\pm$ 0	<b>1</b> $\pm$ 0
Jet energy scale	<b>1</b> $\pm$ 0	2 $\pm$ 1	2 $\pm$ 1	2 $\pm$ 0
Jet energy resolution	2 $\pm$ 0	4 $\pm$ 1	5 $\pm$ 1	4 $\pm$ 0
Jet angular resolution	-2 $\pm$ 0	-3 $\pm$ 0	-6 $\pm$ 1	3 $\pm$ 0
Lepton energy scale	<b>14</b> $\pm$ 1	<b>16</b> $\pm$ 1	0 $\pm$ 0	<b>9</b> $\pm$ 0
Lepton energy resolution	-2 $\pm$ 0	-1 $\pm$ 1	1 $\pm$ 0	1 $\pm$ 0
Lepton angular resolution	0 $\pm$ 0	0 $\pm$ 0	1 $\pm$ 1	0 $\pm$ 0
Hadronization	6 $\pm$ <b>17</b>	24 $\pm$ 17	7 $\pm$ <b>25</b>	2 $\pm$ <b>13</b>
4-fermion effects	-2 $\pm$ 0	0 $\pm$ 0	1 $\pm$ 1	1 $\pm$ 0
Fit Procedure	0 $\pm$ <b>1</b>	-1 $\pm$ 1	-6 $\pm$ 1	3 $\pm$ 0
Background	-5 $\pm$ <b>28</b>	1 $\pm$ <b>20</b>	6 $\pm$ <b>34</b>	2 $\pm$ <b>15</b>
Total	45	45	52	30

**Table 8.14:** Systematic uncertainties for  $M_W$  at the center-of-mass energy of  $\sqrt{s} = 189$  GeV. See text for the combined  $W^+W^- \rightarrow q\bar{q}\ell\nu$  systematic error calculation (only the absolute values are given for these uncertainties). The total error is the quadratic sum of the bold entries in each column. All entries are in MeV.





## Chapter 9

# Results and Discussion

In this chapter, the *Convolution method* is applied to the data collected with the OPAL detector in the years 1997 and 1998 at center-of-mass energies of  $\sqrt{s} = 183$  GeV and  $\sqrt{s} = 189$  GeV and a combined result on the mass of the W boson for these energies is obtained.

The *Convolution method* is then compared to two alternative approaches to determine the mass of the W boson within the OPAL collaboration, the *Reweighting method* and the *Breit-Wigner fit*.

The chapter closes with a comparison of the *Convolution method* with the results of the other LEP experiments and a review of the current status of the W mass measurement.

### 9.1 Results at $\sqrt{s} = 183$ GeV

The measurement of the mass of the W boson at a center-of-mass energy of  $\sqrt{s} = 183$  GeV is based on  $56.56 \pm 0.15(\text{stat.}) \pm 0.23(\text{sys.}) \text{ pb}^{-1}$  of data collected with the OPAL detector in the year 1997 [60]. The luminosity weighted mean center-of-mass energy of the data sample is  $182.69 \pm 0.05$  GeV [60].

The number of selected events used in the mass analysis is listed in table 9.1, together with the Monte Carlo expectation for the signal and the background. The number of data events and the expectations are in good agreement with each other.

The data of the three semileptonic decay channels,  $W^+W^- \rightarrow q\bar{q}e\bar{\nu}$ ,  $W^+W^- \rightarrow q\bar{q}\mu\bar{\nu}$ , and  $W^+W^- \rightarrow q\bar{q}\tau\bar{\nu}$  were fitted separately. The results from the maximum likelihood fits were corrected for residual bias using calibration functions as described in chapter 8.4. The calibration functions have slopes consistent with unity for all decay channels and the exhibit only small biases of the order of 50–90 MeV. The statistical error was scaled by the inverse slope of the calibration function and the pull width, compare chapter 8.5. The Monte Carlo samples that were used in the analysis to determine the calibration function, to estimate the statistical error and to obtain the systematic uncertainties are listed in appendix E and were generated, with a few exceptions, at a center-of-mass energy of  $\sqrt{s} = 183$  GeV.

Channel	Data events	Monte-Carlo expectation	
		Signal events	Background events
$W^+W^- \rightarrow q\bar{q}e\bar{\nu}$	120	111	3
$W^+W^- \rightarrow q\bar{q}\mu\bar{\nu}$	113	113	1
$W^+W^- \rightarrow q\bar{q}\tau\bar{\nu}$	96	98	12

**Table 9.1:** Number of selected data events at a center-of-mass energy of  $\sqrt{s} = 183$  GeV. For comparison the expected number of events from Monte Carlo is shown. The signal expectation is taken from a Monte Carlo sample with  $M_W = 80.33$  GeV, the background expectations from  $e^+e^- \rightarrow Z^0/\gamma \rightarrow q\bar{q}$ ,  $e^+e^- \rightarrow We\nu_e$  ( $M_W = 80.33$  GeV), and  $e^+e^- \rightarrow Z^0Z^0$  Monte Carlos.

Channel	Fitted Mass / GeV	Corrected Mass / GeV	Expected Error / GeV
$W^+W^- \rightarrow q\bar{q}e\bar{\nu}$	$80.237 \pm 0.246$	$80.306 \pm 0.258$	0.269
$W^+W^- \rightarrow q\bar{q}\mu\bar{\nu}$	$80.514 \pm 0.264$	$80.603 \pm 0.275$	0.284
$W^+W^- \rightarrow q\bar{q}\tau\bar{\nu}$	$80.323 \pm 0.447$	$80.388 \pm 0.459$	0.413

**Table 9.2:** Summary of the fit results for the data at  $\sqrt{s} = 183$  GeV and the expected errors of the measurement. All errors are statistical only.

Table 9.2 lists the results obtained from the maximum likelihood fit, the bias corrected results and the expected statistical error of the measurement. The applied bias corrections and the scaling factor for the statistical error as obtained from the inverse slope of the calibration function and the pull width are listed in table 9.3. The results of the three channels are consistent within the statistical errors and their precision agrees with the expectation.

The systematic uncertainties of each decay channel were evaluated and merged for the combined result as detailed in chapter 8.6, see table 8.13 on page 122 for a list of the individual systematic uncertainties.

In the  $W^+W^- \rightarrow q\bar{q}e\bar{\nu}$  channel we obtain a W boson mass of

$$M_W^{qqe\nu} = 80.306 \pm 0.258_{\text{stat}} \pm 0.081_{\text{sys}} \text{ GeV}, \quad (9.1)$$

in the  $W^+W^- \rightarrow q\bar{q}\mu\bar{\nu}$  channel a value of

$$M_W^{qq\mu\nu} = 80.603 \pm 0.275_{\text{stat}} \pm 0.083_{\text{sys}} \text{ GeV}, \quad (9.2)$$

is found and the  $W^+W^- \rightarrow q\bar{q}\tau\bar{\nu}$  channel yields

$$M_W^{qq\tau\nu} = 80.388 \pm 0.459_{\text{stat}} \pm 0.114_{\text{sys}} \text{ GeV}. \quad (9.3)$$



Channel	Bias correction / GeV	Scaling factor for stat. error
$W^+W^- \rightarrow q\bar{q}e\bar{\nu}$	$+0.069 \pm 0.015$	1.05
$W^+W^- \rightarrow q\bar{q}\mu\bar{\nu}$	$+0.090 \pm 0.019$	1.04
$W^+W^- \rightarrow q\bar{q}\tau\bar{\nu}$	$+0.055 \pm 0.022$	1.03

**Table 9.3:** Summary of the applied corrections to the fitted W mass at  $\sqrt{s} = 183 \text{ GeV}$ 

To facilitate the comparison with other measurements, which usually split the total error in statistical and systematic contributions, we use equation (8.24) to derive a combined result with the individual statistical and systematic errors. We obtain for  $M_W$  a value of

$$M_W = 80.437 \pm 0.174_{\text{stat}} \pm 0.057_{\text{sys}} \text{ GeV}. \quad (9.4)$$

The combined value for the W boson mass in the  $W^+W^- \rightarrow q\bar{q}\ell\bar{\nu}$  channel, taking into account the correlation of systematic uncertainties in the individual decay channels, is determined to

$$\boxed{M_W = 80.437 \pm 0.188 \text{ GeV}} \quad (9.5)$$

by applying equation (8.22).

Both combination methods give the same result for the W mass value, the total errors are within 4 MeV of each other.

Figure 9.1 summarizes the results for the W mass  $M_W$  as obtained with the *Convolution method* for the center-of-mass energy of  $\sqrt{s} = 183 \text{ GeV}$ . The points with error bars denote the measurements of  $M_W$  with the *Convolution method*, the solid line and the yellow (light grey) band mark the average value for  $M_W$  of all four LEP experiments and its error in the  $W^+W^- \rightarrow q\bar{q}\ell\bar{\nu}$  channel at this center-of-mass energy (including the results of the OPAL experiment as obtained with the *Reweighting technique*, compare section 9.4) [60–63]. The dotted lines show the average error of one LEP experiment. The results of the *Convolution method* are in good agreement with the LEP combination.

The results obtained with the *Convolution method* for the data collected with the OPAL detector at a center-of-mass energy of  $\sqrt{s} = 183 \text{ GeV}$  are consistent with each other, with the Standard Model expectations and other direct and indirect measurements of the mass of the W boson.

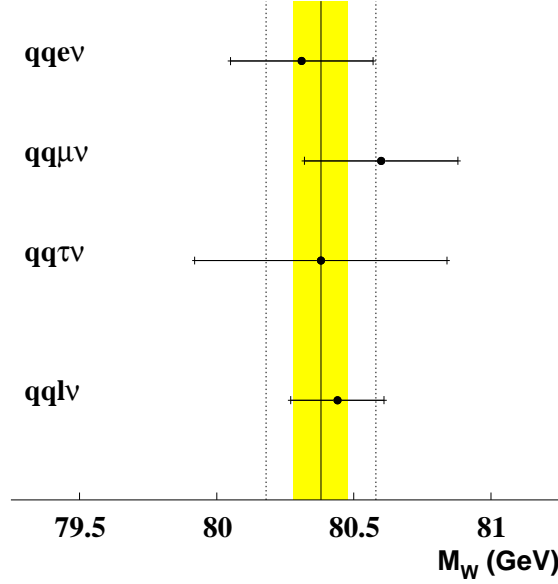


**Figure 9.1:** Summary of the results for  $M_W$  in the  $W^+W^- \rightarrow q\bar{q}\ell\bar{\nu}$  channel for the data collected with the OPAL detector at the center-of-mass energy of  $\sqrt{s} = 183$  GeV. The points denote the measurements with the *Convolution method*, the error bars show the statistical and total error of the measurements. The solid line marks the average result in the  $W^+W^- \rightarrow q\bar{q}\ell\bar{\nu}$  channel of the four LEP experiments for this energy [60–63], the yellow (light grey) band its total error. The dotted lines show the average error on  $M_W$  for one LEP experiment.

## 9.2 Results at $\sqrt{s} = 189$ GeV

The measurement of the mass of the W boson at a center-of-mass energy of  $\sqrt{s} = 189$  GeV is based on  $183.1 \pm 0.2(\text{stat.}) \pm 0.4(\text{sys.}) \text{ pb}^{-1}$  of data collected with the OPAL detector in the year 1998 [64]. The luminosity weighted mean center-of-mass energy of the data sample is  $188.625 \pm 0.040$  GeV [64].

Table 9.4 lists the number of events used in the mass analysis and the expectations for the number of signal and background events derived from Monte Carlo studies. The number of data events and the expectations are in good agreement with each other.

The data of the three semileptonic decay channels,  $W^+W^- \rightarrow q\bar{q}e\bar{\nu}$ ,  $W^+W^- \rightarrow q\bar{q}\mu\bar{\nu}$ , and  $W^+W^- \rightarrow q\bar{q}\tau\bar{\nu}$  were fitted separately. The results from the individual maximum likelihood fits were corrected for residual biases by applying

Channel	Data events	Monte-Carlo expectation	
		Signal events	Background events
$W^+W^- \rightarrow q\bar{q}e\bar{\nu}$	360	379	11
$W^+W^- \rightarrow q\bar{q}\mu\bar{\nu}$	370	375	4
$W^+W^- \rightarrow q\bar{q}\tau\bar{\nu}$	411	357	47

**Table 9.4:** Number of selected data events at a center-of-mass energy of  $\sqrt{s} = 189 \text{ GeV}$ . For comparison the expected number of events from Monte Carlo is shown. The signal expectation is taken from a Monte Carlo sample with  $M_W = 80.33 \text{ GeV}$  and includes the 4-fermion WW final state background, the background expectations from  $Z^0/\gamma$  and 4-fermion non-WW final states Monte Carlos.

Channel	Fitted Mass / GeV	Corrected Mass / GeV	Expected Error / GeV
$W^+W^- \rightarrow q\bar{q}e\bar{\nu}$	$80.187 \pm 0.164$	$80.128 \pm 0.167$	0.161
$W^+W^- \rightarrow q\bar{q}\mu\bar{\nu}$	$80.464 \pm 0.171$	$80.468 \pm 0.170$	0.154
$W^+W^- \rightarrow q\bar{q}\tau\bar{\nu}$	$80.624 \pm 0.223$	$80.656 \pm 0.220$	0.206

**Table 9.5:** Summary of the fit results for the data at  $\sqrt{s} = 189 \text{ GeV}$  and the expected errors of the measurement. All errors are statistical only.

the inverse calibration functions, as described in chapter 8.4. For all decay channels, the slopes of the calibration functions are consistent with unity within their statistical errors. The *Convolution method* exhibits only small biases in the range of 0–60 MeV. The statistical error returned by each fit was corrected by scaling it with the inverse slope of the calibration function and the pull width of the corresponding decay channel, see chapter 8.5 for further details. The Monte Carlo samples that were used in the analysis to obtain the calibration function, to estimate the statistical error and to determine the systematic uncertainties are listed in appendix E; they were generated, with a few exceptions, at a center-of-mass energy of  $\sqrt{s} = 188.634 \text{ GeV}$ .

Table 9.5 lists the results obtained from the maximum likelihood fit, the bias corrected results and the expected statistical error of the measurement. The applied bias corrections and the scaling factor for the statistical error as obtained from the inverse slope of the calibration function and the pull width are given in table 9.6. The results of the three channels are consistent within the statistical errors and their precision agrees with the expectation.

The systematic uncertainties of each decay channel were evaluated and merged for the combined result as detailed in chapter 8.6, compare table 8.14 on page 122 for a list of the individual systematic uncertainties.

In the  $W^+W^- \rightarrow q\bar{q}e\bar{\nu}$  channel we obtain a W boson mass of

$$M_W^{\text{qqe}\bar{\nu}} = 80.128 \pm 0.167_{\text{stat}} \pm 0.045_{\text{sys}} \text{ GeV}, \quad (9.6)$$

Channel	Bias correction / GeV	Scaling factor for stat. error
$W^+W^- \rightarrow q\bar{q}e\bar{\nu}$	$-0.059 \pm 0.022$	1.02
$W^+W^- \rightarrow q\bar{q}\mu\bar{\nu}$	$+0.004 \pm 0.022$	1.00
$W^+W^- \rightarrow q\bar{q}\tau\bar{\nu}$	$+0.032 \pm 0.024$	0.99

**Table 9.6:** Summary of the applied corrections to the fitted W mass at  $\sqrt{s} = 189$  GeV

in the  $W^+W^- \rightarrow q\bar{q}\mu\bar{\nu}$  channel a value of

$$M_W^{q\bar{q}\mu\bar{\nu}} = 80.468 \pm 0.170_{\text{stat}} \pm 0.045_{\text{sys}} \text{ GeV}, \quad (9.7)$$

is found and the  $W^+W^- \rightarrow q\bar{q}\tau\bar{\nu}$  channel yields

$$M_W^{q\bar{q}\tau\bar{\nu}} = 80.656 \pm 0.220_{\text{stat}} \pm 0.052_{\text{sys}} \text{ GeV}. \quad (9.8)$$

Using equation (8.24) the combined value of all three decay channels, with the error split into statistical and systematic contributions, is given by

$$M_W = 80.378 \pm 0.105_{\text{stat}} \pm 0.031_{\text{sys}} \text{ GeV}. \quad (9.9)$$

For the combined value for the W boson mass in the  $W^+W^- \rightarrow q\bar{q}\ell\bar{\nu}$  channel, taking into account the correlation of systematic uncertainties in the individual decay channels, we obtain

$$\boxed{M_W = 80.377 \pm 0.110 \text{ GeV}} \quad (9.10)$$

by applying equation (8.22).

Both combination methods give the same results within 1 MeV for both the value and its total error.

Figure 9.2 summarizes the results for the  $M_W$  as obtained with the *Convolution method* for the center-of-mass energy of  $\sqrt{s} = 189$  GeV. The points with error bars denote the measurements of  $M_W$  with the *Convolution method*, the solid line and the yellow (light grey) band mark the average value for  $M_W$  of all four LEP experiments and its error in the  $W^+W^- \rightarrow q\bar{q}\ell\bar{\nu}$  channel at this center-of-mass energy (including the results of the OPAL experiment as obtained with the *Reweighting technique*, compare section 9.4) [64–67]. The dotted lines shows the average error of one LEP experiment. The results of the *Convolution method* are in good agreement with the LEP combination.

The results obtained with the *Convolution method* for the data collected with the OPAL detector at a center-of-mass energy of  $\sqrt{s} = 189$  GeV are consistent with each other, with the Standard Model expectations and other direct and indirect measurements of the mass of the W boson.

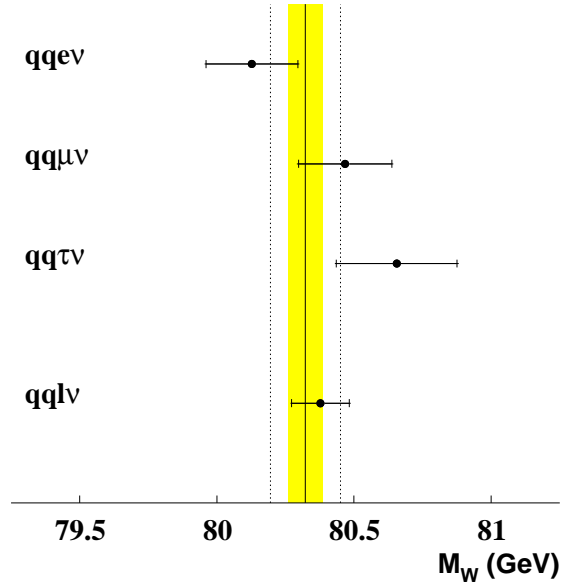


**Figure 9.2:** Summary of the results for  $M_W$  in the  $W^+W^- \rightarrow q\bar{q}\ell\bar{\nu}$  channel for the data collected with the OPAL detector at the center-of-mass energy of  $\sqrt{s} = 189$  GeV. The points with error bars denote the measurements with the *Convolution method*, the error bars show the statistical and total error of the measurements. The solid line marks the average result in the  $W^+W^- \rightarrow q\bar{q}\ell\bar{\nu}$  channel of the four LEP experiments for this energy [64–67], the yellow (light grey) band its total error. The dotted lines show the average error on  $M_W$  for one LEP experiment.

### 9.3 Combined Results

In this section the results obtained for the  $240 \text{ pb}^{-1}$  of data collected with the OPAL detector at center-of-mass energies of  $\sqrt{s} = 183$  GeV and  $\sqrt{s} = 189$  GeV are combined to yield a single value for the measurement of the mass of the W boson.

In combining the results for different center-of-mass energies, the systematic uncertainties for the beam energy, the *Initial State Radiation* modeling, the jet energy scale and resolutions, the hadronization and the fit procedure are treated as fully correlated, all other systematic uncertainties are treated as uncorrelated [55].

To allow the comparison with other measurements and their statistical and systematic errors, we first use equation (8.24) to derive the results with the total error split into the individual statistical and systematic errors.

In the  $W^+W^- \rightarrow q\bar{q}\ell\bar{\nu}$  channel we obtain with this method a W boson mass of

$$M_{\text{W}}^{\text{qq}\nu} = 80.180 \pm 0.140_{\text{stat}} \pm 0.047_{\text{sys}} \text{ GeV}, \quad (9.11)$$

in the  $W^+W^- \rightarrow q\bar{q}\mu\bar{\nu}$  channel a value of

$$M_{\text{W}}^{\text{qq}\mu\nu} = 80.505 \pm 0.145_{\text{stat}} \pm 0.048_{\text{sys}} \text{ GeV}, \quad (9.12)$$

is found and the  $W^+W^- \rightarrow q\bar{q}\tau\bar{\nu}$  channel yields

$$M_{\text{W}}^{\text{qq}\tau\nu} = 80.606 \pm 0.198_{\text{stat}} \pm 0.055_{\text{sys}} \text{ GeV}. \quad (9.13)$$

The combined value for  $M_{\text{W}}$  in the  $W^+W^- \rightarrow q\bar{q}\ell\bar{\nu}$  channel is determined to

$$M_{\text{W}} = 80.394 \pm 0.090_{\text{stat}} \pm 0.033_{\text{sys}} \text{ GeV}. \quad (9.14)$$

As can be seen, the statistical error still dominates the precision of the measurement of the mass of the W boson in the combination, thus justifying the approximate combination in a weighted average. The results obtained with the weighted average are in very good agreement with the combined results derived from equation (8.22), see below.

To properly take into account the correlations between the individual decay channels and between the measurements at the two center-of-mass energies, a combination based on equation (8.22) has to be performed.

In the  $W^+W^- \rightarrow q\bar{q}e\bar{\nu}$  channel we obtain a W boson mass of

$$\boxed{M_{\text{W}}^{\text{qq}\nu} = 80.179 \pm 0.147 \text{ GeV}}, \quad (9.15)$$

in the  $W^+W^- \rightarrow q\bar{q}\mu\bar{\nu}$  channel a value of

$$\boxed{M_{\text{W}}^{\text{qq}\mu\nu} = 80.504 \pm 0.152 \text{ GeV}}, \quad (9.16)$$

is found and the  $W^+W^- \rightarrow q\bar{q}\tau\bar{\nu}$  channel yields

$$\boxed{M_{\text{W}}^{\text{qq}\tau\nu} = 80.608 \pm 0.206 \text{ GeV}}. \quad (9.17)$$

The combined value for the W boson mass in the  $W^+W^- \rightarrow q\bar{q}\ell\bar{\nu}$  channel is determined to

$$\boxed{M_{\text{W}} = 80.391 \pm 0.098 \text{ GeV}}. \quad (9.18)$$

The results obtained with the *Convolution method* at the center-of-mass energies of  $\sqrt{s} = 183$  GeV and  $\sqrt{s} = 189$  GeV with the OPAL data are summarized in figure 9.3; the solid line and the yellow (light grey) band in this figure denote the average value for  $M_W$  of all four LEP experiments and its error in the  $W^+W^- \rightarrow q\bar{q}\ell\bar{\nu}$  channel for these center-of-mass energies (including the results of the OPAL experiment as obtained with the *Reweighting technique*, compare section 9.4) [68]. The results of the *Convolution method* are in good agreement with the LEP combination.

The combined results obtained with the *Convolution method* for the data collected with the OPAL detector at a center-of-mass energy of  $\sqrt{s} = 183$  GeV and  $\sqrt{s} = 189$  GeV are consistent with each other, with the Standard Model expectations and other direct and indirect measurements of the mass of the W boson.

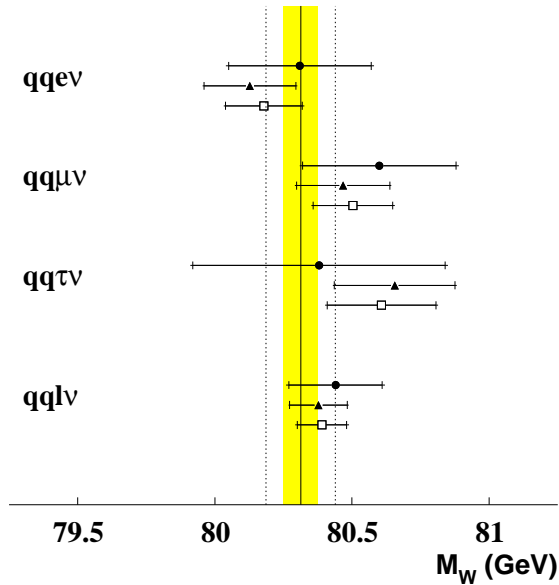


**Figure 9.3:** Summary of the results for  $M_W$  in the  $W^+W^- \rightarrow q\bar{q}\ell\bar{\nu}$  channel for the data collected with the OPAL detector at the center-of-mass energies of  $\sqrt{s} = 183$  GeV and  $\sqrt{s} = 189$  GeV as obtained with the *Convolution method*. The filled circles denote the results for the data at  $\sqrt{s} = 183$  GeV, the filled triangle for the data at  $\sqrt{s} = 189$  GeV, and the open rectangles show the combined results. The error bars show the statistical and total error of the measurements. The solid line marks the average result in the  $W^+W^- \rightarrow q\bar{q}\ell\bar{\nu}$  channel of the four LEP experiments for these energies [68], the yellow (light grey) band its total error. The dotted lines show the average error on  $M_W$  for one LEP experiment.

## 9.4 Comparison with Alternative Measurement Methods

In this section the performance of the *Convolution method* is compared to two alternative methods to determine the mass of the W boson within the OPAL collaboration, the *Reweighting method* and the *Breit-Wigner fit*. After a brief description of each alternative method, the expected statistical errors, the systematic uncertainties, the necessary bias corrections and the results obtained for the OPAL data at center-of-mass energies of  $\sqrt{s} = 183$  GeV and  $\sqrt{s} = 189$  GeV are compared.

### 9.4.1 The Reweighting Method

The *Reweighting method* [55, 69, 70] is based on the idea of a direct comparison between the reconstructed mass distribution of the data events with a simulated mass distribution derived from Monte Carlo.

An event-by-event reweighting technique is used to emulate the simulated mass spectrum from a few standard Monte Carlo samples, since the production of Monte Carlo samples at arbitrary values of  $M_W$  and  $\Gamma_W$ , as they are needed for a fit of the simulated spectrum to the data, is not feasible.

The mass of the W boson is extracted with a binned maximum likelihood fit, since there is no analytical description of the parent distribution. The maximum likelihood fit is carried out in four bins of the event mass error in the  $W^+W^- \rightarrow q\bar{q}\ell\bar{\nu}$  channel, thus including in a crude way the error information of the kinematic event reconstruction.

The *Reweighting method* should provide a bias free measurement of the W mass  $M_W$  and its width  $\Gamma_W$  as long as all important effects are properly included in the Monte Carlo generators.

### 9.4.2 The Breit-Wigner Fit

The *Breit-Wigner method* [71, 72] is the most straight forward method for the measurement of the mass of the W boson at OPAL. The expected mass spectrum is approximated by a Breit-Wigner distribution. The problem of the inclusion of ISR effects in the mass spectrum is solved by using different widths below and above the peak in the Breit-Wigner function; these widths are determined from Monte Carlo simulations of the expected mass distribution.

The mass of the W boson is extracted with an unbinned maximum likelihood fit to the mass distribution of the data sample. The *Breit-Wigner method* does not take into account the individual measurement errors of the data events and thus uses less information than the *Reweighting* and *Convolution methods*.

The *Breit-Wigner fit* provides a very simple and direct way to measure the mass of the W boson, but is expected to lead to relatively high biases—due to the simple treatment of ISR effects on the mass spectrum—and a slightly worse resolution—it disregards the errors of the individual W mass measurements in each event and thus does not use the full information available from the data sample.



Channel	Mean Number of Events		
	Signal	Background	Total
$W^+W^- \rightarrow q\bar{q}e\bar{\nu}$	111	3	114
$W^+W^- \rightarrow q\bar{q}\mu\bar{\nu}$	113	1	114
$W^+W^- \rightarrow q\bar{q}\tau\bar{\nu}$	98	12	110

**Table 9.7:** Mean number of events in a data-sized Monte Carlo subsample of  $57 \text{ pb}^{-1}$  at  $\sqrt{s} = 183 \text{ GeV}$  selected with the *Convolution method*.

Channel	Mean Number of Events		
	Signal	Background	Total
$W^+W^- \rightarrow q\bar{q}e\bar{\nu}$	379	11	390
$W^+W^- \rightarrow q\bar{q}\mu\bar{\nu}$	375	4	379
$W^+W^- \rightarrow q\bar{q}\tau\bar{\nu}$	357	47	404

**Table 9.8:** Mean number of events in a data-sized Monte Carlo subsample of  $183 \text{ pb}^{-1}$  at  $\sqrt{s} = 189 \text{ GeV}$  selected with the *Convolution method*.

### 9.4.3 Comparison of Results

This section provides a comparison of the three different methods, the *Reweighting method*, the *Breit-Wigner fit*, and the *Convolution method*, used to extract the mass  $M_W$  of the W boson from the data within the OPAL collaboration. The use of three independent and complementary methods to measure the W mass provides a valuable cross-check and allows to choose the method that yields the smallest error. In this comparison the results obtained in [60, 70] were used for the *Reweighting method* and those of [71, 72] for the *Breit-Wigner method*. The discussion will include the expected statistical errors, systematic errors, the bias corrections and the actual results obtained for the data at the center-of-mass energies of  $\sqrt{s} = 183 \text{ GeV}$  and  $\sqrt{s} = 189 \text{ GeV}$ .

#### Expected Statistical Errors

Unlike the presented analysis in this thesis (compare chapter 8.5), the other two methods determine the expected statistical error in a slightly different way: Instead of forming the ensemble subsamples with a fixed number of events—the number observed in the data—the Monte Carlo events are divided into samples of the integrated data luminosity. Thus the number of events in each subsamples is no longer fixed but is allowed to fluctuate around the mean value according to a Poisson distribution. To allow the direct comparison of the expected statistical errors, this scheme has also been applied to the *Convolution method*. Table 9.7 and table 9.8 list the mean numbers of signal and background events for a data-sized sample for the center-of-mass energies of  $\sqrt{s} = 183 \text{ GeV}$  and  $\sqrt{s} = 189 \text{ GeV}$ , respectively.

Channel	Method		
	Reweighting	Breit-Wigner	Convolution
$W^+W^- \rightarrow q\bar{q}e\bar{\nu}$	0.31	0.30	0.26
$W^+W^- \rightarrow q\bar{q}\mu\bar{\nu}$	0.30	0.33	0.27
$W^+W^- \rightarrow q\bar{q}\tau\bar{\nu}$	0.45	0.56	0.39
$W^+W^- \rightarrow q\bar{q}\ell\bar{\nu}$ comb.	0.19	0.21	0.17

**Table 9.9:** Comparison of the expected statistical errors of the three W mass extraction methods at OPAL for a data-sized sample of  $57 \text{ pb}^{-1}$  at a center-of-mass energy of  $\sqrt{s} = 183 \text{ GeV}$ . All entries are in GeV, the errors are smaller than  $0.005 \text{ GeV}$ . Values for the *Reweighting method* are taken from [60], for the *Breit-Wigner fit* from [71].

The expected statistical errors<sup>1</sup> for the W mass measurement at a center-of-mass energy of  $\sqrt{s} = 183 \text{ GeV}$  are listed in table 9.9. As for all analysis methods the slope of the calibration functions and the width of the pull distributions are consistent with unity, no correction factors were applied to the results of these ensemble tests.

The expected statistical error of the *Convolution method* in the  $W^+W^- \rightarrow q\bar{q}e\bar{\nu}$  channel is about 17% smaller than for the *Reweighting technique* and about 13% smaller than for the *Breit-Wigner fit*. In the  $W^+W^- \rightarrow q\bar{q}\mu\bar{\nu}$  channel the *Convolution method* yields an error that is about 9% smaller than the error of the *Reweighting method* and about 20% smaller than the error of the *Breit-Wigner fit*. The error of the *Convolution fit* in the  $W^+W^- \rightarrow q\bar{q}\tau\bar{\nu}$  channel is about 17% smaller than for the *Reweighting technique*, while the *Breit-Wigner fit* is outperformed by more than 45%. The combined expected statistical error for all three decay channels of the *Convolution method* is about 15% smaller than for the *Reweighting technique* and about 20% smaller than for the *Breit-Wigner fit*.

The expected statistical errors<sup>1</sup> for the W mass measurement at a center-of-mass energy of  $\sqrt{s} = 189 \text{ GeV}$  are listed in table 9.10. In the *Breit-Wigner fit*, the analysis of the  $W^+W^- \rightarrow q\bar{q}\tau\bar{\nu}$  channel is split in events with hadronic tau decays and events with leptonic tau decays, to improve the resolution. Only the combined error for the full  $W^+W^- \rightarrow q\bar{q}\tau\bar{\nu}$  channel is used in this comparison [72].

The expected statistical error of the *Convolution method* in the  $W^+W^- \rightarrow q\bar{q}e\bar{\nu}$  channel is about 8% smaller than for the *Reweighting technique* and about 14% smaller than for the *Breit-Wigner fit*. In the  $W^+W^- \rightarrow q\bar{q}\mu\bar{\nu}$  channel the *Convolution method* yields an error that is about 8% smaller than the error of the *Reweighting method* and about 10% smaller than the error of the *Breit-Wigner fit*. The error of the *Convolution fit* in the  $W^+W^- \rightarrow q\bar{q}\tau\bar{\nu}$  channel is about 3% smaller than for the *Reweighting technique* and about 7% smaller than for the *Breit-Wigner fit*. The

<sup>1</sup>The differences in the expected errors for the *Convolution method* compared to the values given in table 8.10 and table 8.11 in chapter 8.5 are due to the different mean number of events—in most cases the number of observed events in the data is smaller than the expected number of events—and the correction factors applied for the slope of the calibration functions and the pull width—which are in most cases larger than 1 for the *Convolution method*.

Channel	Method		
	Reweighting	Breit-Wigner	Convolution
$W^+W^- \rightarrow q\bar{q}e\bar{\nu}$	0.164	0.172	0.151
$W^+W^- \rightarrow q\bar{q}\mu\bar{\nu}$	0.168	0.170	0.155
$W^+W^- \rightarrow q\bar{q}\tau\bar{\nu}$	0.220	0.229	0.214
$W^+W^- \rightarrow q\bar{q}\ell\bar{\nu}$ comb.	0.104	0.107	0.097

**Table 9.10:** Comparison of the expected statistical errors of the three W mass extraction methods at OPAL for a data-sized sample of  $183 \text{ pb}^{-1}$  at a center-of-mass energy of  $\sqrt{s} = 189 \text{ GeV}$ . All entries are in GeV, the errors are smaller than  $0.005 \text{ GeV}$ . Values for the *Reweighting method* are taken from [70], for the *Breit-Wigner fit* from [72].

combined expected statistical error for all three decay channels of the *Convolution method* is about 7% smaller than for the *Reweighting technique* and about 10% smaller than for the *Breit-Wigner fit*.

The *Convolution method* with its inclusion of the single event error information leads to a better resolution in the measurement of the mass of the W boson. An overall improvement of the order of 10–20% on the expected statistical error in the  $W^+W^- \rightarrow q\bar{q}\ell\bar{\nu}$  channel over the two alternative methods, the *Reweighting technique* and the *Breit-Wigner fit*, is achieved. The improvement is enhanced for lower statistics in the data sample, as can be seen by comparing the results at the center-of-mass energy of  $\sqrt{s} = 183 \text{ GeV}$  with the results at a center-of-mass energy of  $\sqrt{s} = 189 \text{ GeV}$ , for which the data has approximately three times the integrated luminosity. The *Convolution method* yields consistently the best expected statistical errors for both center-of-mass energies and in all decay channels.

### Systematic Uncertainties

The resolution of the mass measurement is not only limited by the statistical error, but as well by systematic uncertainties. An improvement in the statistical precision could well be negated by increased systematic uncertainties. To properly compare the methods, it is therefore essential to combine the statistical and systematic errors to yield the total error. The comparison is limited to the combined results for the  $W^+W^- \rightarrow q\bar{q}\ell\bar{\nu}$  channel as no breakdown in the  $W^+W^- \rightarrow q\bar{q}e\bar{\nu}$ ,  $W^+W^- \rightarrow q\bar{q}\mu\bar{\nu}$  and  $W^+W^- \rightarrow q\bar{q}\tau\bar{\nu}$  channels is available for the *Reweighting method* and the *Breit-Wigner fit*.

Table 9.11 compares the systematic uncertainties for the center-of-mass energies of  $\sqrt{s} = 183 \text{ GeV}$  and  $\sqrt{s} = 189 \text{ GeV}$ . The systematic errors  $\delta_{\text{sys}}$  are combined with the expected statistical error  $\delta_{\text{stat}}$  as given in table 9.9 and table 9.10 to yield the total expected error  $\delta_{\text{total}}$  for the W mass measurement for each method,

$$\delta_{\text{total}} = \sqrt{\delta_{\text{stat}}^2 + \delta_{\text{sys}}^2}. \quad (9.19)$$

The systematic uncertainties are comparable for all three methods and the total

Method	$\sqrt{s} = 183 \text{ GeV}$		$\sqrt{s} = 189 \text{ GeV}$	
	Sys. Error	Tot. Error	Sys. Error	Tot. Error
Reweighting	0.06	0.20	0.031	0.109
Breit-Wigner	0.06	0.21	0.037	0.113
Convolution	0.06	0.18	0.030	0.101

**Table 9.11:** Systematic uncertainties and total expected error on the W mass of the three analysis methods at OPAL at center-of-mass energies of  $\sqrt{s} = 183 \text{ GeV}$  and  $\sqrt{s} = 189 \text{ GeV}$ . All entries are in GeV. Values for the *Reweighting method* are taken from [60, 70], for the *Breit-Wigner fit* from [71, 72].

error is dominated by the statistical error of the measurement. Therefore the *Convolution method* gives the smallest expected total error for the W mass measurement, about 10–20% better than the *Reweighting technique* and the *Breit-Wigner fit*.

### Bias Corrections

Another interesting point is the size of the bias corrections that have to be applied to a method to correct for shortcomings in the description and the underlying assumptions. The *Reweighting method* is supposed to be bias-free as long as the Monte Carlo simulation correctly incorporates all effects that could lead to deviations. The *Breit-Wigner fit* and the *Convolution method* are not expected to be bias-free, as explained for the *Convolution method* in chapter 8.4; similar arguments apply to the *Breit-Wigner fit*. The comparison of the bias corrections is limited to the *Breit-Wigner fit* and the *Convolution method*, as the reweighting technique was proven to be bias free [60, 64].

Table 9.12 and table 9.13 list the bias corrections that were applied to the data at the center-of-mass energies of  $\sqrt{s} = 183 \text{ GeV}$  and  $\sqrt{s} = 189 \text{ GeV}$ . As expected by the better modeling of the physics function compared to the *Breit-Wigner fit*, the *Convolution method* has much reduced bias corrections. This becomes most apparent in the  $W^+W^- \rightarrow q\bar{q}\tau\bar{\nu}$  channel where the background contribution is largest and the shape of the mass distribution deviates most from the simple Breit-Wigner form. But even in the  $W^+W^- \rightarrow q\bar{q}e\bar{\nu}$  and  $W^+W^- \rightarrow q\bar{q}\mu\bar{\nu}$  channels, the bias correction for the *Convolution method* is less than 1/2 or 1/3 than for the *Breit-Wigner method*.

### Results for Data at $\sqrt{s} = 183 \text{ GeV}$ and $\sqrt{s} = 189 \text{ GeV}$

As a last point of the comparison of the three methods to extract the W mass we focus our attention on the results of the actual measurements at the center-of-mass energies of  $\sqrt{s} = 183 \text{ GeV}$  and  $\sqrt{s} = 189 \text{ GeV}$ .

Table 9.14 lists the results for the  $57 \text{ pb}^{-1}$  of data collected with the OPAL detector at a center-of-mass energy of  $\sqrt{s} = 183 \text{ GeV}$ , only the uncorrected<sup>2</sup> statis-

<sup>2</sup>That is, the errors returned by the maximum likelihood fit. No correction for the slope of the

Channel	Method	
	Breit-Wigner	Convolution
$W^+W^- \rightarrow q\bar{q}e\bar{\nu}$	$-0.202 \pm 0.015$	$+0.069 \pm 0.015$
$W^+W^- \rightarrow q\bar{q}\mu\bar{\nu}$	$-0.233 \pm 0.015$	$+0.090 \pm 0.019$
$W^+W^- \rightarrow q\bar{q}\tau\bar{\nu}$	$-0.450 \pm 0.021$	$+0.055 \pm 0.022$

**Table 9.12:** Comparison of the applied bias corrections for the *Breit-Wigner fit* and the *Convolution method* at a center-of-mass energy of  $\sqrt{s} = 183$  GeV. All entries are in GeV. Values for the *Breit-Wigner fit* are taken from [71].

Channel	Method	
	Breit-Wigner	Convolution
$W^+W^- \rightarrow q\bar{q}e\bar{\nu}$	$-0.115 \pm 0.013$	$-0.059 \pm 0.022$
$W^+W^- \rightarrow q\bar{q}\mu\bar{\nu}$	$-0.168 \pm 0.013$	$+0.004 \pm 0.022$
$W^+W^- \rightarrow q\bar{q}\tau\bar{\nu}$	$-0.460 \pm 0.029^a$	$+0.032 \pm 0.024$
	$-0.350 \pm 0.024^b$	

<sup>a</sup>Hadronic tau decays

<sup>b</sup>Leptonic tau decays

**Table 9.13:** Comparison of the applied bias corrections for the *Breit-Wigner fit* and the *Convolution method* at a center-of-mass energy of  $\sqrt{s} = 189$  GeV. The bias corrections for the *Breit-Wigner fit* in the  $W^+W^- \rightarrow q\bar{q}\tau\bar{\nu}$  channel are given for the event classes with hadronic and leptonic tau decays. All entries are in GeV. Values for the *Breit-Wigner fit* are taken from [72].

tical errors are quoted. The results for the different methods are consistent within their errors. Contrary to the expectation, the *Convolution method* gives only a comparable error to the *Reweighting technique* on the measured W mass. While the errors for the *Convolution method* in the  $W^+W^- \rightarrow q\bar{q}e\bar{\nu}$  and  $W^+W^- \rightarrow q\bar{q}\mu\bar{\nu}$  channel match the expectations, the error in the  $W^+W^- \rightarrow q\bar{q}\tau\bar{\nu}$  channel for the data sample is much larger than expected. The *Reweighting technique*, on the other hand, gives in all three semileptonic decay channels much smaller errors for the data sample than expected, compare table 9.9. As expected, the precision of the *Breit-Wigner fit* is approximately 10–20% worse than the precision of the other two methods.

Table 9.15 lists the results for the  $183 \text{ pb}^{-1}$  of data collected with the OPAL detector at a center-of-mass energy of  $\sqrt{s} = 189$  GeV, only the uncorrected statistical errors are quoted. The precisions of the three measurements are comparable and match the expectations. The results of the three methods are consistent within their errors. As a further cross-check of the analysis methods at the center-of-mass energy of  $\sqrt{s} = 189$  GeV, a common ensemble test—using exactly the same subsamples—was performed for the publication [64]. The mean difference on the measured W mass between the extraction methods was found to be consistent with calibration function or the width of the pull distribution has been applied.

Channel	Method		
	Reweighting	Breit-Wigner	Convolution
$W^+W^- \rightarrow q\bar{q}e\bar{\nu}$	$80.23 \pm 0.24$	$80.21 \pm 0.27$	$80.31 \pm 0.25$
$W^+W^- \rightarrow q\bar{q}\mu\bar{\nu}$	$80.42 \pm 0.27$	$80.30 \pm 0.33$	$80.60 \pm 0.26$
$W^+W^- \rightarrow q\bar{q}\tau\bar{\nu}$	$80.40 \pm 0.40$	$80.36 \pm 0.52$	$80.38 \pm 0.45$
$W^+W^- \rightarrow q\bar{q}\ell\bar{\nu}$ comb.	$80.33 \pm 0.17$	$80.27 \pm 0.19$	$80.44 \pm 0.17$

**Table 9.14:** Comparison of the measured W mass of the three extraction methods for the data sample of  $57 \text{ pb}^{-1}$  at a center-of-mass energy of  $\sqrt{s} = 183 \text{ GeV}$ . Only the uncorrected statistical errors are given. All entries are in GeV. Values for the *Reweighting method* are taken from [60], for the *Breit-Wigner fit* from [71].

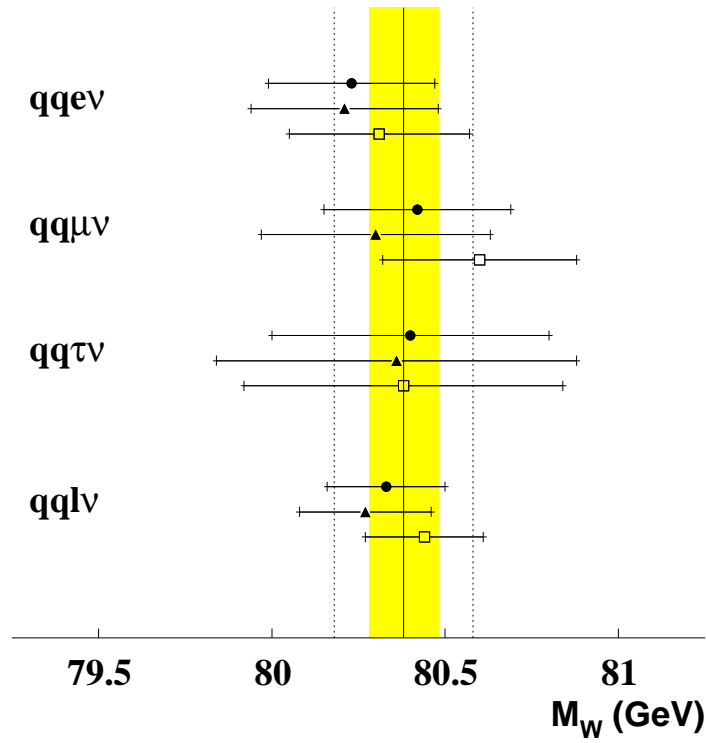
Channel	Method		
	Reweighting	Breit-Wigner	Convolution
$W^+W^- \rightarrow q\bar{q}e\bar{\nu}$	$80.375 \pm 0.175$	$80.286 \pm 0.164$	$80.128 \pm 0.164$
$W^+W^- \rightarrow q\bar{q}\mu\bar{\nu}$	$80.513 \pm 0.163$	$80.562 \pm 0.173$	$80.468 \pm 0.171$
$W^+W^- \rightarrow q\bar{q}\tau\bar{\nu}$	$80.594 \pm 0.227$	$80.672 \pm 0.240$	$80.656 \pm 0.223$
$W^+W^- \rightarrow q\bar{q}\ell\bar{\nu}$ comb.	$80.478 \pm 0.106$	$80.467 \pm 0.107$	$80.378 \pm 0.105$

**Table 9.15:** Comparison of the measured W mass of the three extraction methods for the data sample of  $183 \text{ pb}^{-1}$  at a center-of-mass energy of  $\sqrt{s} = 189 \text{ GeV}$ . Only the uncorrected statistical errors are given. All entries are in GeV. Values for the *Reweighting method* are taken from [70], for the *Breit-Wigner fit* from [72].

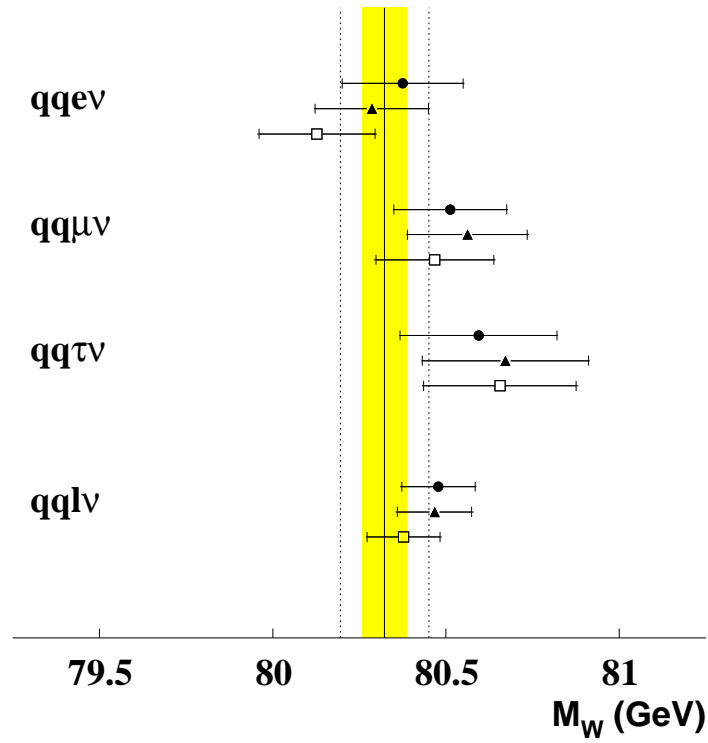
0 within the statistical error of 10–20 MeV in this ensemble test, the RMS spread was in the range of 60–90 MeV (with an error of about 10 MeV) for the  $W^+W^- \rightarrow q\bar{q}e\bar{\nu}$  and  $W^+W^- \rightarrow q\bar{q}\mu\bar{\nu}$  channels, and between 130–160 MeV (with an error of about 15 MeV) for the  $W^+W^- \rightarrow q\bar{q}\tau\bar{\nu}$  channel.

Figure 9.4 and figure 9.5 summarize the measurements of the W boson mass with the three extraction method for the center-of-mass energies of  $\sqrt{s} = 183 \text{ GeV}$  and  $\sqrt{s} = 189 \text{ GeV}$ , respectively. The filled circles denote the results obtained with the *Reweighting technique*, the filled triangles the results for the *Breit-Wigner fit* and the open rectangles the measurements using the *Convolution method*. The error bars show the statistical and total errors of the measurements. As a comparison, the solid line marks the average result of the four LEP experiments for the corresponding center-of-mass energy (including the results of the OPAL experiment as obtained with the *Reweighting technique*) [60–67], the yellow (lightgrey) band denotes its total error.

The analysis of the data recorded at the center-of-mass energies of  $\sqrt{s} = 183 \text{ GeV}$  and  $\sqrt{s} = 189 \text{ GeV}$  yielded consistent results for all three methods of the W mass determination. The precision of the measurements is comparable for all methods.



**Figure 9.4:** Comparison of the results for  $M_W$  in the  $W^+W^- \rightarrow q\bar{q}\ell\bar{\nu}$  channel for the data collected with the OPAL detector at the center-of-mass energy of  $\sqrt{s} = 183$  GeV for the three extraction methods. The full circles denote the measurements with the *Reweighting technique*, the full triangles the measurements with the *Breit-Wigner fit*, and the open squares the results obtained with the *Convolution method*. The error bars show the statistical and total error of the measurements. The solid line marks the average result of the four LEP experiments for these energies [60–63], the yellow (light grey) band its total error. The dotted lines show the average error on  $M_W$  for one LEP experiment.



**Figure 9.5:** Comparison of the results for  $M_W$  in the  $W^+W^- \rightarrow q\bar{q}\ell\bar{\nu}$  channel for the data collected with the OPAL detector at the center-of-mass energy of  $\sqrt{s} = 189$  GeV for the three extraction methods. The full circles denote the measurements with the *Reweighting technique*, the full triangles the measurements with the *Breit-Wigner fit*, and the open squares the results obtained with the *Convolution method*. The error bars show the statistical and total error of the measurements. The solid line marks the average result of the four LEP experiments for these energies [64–67], the yellow (light grey) band its total error. The dotted lines show the average error on  $M_W$  for one LEP experiment.



## 9.5 Comparison with the other LEP Experiments and the Current Status of the W Mass Measurement

This section provides a comparison of the results obtained with *Convolution method* at OPAL with the W mass measurements of the other three experiments, ALEPH, DELPHI, and L3. Also reviewed is the current status of the measurement of the mass of the W boson at LEP and its implications concerning the Standard Model.

Figure 9.6 and figure 9.7 show the comparison of the mass of the W boson determined with the *Convolution method* with the results of the four LEP experiments for the center-of-mass energies  $\sqrt{s} = 183$  GeV and  $\sqrt{s} = 189$  GeV in the  $W^+W^- \rightarrow q\bar{q}\ell\bar{\nu}$  channel [60–67].

Compared to the other three LEP experiments, the *Convolution method* performs very well. Only the ALEPH experiment reaches the precision of the W mass measurement achieved in the OPAL collaboration.

The current status of the W mass measurements is shown in figure 9.8. The combined result of the LEP experiments of the center-of-mass energies of  $\sqrt{s} = 161$ –202 GeV from the years 1996–1999 is the most precise measurement of the mass of the W boson up to date. The precision of the direct W mass measurements in  $p\bar{p}$  collision was already reached by the LEP experiments with the inclusion of the  $\sqrt{s} = 189$  GeV data in 1998. The figure also shows the W mass derived from indirect measurements, as e.g. the electroweak precision tests with the LEP1 data. The direct measurement of the W mass is in very good agreement with the Standard Model predictions, confirming the self-consistency of the theory.

Together with the measurement of mass of the top quark and results of direct searches, the mass of the W boson can be used to set constraints on the mass of the Higgs boson via electroweak radiative corrections. Figure 9.9 shows the current results of the direct and indirect measurements of the W boson and top mass [12]. The intersection of the confidence levels of these measurements with the yellow (light grey) band allows the derivation of limits on the Higgs boson mass. The lower limit of 113 GeV on the Higgs mass is set by (unsuccessful) direct searches. A marked improvement can be seen by comparing the current status with the status of 1997, as it was shown in figure 4.2 on page 35. Both, direct and indirect measurements favor a light Higgs boson with a mass lower than 1 TeV. The next generation accelerator, the LHC pp collider, with its center-of-mass energy of 14 TeV will open this mass range for direct searches in the year 2005 and will hopefully allow its two multipurpose experiments ATLAS and CMS to observe the Higgs boson.

## 9.6 Summary of Results

The results obtained with the *Convolution method* from the  $240 \text{ pb}^{-1}$  of OPAL data in the semileptonic decay channel,  $W^+W^- \rightarrow q\bar{q}\ell\bar{\nu}$ , at the center-of-mass energies

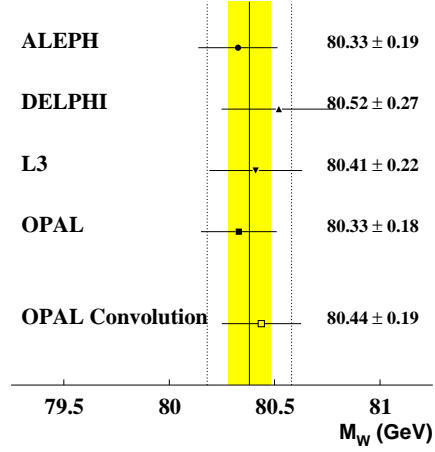


**Figure 9.6:** Comparison of the measurement of the mass of the W boson in the  $W^+W^- \rightarrow q\bar{q}\ell\bar{\nu}$  channel with the *Convolution method* with the results of the four LEP experiments at the center-of-mass energy of  $\sqrt{s} = 183$  GeV. The solid line denotes the average value of the W mass measurements of all four experiments [60–63], the yellow (light grey) band its error. The dotted lines show the average error on  $M_W$  for one LEP experiment.

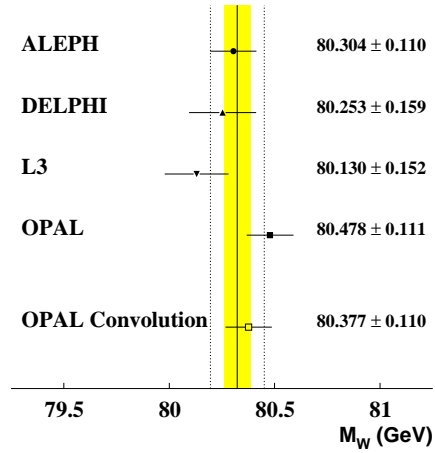


**Figure 9.7:** Comparison of the measurement of the mass of the W boson in the  $W^+W^- \rightarrow q\bar{q}\ell\bar{\nu}$  channel with the *Convolution method* with the results of the four LEP experiments at the center-of-mass energy of  $\sqrt{s} = 189$  GeV. The solid line denotes the average value of the W mass measurements of all four experiments [64–67], the yellow (light grey) band its error. The dotted lines show the average error on  $M_W$  for one LEP experiment.

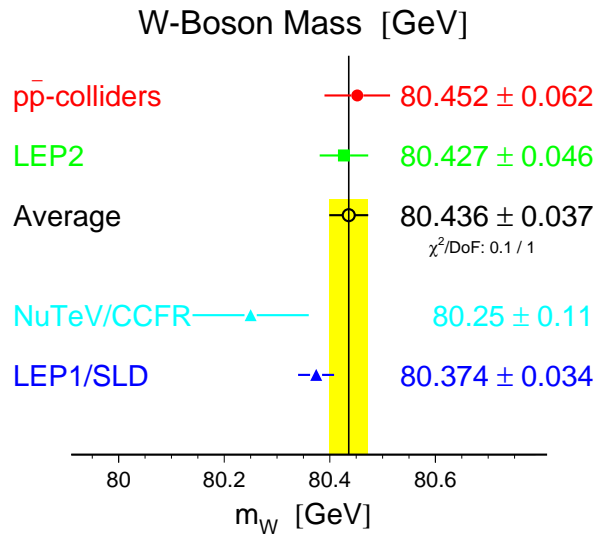


**Figure 9.8:** Comparison of the direct ( $p\bar{p}$  and LEP2) and indirect (NuTeV, LEP1/SLD) measurements of the mass of the W boson [12].

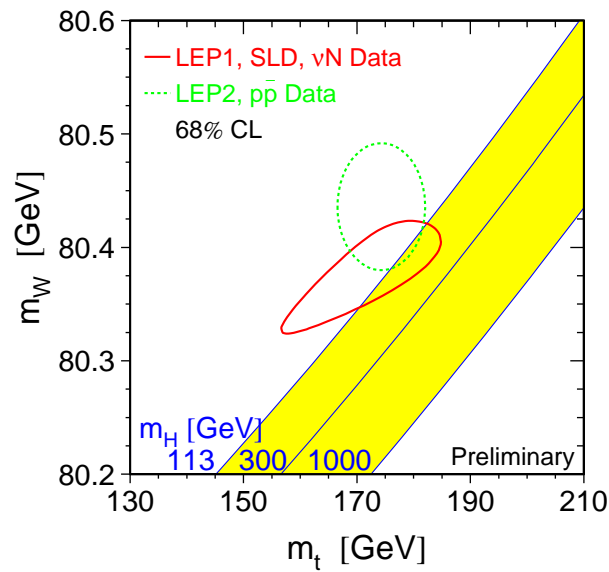


**Figure 9.9:** Comparison of the Standard Model predictions of the top and W masses with indirect and direct measurements [12]. The indirect measurements are obtained from a fit to electroweak precision data. The yellow (light grey) area shows the Standard Model prediction for a range of the Higgs mass (the lower bound is the current limit derived from direct searches).

of  $\sqrt{s} = 183$  GeV and  $\sqrt{s} = 189$  GeV were presented. The measurements are consistent with each other for all analyzed decay channels,  $W^+W^- \rightarrow q\bar{q}e\bar{\nu}$ ,  $W^+W^- \rightarrow q\bar{q}\mu\bar{\nu}$ , and  $W^+W^- \rightarrow q\bar{q}\tau\bar{\nu}$  and both center-of-mass energies. The precision of the actual measurement matches the expectations and is on par with other measurements of  $M_W$  within the OPAL collaboration and the other LEP experiments at these center-of-mass energies. The results agree well with other indirect and direct measurements of the mass of the W boson.

A comparison of the *Convolution method* with the two alternative methods to extract the W mass within the OPAL collaboration, the *Reweighting method* and the *Breit-Wigner fit*, was performed. Monte Carlo studies of the expected statistical error show an improvement in the precision of the W mass measurement by about 10% in favor of the *Convolution method*. The systematic uncertainties are comparable and consistent for all methods. Compared to the *Breit-Wigner fit*, the *Convolution method* has a much reduced bias correction due to the better modeling of the expected event W mass distribution. For the analyses of the data at center-of-mass energies of  $\sqrt{s} = 183$  GeV and  $\sqrt{s} = 189$  GeV all methods yield consistent results with comparable statistical precision and systematic uncertainties. This result provides an important cross-check for the measurement of the mass of the W boson within the OPAL experiment.





# Chapter 10

## Summary

In this thesis a new method to measure the mass of the  $W$  boson in the semileptonic decay channel,  $W^+W^- \rightarrow q\bar{q}\ell\bar{\nu}$ , at the OPAL experiment, the *Convolution method*, has been presented.

The semileptonic channel has the biggest influence on the measurement of the mass of the  $W$  boson, as systematic uncertainties of final state interactions like *Bose-Einstein Correlation* and *Color Reconnection*—which can bias the mass measurement in  $W^+W^- \rightarrow q\bar{q}q\bar{q}$  decays [21, 24]—do not exist in this channel. The measurement of the  $W$  boson mass in the  $W^+W^- \rightarrow \bar{\ell}\nu\ell\bar{\nu}$  channel [73, 74] provides a valuable cross-check, but has only negligible influence due to the low statistics in this channel and a corresponding large error on the measurement. The weight of the  $W^+W^- \rightarrow q\bar{q}\ell\bar{\nu}$  channel in the combined result of the  $W$  mass at OPAL at the center-of-mass energies of  $\sqrt{s} = 161\text{--}189$  GeV is about 65%, while the measurement in the  $W^+W^- \rightarrow q\bar{q}q\bar{q}$  channel has a weight of only 35%. With the inclusion of further data, collected in 1999 and 2000, the weight on the  $W$  mass of the measurement of the semileptonic channel will rise to about 80%.

The *Convolution method* extends and improves the analytical *Breit-Wigner fit* method already used within the collaboration. The mass of the  $W$  boson is determined with an unbinned maximum likelihood fit as in the *Breit-Wigner fit*.

In the *Convolution method*, the event likelihood is not simply given by the value of a Breit-Wigner function at the measured event  $W$  mass, but is calculated as the convolution of a physics function with an event probability density, thus including the precision of the  $W$  mass determination of the individual data points in the fit.

The physics function is based on the superposition of relativistic Breit-Wigner functions evaluated at different center-of-mass energies to take in account—for the first time in the underlying theoretical description of the expected data distribution—the effects of *Initial State Radiation* on the mass reconstruction in a kinematic fit on a statistical basis.

The event probability density assigns each  $W$  mass value a probability that a pair of  $W$  bosons with that mean mass generated this particular event. It is closely related to the measurement error, which can in fact be derived from it, and thus

allows to take into account the precision of the measurement of the mean W boson mass in each individual event in the W mass extraction fit. A kinematic fit is used to reconstruct the events and to obtain the event probability density.

The mass of the W boson is determined by a maximum likelihood fit to the data sample, assuming the Standard Model relation between the mass  $M_W$  and the width  $\Gamma_W$  of the W boson.

The *Convolution method* was applied to the data recorded with the OPAL detector at LEP at center-of-mass energies of  $\sqrt{s} = 183$  GeV and  $\sqrt{s} = 189$  GeV in the years 1997 and 1998. For the integrated luminosity of  $57 \text{ pb}^{-1}$  of data recorded at a center-of-mass energy of  $\sqrt{s} = 183$  GeV the mass of the W boson was measured to be

$$M_W = 80.437 \pm 0.188 \text{ GeV}.$$

For the integrated luminosity of  $183 \text{ pb}^{-1}$  of data recorded at a center-of-mass energy of  $\sqrt{s} = 189$  GeV a value of

$$M_W = 80.377 \pm 0.110 \text{ GeV}$$

was found. A combination of the results of both center-of-mass energies yielded

$$M_W = 80.391 \pm 0.098 \text{ GeV}.$$

The measured mass of the W boson is in agreement with Standard Model prediction, obtained from electroweak precision tests, and other direct measurements.

Compared to the two alternative methods, the *Reweighting technique* and the *Breit-Wigner fit*, used to extract the W mass within the OPAL collaboration the *Convolution method* has several advantages. The better modeling of the expected event W mass distribution by the inclusion of *Initial State Radiation* effects in the physics function makes the use of constant widths determined from Monte Carlo as in the *Breit-Wigner fit* unnecessary and leads to a reduction of the bias corrections. The *Convolution method* exhibits only a small residual bias of less than 100 MeV, much smaller than the statistical error of the measurements in the individual decay channels. The inclusion of the single event error information in the maximum likelihood fit improves the precision of the W mass measurement by 10–20% compared to the other methods, as determined from the expected statistical error obtained from Monte Carlo ensemble tests. The systematic uncertainties of all three methods are comparable. Thus, the *Convolution method* offers the best expected precision for the measurement of the W boson mass in the semileptonic channel in OPAL.

The success of the *Convolution method* in the semileptonic channel,  $W^+W^- \rightarrow q\bar{q}\ell\bar{\nu}$ , has spurred more effort in the inclusion of individual event errors for the measurement of the W mass. The *Reweighting technique* is now carried out in bins of the fit error, but still does not reach the precision of the *Convolution method*. A two-dimensional convolution method, albeit using only Gaussian event probability



densities and similar to the method developed in [62], is applied in the  $W^+W^- \rightarrow q\bar{q}q\bar{q}$  channel [75] and a fast approximative reconstruction of  $W^+W^- \rightarrow q\bar{q}\ell\bar{\nu}$  events will allow a two-dimensional convolution in the semileptonic channel as well [76].

For the current published results of the OPAL collaboration on the mass of the W boson, the *Convolution method* is used as a cross-check of the more tested *Reweighting technique* [64, 77], but the advantage of the improved precision on the W mass measurement of the convolution methods in the  $W^+W^- \rightarrow q\bar{q}\ell\bar{\nu}$  and  $W^+W^- \rightarrow q\bar{q}q\bar{q}$  channels has been recognized [64].

The analysis efforts concerning the precision measurements of the mass of the W boson will not stop with the end of the data taking and the dismantling of the LEP accelerator and its experiments at the end of the year 2000. The four LEP experiments will still have to choose the best analysis method and will have to combine their results.

Together with the precise determination of the parameters of the Z boson, the measurement of the mass of the W boson will be a major result of the LEP program.



## Appendix A

# Performance of the Evil Tau Rejection

In this appendix, the performance of the *Evil tau rejection* [44] is estimated from its application to Monte Carlo samples, and the improvement of the expected statistical error for the mass measurement in the  $W^+W^- \rightarrow q\bar{q}\tau\bar{\nu}$  channel is derived. The *Evil tau rejection* can be applied to data collected at a center-of-mass energy of  $\sqrt{s} = 189$  GeV.

The likelihood selection of the *Evil tau rejection* tries to improve the identification of the best lepton candidate in  $W^+W^- \rightarrow q\bar{q}\tau\bar{\nu}$  events in which the tau lepton further decays into hadrons,  $W \rightarrow \tau\nu_\tau \rightarrow h(n\pi^0)\nu_\tau\nu_\tau$  and  $W \rightarrow \tau\nu_\tau \rightarrow 3h(n\pi^0)\nu_\tau\nu_\tau$ . In these event classes, the hadrons from the tau decay can intermix with the hadrons of the two jets belonging to the other W boson, and the standard event selection can associate the wrong tracks with the lepton, rendering the event useless for the determination of the W boson mass.

To estimate the efficiency of the *Evil tau rejection*, a comparison was made between the events of a Monte Carlo sample to which the *Evil tau rejection* was applied and the events of the same Monte Carlo sample without any *Evil tau rejection*. Reconstructed tau leptons for which the track angle deviates more than  $15^\circ$  from direction of the true tau lepton were defined as *Evil taus*.

In approximately 22% of the events with hadronic tau decays the standard event selection mis-identifies the best lepton candidate. The *Evil tau rejection* routine recuperates 27% of these bad events, while it mistakenly transforms only 3% of the good events to evil ones. The overall increase of good events is 3.5%.

To estimate the expected statistical error, an ensemble test was performed as described in chapter 8.3. The same Monte Carlo signal sample was used once without the application of the *Evil tau rejection* routine and once after it had been applied. In each case the appropriate background shape for the *Evil tau* background was used in the physics function, the four-fermion and the  $Z^0/\gamma$  backgrounds were included as usual. Figure A.1 shows the mass and pull distributions for the ensemble test for the uncorrected ensemble (upper plots) and the ensemble in which the

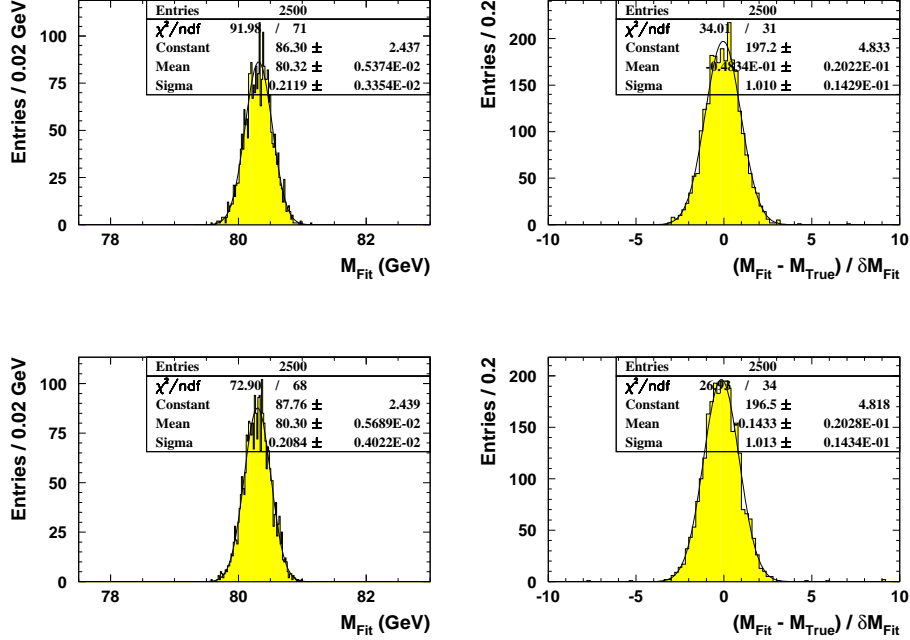


**Figure A.1:** Mass (left) and pull (right) distributions for the ensemble tests to estimate the improvement of the expected statistical error by applying the *Evil tau rejection*. The upper plots shows the distributions for the uncorrected ensemble, the lower plots for the ensemble to which the *Evil tau rejection* was applied.

	Exp. error / GeV	Pull width
Evil tau rejection not applied	$0.212 \pm 0.003$	$1.01 \pm 0.01$
Evil tau rejection applied	$0.208 \pm 0.004$	$1.01 \pm 0.01$
Difference	$0.004 \pm 0.001$	

**Table A.1:** Expected statistical errors and pull widths for the ensemble test performed to estimate the influence of the *Evil tau rejection* on the expected statistical error of the measurement of the W mass in the  $W^+W^- \rightarrow q\bar{q}\tau\bar{\nu}$  channel. The error on the difference between the expected errors for the ensemble with and without applied *Evil tau rejection* takes into account the almost full correlation between the samples of the two ensembles.

*Evil tau rejection* was applied (lower plots), the results for the widths of these distributions are listed in table A.1. The widths of the pull distributions are consistent with unity showing that the error estimates of the individual samples are correct in both methods. The improvement of the expected statistical error is given by the difference of the widths of the mass distributions with and without applied *Evil tau rejection*. It should be noted that the corresponding samples in the ensembles are built of the exactly the same events; thus they are almost fully correlated, which is

taken into account in the calculation of the error on the difference of the expected errors.

The *Evil tau rejection* improves the expected statistical error of the measurement of the W boson mass in the  $W^+W^- \rightarrow q\bar{q}\tau\bar{\nu}$  channel by approximately 2%.



## Appendix B

# Influence of the Penalty Factors on the Event Probability Density

As mentioned in chapter 8.2.1, the interpretation of equation (8.4),

$$P_i(m) = \frac{1}{N} \exp\left(-\frac{\chi_i^2(m) - \chi_i^2(m_i)}{2}\right),$$

as a probability density is only valid if the normalization constant  $N$ , as defined in equation (8.5),

$$N = \int_{-\infty}^{\infty} \exp\left(-\frac{\chi_i^2(m) - \chi_i^2(m_i)}{2}\right) dm,$$

cancels out the dependence on the penalty factors  $\delta_E$  and  $\delta_m$  for the energy and equal mass constraint which were used in equation (8.3),

$$\chi^2(m) = \min_{\hat{\mathbf{p}}} \left( \sum_{i,j} (\mathbf{p} - \hat{\mathbf{p}})_i G_{ij} (\mathbf{p} - \hat{\mathbf{p}})_j + \frac{(\sum_i E_i - \sqrt{s})^2}{\delta_E^2} + \frac{(m_{12} - m)^2}{\delta_m^2} + \frac{(m_{34} - m)^2}{\delta_m^2} \right),$$

to calculate the value of  $\chi^2(m)$ .

To investigate the influence of the penalty factors on the event probability density, the probabilities for a Monte Carlo sample were calculated twice: once with the default penalty factors and once with the weight of the penalty factors in the  $\chi^2$ -function increased by a factor of 10. For each event, the event probability densities are compared in the mass range which corresponds to a  $\Delta\chi^2 < 9$ , in steps of 0.5 GeV using a linear interpolation between the calculated  $\chi^2$  values.

Since the  $W^+W^- \rightarrow q\bar{q}\tau\bar{\nu}$  channel uses a less stringent penalty factor for the equal mass constraint to ensure a flat fit probability and the matching of the results with the standard kinematic fit as implemented in the WW analysis framework [37], the comparison is carried out separately for the  $W^+W^- \rightarrow q\bar{q}e\bar{\nu}$  and  $W^+W^- \rightarrow q\bar{q}\mu\bar{\nu}$  channels and the  $W^+W^- \rightarrow q\bar{q}\tau\bar{\nu}$  channel.

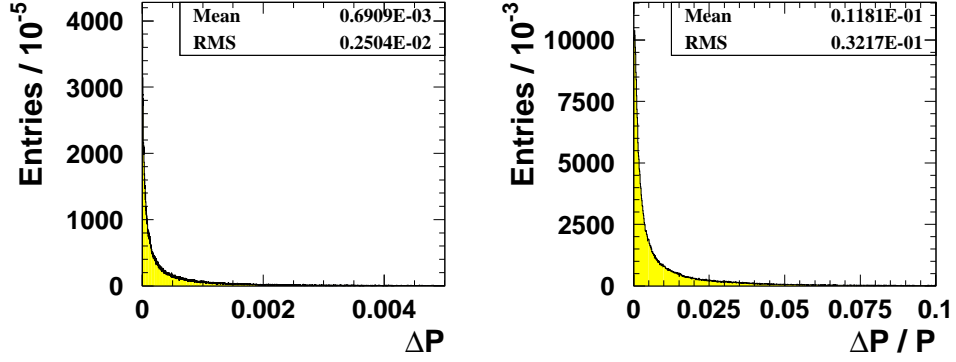


**Figure B.1:** Left: Absolute difference of the event probability values obtained with the default weights of the energy and equal mass constraint in equation (8.3) and the weights increased by a factor 10 for  $W^+W^- \rightarrow q\bar{q}e\bar{\nu}$  and  $W^+W^- \rightarrow q\bar{q}\mu\bar{\nu}$  events at  $\sqrt{s} = 189$  GeV. Right: Relative difference of the same probability values.

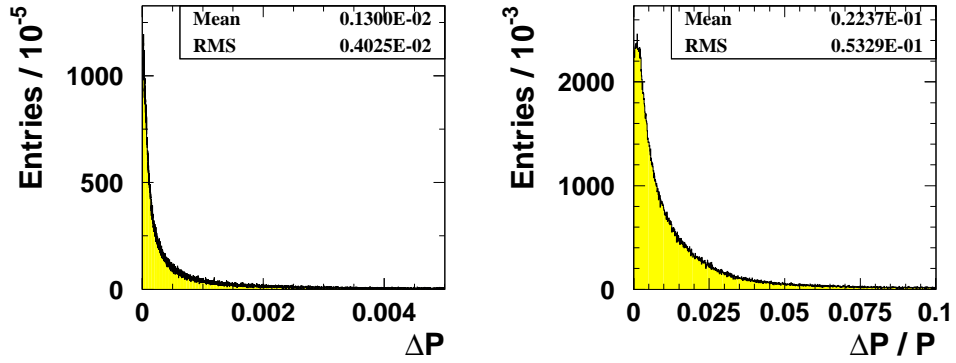


**Figure B.2:** Left: Absolute difference of the event probability values obtained with the default weights of the energy and equal mass constraint in equation (8.3) and the weights increased by a factor 10 for  $W^+W^- \rightarrow q\bar{q}\tau\bar{\nu}$  events at  $\sqrt{s} = 189$  GeV. Right: Relative difference of the same probability values.

The left side of figure B.1 and figure B.2 show the difference in the absolute value of the event probability density in the range  $\Delta\chi^2 < 9$ . In the  $W^+W^- \rightarrow q\bar{q}e\bar{\nu}$  and  $W^+W^- \rightarrow q\bar{q}\mu\bar{\nu}$  channels the mean value is smaller than 0.1% and the



RMS spread smaller than 0.3%, in the  $W^+W^- \rightarrow q\bar{q}\tau\bar{\nu}$  channel these values are increased by a factor of one and a half. The right side of figure B.1 and figure B.2 show the difference in the relative value, i.e. the absolute difference divided by the mean value of the event probability density in the range  $\Delta\chi^2 < 9$ . In the  $W^+W^- \rightarrow q\bar{q}e\bar{\nu}$  and  $W^+W^- \rightarrow q\bar{q}\mu\bar{\nu}$  channels the mean value is smaller than 1.5% and the RMS spread smaller than 3.5%, in the  $W^+W^- \rightarrow q\bar{q}\tau\bar{\nu}$  channel these values are again increased by a factor of about one and a half.

Despite the large increase in the weight of the constraints in the  $\chi^2$ -function, the event probability density remains almost unchanged for all decay channels.

To take into account possible effects of the penalty factors on the W mass measurement, a systematic error is assigned from the results of an ensemble test—carried out at both center-of-mass energies,  $\sqrt{s} = 183$  GeV and  $\sqrt{s} = 189$  GeV—with the *increased weight sample* and the *default* sample. In the  $W^+W^- \rightarrow q\bar{q}e\bar{\nu}$  and  $W^+W^- \rightarrow q\bar{q}\mu\bar{\nu}$  channels, the increased weight has only negligible influence on the determination of the W mass, only a shift of less than 2 MeV was observed. The  $W^+W^- \rightarrow q\bar{q}\tau\bar{\nu}$  channel is—as expected from the less stringent default penalty factor—more sensitive to the weight of the constraint terms. Here a shift of 17 MeV was observed, which is still negligible compared to the statistical errors of the mass measurements in this channel of approximately 400 MeV and 200 MeV at  $\sqrt{s} = 183$  GeV and  $\sqrt{s} = 189$  GeV, respectively.

The increased weights in the penalty functions lead to a notable deviation of the fitted mean event mass from the value of the kinematic fit implemented in the WW analysis framework and to a non-uniform distribution of the fit probability. Therefore, the obtained mass shifts are taken as an upper limit and systematic uncertainties of 1 MeV and 6 MeV were assigned in the  $W^+W^- \rightarrow q\bar{q}e\bar{\nu}/W^+W^- \rightarrow q\bar{q}\mu\bar{\nu}$  and  $W^+W^- \rightarrow q\bar{q}\tau\bar{\nu}$  channels, respectively.



## Appendix C

# Correlation between Scaled Hadronic Mass and Fitted Mass

The scaled hadronic mass, as described in chapter 7.3.1, is used as an approximation of the fitted mass in several intuitive reasonings in this thesis. In contrast to the results of a kinematic fit, the scaled hadronic mass can be easily calculated analytically and yields a simple result. This simplicity can be exploited to gain insights in the expected behavior of the reconstructed mass of the W boson in each event if parameters, e.g. the jet energies or the beam energy, are changed.

The approximation of the 2C/1C fitted mass<sup>1</sup> by the scaled hadronic mass is of course only a valid approach if both are highly correlated. Figure C.1 shows the fitted mass versus the scaled hadronic mass for  $W^+W^- \rightarrow q\bar{q}\ell\bar{\nu}$  Monte Carlo events at the center-of-mass energies of  $\sqrt{s} = 183$  GeV and  $\sqrt{s} = 189$  GeV. A high correlation can be readily observed.

To quantify the correlation between the scaled hadronic mass and the fitted mass the correlation coefficient  $\rho$  can be calculated as

$$\rho = \sum_{i=1}^N \frac{(M_{\text{Fit},i} - \langle M_{\text{Fit}} \rangle)(M_{\text{Scaled},i} - \langle M_{\text{Scaled}} \rangle)}{\sigma(M_{\text{Fit}}) \sigma(M_{\text{Scaled}})}, \quad (\text{C.1})$$

where  $N$  denotes the number of events,  $M_{\text{Fit},i}$  the 2C/1C fitted mass of the  $i$ -th event,  $M_{\text{Scaled},i}$  the scaled hadronic mass,  $\langle M_{\text{Fit}} \rangle$  the mean fitted mass of all events,  $\langle M_{\text{Scaled}} \rangle$  the mean scaled hadronic mass of all events,  $\sigma(M_{\text{Fit}})$  the standard deviation of the fitted mass and  $\sigma(M_{\text{Scaled}})$  the standard deviation of the scaled hadronic mass.

From the main Monte Carlo samples at  $\sqrt{s} = 183$  GeV and  $\sqrt{s} = 189$  GeV (compare appendix E), we obtain values of

$$\rho(\sqrt{s} = 183 \text{ GeV}) = 0.88 \quad (\text{C.2})$$

---

<sup>1</sup>The kinematic fit with energy-momentum conservation and an equal mass constraint is referred to as a 2C fit for  $W^+W^- \rightarrow q\bar{q}\ell\bar{\nu}$  and  $W^+W^- \rightarrow q\bar{q}\mu\bar{\nu}$  events, and as a 1C fit for  $W^+W^- \rightarrow q\bar{q}\tau\bar{\nu}$  events as the number of constraints that are not used to determine unobserved parameters are 2 or 1, respectively.

and

$$\rho(\sqrt{s} = 189 \text{ GeV}) = 0.90. \quad (\text{C.3})$$

The events used in this calculation were required to have a fit probability—as defined in equation (7.11)—greater than 0.05. This cut ensures that only properly fitted events are used in the comparison.

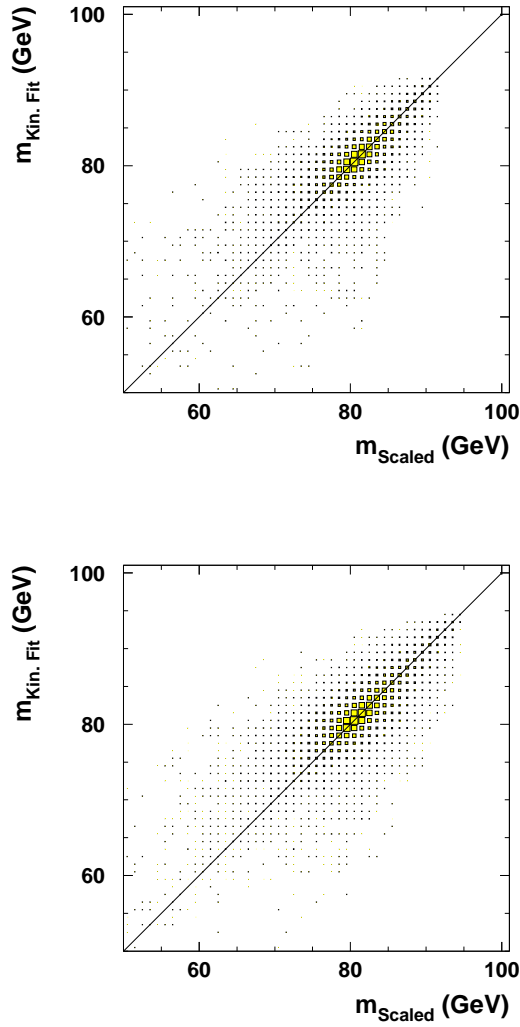


**Figure C.1:** 2C/1C fitted mass versus scaled hadronic mass for Monte Carlo events at center-of-mass energies of  $\sqrt{s} = 183 \text{ GeV}$  (upper plot) and  $\sqrt{s} = 189 \text{ GeV}$  (lower plot). The size of the squares is proportional to the number of entries in the bin. The solid line marks  $m_{\text{Scaled}} = m_{\text{Kin. Fit}}$ .





## Appendix D

# Expected Acceptance of the Data Quality Cuts

This appendix describes in detail the calculation of the expected acceptances of the data quality cuts.

The acceptance  $\alpha$  is defined as the ratio of the events  $n$  after the cut has been applied to the number of events  $N$  before the cut,

$$\alpha = \frac{n}{N}. \quad (\text{D.1})$$

The expected acceptances are determined for all three semileptonic decay channels,  $W^+W^- \rightarrow q\bar{q}e\bar{\nu}$ ,  $W^+W^- \rightarrow q\bar{q}\mu\bar{\nu}$ , and  $W^+W^- \rightarrow q\bar{q}\tau\bar{\nu}$ , independently for the signal and the backgrounds.

The total expected acceptance  $\alpha_{\text{tot}}$  is given by the weighted average of the signal acceptance  $\alpha_{\text{sig}}$  and the background acceptances  $\alpha_{\text{bg},i}$ ,

$$\alpha_{\text{tot}} = \alpha_{\text{sig}} \frac{N_{\text{sig}}}{N_{\text{sig}} + \sum_i N_{\text{bg},i}} + \sum_i \alpha_{\text{bg},i} \frac{N_{\text{bg},i}}{N_{\text{sig}} + \sum_i N_{\text{bg},i}}, \quad (\text{D.2})$$

where  $N_{\text{sig}}$  denotes the expected number of signal events and  $N_{\text{bg},i}$  the expected number of background events of the  $i$ -th background source before the cut is applied.

The error of the total acceptance can be calculated by a straight-forward application of the laws of error propagation, using Poisson statistics for the errors on the number of events, equation (D.1) to substitute the acceptances and keeping in mind that the number of events  $n$  after the cut and the number of events  $N$  before the cut are correlated. The correlation coefficient  $\rho$  between the number of events after and before the cut is given by their ratio,

$$\rho = \alpha = \frac{n}{N}. \quad (\text{D.3})$$

Table D.1 lists the expected acceptances of the data quality cuts for the signal and background at a center-of-mass energy of  $\sqrt{s} = 183$  GeV, table D.2 the expected acceptances at a center-of-mass energy of  $\sqrt{s} = 189$  GeV.

Channel		Fit-Prob.	Cut	
			$\Delta\chi^2 > 25$	$\chi^2$ smoothness
$W^+W^- \rightarrow q\bar{q}e\bar{\nu}$	Signal	$95.3 \pm 0.3\%$	$99.6 \pm 0.1\%$	$99.5 \pm 0.1\%$
	Bg. 1	$85.1 \pm 3.1\%$	$99.0 \pm 1.0\%$	$98.5 \pm 1.2\%$
	Bg. 2	$82.5 \pm 3.3\%$	100%	100%
	Bg. 3	$68.2 \pm 13.1\%$	100%	100%
	<b>Total</b>	<b><math>94.9 \pm 0.3\%</math></b>	<b><math>99.6 \pm 0.1\%</math></b>	<b><math>99.2 \pm 0.1\%</math></b>
$W^+W^- \rightarrow q\bar{q}\mu\bar{\nu}$	Signal	$95.4 \pm 0.3\%$	$99.6 \pm 0.1\%$	$99.8 \pm 0.1\%$
	Bg. 1	$45.8 \pm 6.3\%$	100%	100%
	Bg. 2	$29.4 \pm 13.0\%$	100%	100%
	Bg. 3	$50.0 \pm 7.4\%$	$94.4 \pm 5.3\%$	100%
	<b>Total</b>	<b><math>94.7 \pm 0.3\%</math></b>	<b><math>99.6 \pm 0.1\%</math></b>	<b><math>99.8 \pm 0.1\%</math></b>
$W^+W^- \rightarrow q\bar{q}\tau\bar{\nu}$	Signal	$90.3 \pm 0.4\%$	$99.6 \pm 0.1\%$	$99.7 \pm 0.1\%$
	Bg. 1	$70.3 \pm 2.1\%$	$98.0 \pm 0.8\%$	$99.3 \pm 0.5\%$
	Bg. 2	$85.7 \pm 1.5\%$	$99.6 \pm 0.3\%$	100%
	Bg. 3	$70.4 \pm 3.4\%$	$99.1 \pm 0.9\%$	$99.2 \pm 0.6\%$
	<b>Total</b>	<b><math>88.1 \pm 0.4\%</math></b>	<b><math>99.5 \pm 0.1\%</math></b>	<b><math>99.4 \pm 0.1\%</math></b>

**Table D.1:** Acceptance of the consecutive data quality cuts for signal and background events at  $\sqrt{s} = 183$  GeV as determined from Monte Carlo. The signal Monte Carlo includes only the CC03 diagrams, Bg. 1 denotes the  $e^+e^- \rightarrow Z^0/\gamma \rightarrow q\bar{q}$  background, Bg. 2 the  $e^+e^- \rightarrow W\nu_e$  background, and Bg. 3 the  $e^+e^- \rightarrow Z^0Z^0$  background. The total acceptance is calculated as the weighted average of the signal and background acceptances.

Channel		Fit-Prob.	Cut	
			$\Delta\chi^2 > 25$	$\chi^2$ smoothness
$W^+W^- \rightarrow q\bar{q}e\bar{\nu}$	Signal	$92.9 \pm 0.2\%$	$99.7 \pm 0.1\%$	$99.5 \pm 0.1\%$
	Bg. 1	$76.9 \pm 3.7\%$	100%	$99.4 \pm 0.8\%$
	Bg. 2	$69.1 \pm 3.1\%$	100%	$99.6 \pm 0.5\%$
	<b>Total</b>	<b><math>92.2 \pm 0.2\%</math></b>	<b><math>99.7 \pm 0.1\%</math></b>	<b><math>99.5 \pm 0.1\%</math></b>
	$W^+W^- \rightarrow q\bar{q}\mu\bar{\nu}$	Signal	$94.5 \pm 0.2\%$	$99.7 \pm 0.1\%$
Bg. 1		$59.0 \pm 7.2\%$	$97.8 \pm 3.0\%$	$97.8 \pm 3.1\%$
Bg. 2		$57.5 \pm 3.9\%$	$99.3 \pm 0.9\%$	100%
<b>Total</b>		<b><math>93.9 \pm 0.2\%</math></b>	<b><math>99.7 \pm 0.1\%</math></b>	<b><math>99.9 \pm 0.1\%</math></b>
$W^+W^- \rightarrow q\bar{q}\tau\bar{\nu}$		Signal	$92.4 \pm 0.2\%$	$99.8 \pm 0.1\%$
	Bg. 1	$74.1 \pm 1.8\%$	$99.0 \pm 0.5\%$	$99.5 \pm 0.4\%$
	Bg. 2	$81.1 \pm 1.4\%$	$99.6 \pm 0.3\%$	$99.7 \pm 0.2\%$
	<b>Total</b>	<b><math>90.3 \pm 0.3\%</math></b>	<b><math>99.6 \pm 0.1\%</math></b>	<b><math>99.8 \pm 0.1\%</math></b>

**Table D.2:** Acceptance of the consecutive data quality cuts for signal and background events at  $\sqrt{s} = 189$  GeV as determined from Monte Carlo. The signal Monte Carlo includes the four-fermion WW final states background, Bg. 1 denotes the  $e^+e^- \rightarrow Z^0/\gamma \rightarrow q\bar{q}$  background, Bg. 2 the non-WW final states background. The total acceptance is calculated as the weighted average of the signal and background acceptances.







## Appendix E

# Monte Carlo Samples

This appendix lists in detail the Monte Carlo samples that were used to obtain the calibration functions, the expected errors and the systematic uncertainties in the presented analysis of the OPAL data at center-of-mass energies of  $\sqrt{s} = 183$  GeV and  $\sqrt{s} = 189$  GeV.

### E.1 Monte Carlo Samples at $\sqrt{s} = 183$ GeV

Background	Run number	Generator info	$\sqrt{s}$ / GeV
$Z^0/\gamma$	5050	PYTHIA	183.000
$Z^0Z^0$	7338	PYTHIA	183.000
$W\nu_e$	7631	PYTHIA	183.000

**Table E.1:** Monte-Carlo samples used as background in the analysis at the center-of-mass energy of  $\sqrt{s} = 183$  GeV.

Run number	Generator info	$M_W$ / GeV	$\Gamma_W$ / GeV	$\sqrt{s}$ / GeV
7324	KORALW/JETSET	79.33	2.0544	183.000
7325	KORALW/JETSET	79.83	2.0738	183.000
<b>7323</b>	KORALW/JETSET	80.33	2.0933	183.000
7326	KORALW/JETSET	80.83	2.1129	183.000
7327	KORALW/JETSET	81.33	2.1326	183.000

**Table E.2:** Monte-Carlo signal samples used to determine the calibration functions at the center-of-mass energy of  $\sqrt{s} = 183$  GeV. The main signal sample is marked in boldface. For background samples compare table E.1.

Sytematic	Run number	Generator info	$M_W$ / GeV	$\Gamma_W$ / GeV	$\sqrt{s}$ / GeV
Beam energy	7323	KORALW/JETSET	80.33	2.0933	183.000
ISR	7323	KORALW/JETSET, $\mathcal{O}(\alpha^2)$ ISR	80.33	2.0933	183.000
	7667	KORALW/JETSET, $\mathcal{O}(\alpha^1)$ ISR	80.33	2.0933	183.000
Detector calib.	7323	KORALW/JETSET	80.33	2.0933	183.000
Fragmentation	7325	KORALW/JETSET	80.33	2.0933	184.000
	5033	HERWIG	80.33	2.086	184.000
4-f interference	8057	grc4f CC03 diag.	80.33	2.0933	183.00
	8056	grc4f 4f diag. except eeqq	80.33	2.0933	183.00
	7055	grc4f eeqq diag.	80.33	2.0933	183.00
Fit Procedure	7323	KORALW/JETSET	80.33	2.0933	183.000
Background	7323	KORALW/JETSET	80.33	2.0933	183.000
	7631	PYTHIA	80.33	2.0933	183.000
	7338	PYTHIA	—	—	183.000
	5050	PYTHIA	—	—	183.000

**Table E.3:** Monte-Carlo samples used for systematic studies in the analysis at the center-of-mass energy of  $\sqrt{s} = 183$  GeV.

## E.2 Monte Carlo Samples at $\sqrt{s} = 189$ GeV

Background	Run number	Generator info	$\sqrt{s}$ / GeV
$Z^0/\gamma$	5111	PYTHIA	189.000
4f (non- $W^+W^-$ final states)	9323	KORALW/JETSET + grc4f	188.634
4f ( $W^+W^-$ final states)	9300	KORALW/JETSET + grc4f	188.634
$W\nu_e$	8963	KORALW/JETSET + grc4f	189.000

**Table E.4:** Monte-Carlo samples used as background in the analysis at the center-of-mass energy of  $\sqrt{s} = 189$  GeV.

Run number	Generator info	$M_W$ / GeV	$\Gamma_W$ / GeV	$\sqrt{s}$ / GeV
9298	KORALW/JETSET + grc4f	79.83	2.0544	188.634
9299	KORALW/JETSET + grc4f	80.08	2.0738	188.634
<b>9300</b>	KORALW/JETSET + grc4f	80.33	2.0933	188.634
9301	KORALW/JETSET + grc4f	80.58	2.1129	188.634
9302	KORALW/JETSET + grc4f	80.83	2.1326	188.634

**Table E.5:** Monte-Carlo signal samples used to determine the calibration functions at the center-of-mass energy of  $\sqrt{s} = 189$  GeV. The main signal sample is marked in boldface. For background samples compare table E.4.

Sytematic	Run number	Generator info	$M_W$ / GeV	$\Gamma_W$ / GeV	$\sqrt{s}$ / GeV
Beam energy	9300	KORALW/JETSET + grc4f	80.33	2.0933	188.634
ISR	9300	KORALW/JETSET + grc4f	80.33	2.0933	188.634
Detector calib.	9300	KORALW/JETSET + grc4f	80.33	2.0933	188.634
Fragmentation	8438	KORALW/JETSET	80.33	2.086	189.000
	8442	HERWIG	80.33	2.086	189.000
	9865	KORALW/JETSET	80.33	2.086	189.000
	9866	HERWIG	80.33	2.086	189.000
4-f interference	9300	KORALW/JETSET + grc4f	80.33	2.0933	188.634
Fit Procedure	9300	KORALW/JETSET + grc4f	80.33	2.0933	188.634
Background	9300	KORALW/JETSET + grc4f	80.33	2.0933	188.634
	9323	KORALW/JETSET + grc4f	80.33	2.0933	188.634
	5111	PYTHIA	—	—	189.000

**Table E.6:** Monte-Carlo samples used for systematic studies in the analysis at the center-of-mass energy of  $\sqrt{s} = 189$  GeV.



# Bibliography

- [1] The ALEPH Collaboration. *Nucl. Instr. Meth.*, A(294):121, 1990.
- [2] The DELPHI Collaboration. *Nucl. Instr. Meth.*, A(303):233, 1991.
- [3] The L3 Collaboration. *Nucl. Instr. Meth.*, A(289):35, 1990.
- [4] The OPAL Collaboration. *Nucl. Instr. Meth.*, A(305):275–319, 1991.
- [5] The ATLAS Collaboration. ATLAS Technical Proposal. CERN/LHCC 94-43, CERN, 1994.
- [6] The CMS Collaboration. CMS Technical Proposal. CERN/LHCC 94-38, CERN, 1994.
- [7] W. Blum and L. Rolandi. *Particle Detection with Drift Chambers*. Springer Verlag, 1993.
- [8] ALEPH, DELPHI, OPAL, and L3 Collaborations. Searches for Higgs bosons: Preliminary combined results using LEP data collected at energies up to 209 GeV. Submitted to ICHEP'2000.
- [9] UA1 Collaboration. *Zeit. Phys.*, C(44):15, 1989.
- [10] UA2 Collaboration. *Phys. Lett.*, B(276):534, 1992.
- [11] G. Altarelli, T. Sjöstrand, and F. Zwirner Eds. Physics at LEP2. CERN 96-01, CERN, 1996. Volume 1.
- [12] *XXXth International Conference on High Energy Physics*, 2000.
- [13] *Recontres de Moriond*, 1997.
- [14] The LEP Collaborations ALEPH, DELPHI, L3, OPAL and the LEP W Working Group. Combined Preliminary Results on the Mass and Width of the W Boson Measured by the LEP Experiments. LEPEWWG/MASS 2000-01, CERN, 2000.
- [15] C. Caso et al. *Eur. Phys. J.*, C(15):1, 2000.

- [16] The OPAL Collaboration. *Eur. Phys. J.*, C(8):191–215, 1999.
- [17] The OPAL Collaboration. Measurement of Single W Production and Triple Gauge Boson Couplings in  $e^+e^-$  Collisions at  $\sqrt{s} = 189$  GeV. OPAL Physics NOTE PN427, CERN, 2000.
- [18] The OPAL Collaboration.  $W^+W^-$  Production Cross Section and W Branching Fractions in  $e^+e^-$  Collisions at 189 GeV. CERN-EP 2000-101, CERN, 2000. Submitted to *Phys. Lett. B*.
- [19] D. Bardini. GENTLE/4fan v. 2.0: A Program for the Semi-Analytical Calculation of Predictions for the Processes  $e^+e^- \rightarrow 4f$ . DESY 96-233, hep-ph/9612409, DESY, 1996.
- [20] J. Schiek. *Bose-Einstein Correlations in  $e^+e^- \rightarrow W^+W^-$  events at 172, 183 and 189 GeV*. PhD thesis, Ruprecht-Karls-University Heidelberg, 1999.
- [21] O. Sahr. PhD thesis, Ludwig-Maximilians-Universität München. In preparation.
- [22] The OPAL Collaboration. *Eur. Phys. J.*, C(8):559–571, 1999.
- [23] T. Sjöstrand and V.A. Khoze. *Zeit. Phys.*, C(62):281, 1994.
- [24] The OPAL Collaboration. Colour reconnection studies in  $e^+e^- \rightarrow W^+W^-$  at  $\sqrt{s} = 189$  GeV using inter-jet multiplicity. OPAL Physics Note PN448, CERN, 2000.
- [25] T. Christiansen. Influence of 5-Jet Events on the Measurement of the mass of the W Boson in  $e^+e^-$  Collisions. Diploma thesis, Ludwig-Maximilians-Universität München, 2000.
- [26] G. Altarelli, T. Sjöstrand, and F. Zwirner Eds. *Physics at LEP2*. CERN 96-01, CERN, 1996. Volume 2.
- [27] J. Allison et al. *Nucl. Instr. Meth.*, A(317):47, 1992.
- [28] R. Brun. GEANT 3 Users Guide. CERN/DD/EE 84-1, CERN, 1984.
- [29] S. Jadach, W. Placzek, M. Skrzypek, B.F.L. Ward, and Z. Wa. Monte Carlo program KORALW 1.42 for All Four-Fermion Final States in  $e^+e^-$  Collision. CERN-TH 98-242, CERN, 1998.
- [30] J. Fujimoto, T. Ishikawa, T. Kaneko, K. Kato, S. Kawabata, Y. Kurihara, T. Munehisa, D. Perret-Gallix, Y. Shimizu, and H. Tanaka. *Comp. Phys. Comm.*, (100):74, 1997.
- [31] F.A. Berends, R. Pittau, and R. Kleiss. *Comp. Phys. Comm.*, (85):437–452, 1995.



- [32] T. Sjöstrand. *Comp. Phys. Comm.*, (82):74, 1994.
- [33] G. Marchesini, B.R. Webber, G. Abbiendi, I.G. Knowles, M.H. Seymour, and L. Stanco. *Comp. Phys. Comm.*, (67):465, 1992.
- [34] L. Lönnblad. *Comp. Phys. Comm.*, (71):15, 1992.
- [35] S. Jadach, Z. Was, and J.H. Kuehn. *Comp. Phys. Comm.*, (64):275, 1991.
- [36] C. Hawkes, D. Lellouch, M. Redmond, O. Schaile, and M. Schröder. ROPE410. OPAL-Offline Note 16/OFFL-0487, CERN, 1996.
- [37] C.P. Ward, D.R. Ward, and N.K. Watson et al. Program WW112. [Web page] <http://opal.web.cern.ch/opal/manuals/ww/dev/ww.html>. Last access: November 2000.
- [38] G. Wilson. Further Improvements to an Event Selection for Events with Two Charged Leptons and Missing Energy. OPAL Technical Note TNxxx, CERN, 2000. Draft 0.11, March 2000.
- [39] M.A. Thomson. The OPAL  $W^+W^- \rightarrow q\bar{q}\ell\bar{\nu}$  Event Selection. Opal Technical Note TN635, CERN, 2000.
- [40] E. Torrence.  $W^+W^- \rightarrow qqqq$  Event Selection at 189 GeV. OPAL Technical Note TN650, CERN, 2000.
- [41] The OPAL Collaboration. Colour reconnection studies in  $e^+e^- \rightarrow W^+W^-$  at  $\sqrt{s} = 189$  GeV. OPAL Physics NOTE PN417, CERN, 1999.
- [42] E. Duchovni, D. Lellouch, G. Mikenberg, and T. Wlodek. GCE++ An Algorithm for Event Energy Measurement. OPAL Technical Note TN306, CERN, 1995.
- [43] N. Brown and W.J. Stirling. *Phys. Lett.*, B(252):657, 1990.
- [44] A. Frey. Subroutine WVEVLT.
- [45] T. Omori, S. Asai, I. Nakamura, and S. Yamashita. A Matching Algorithm: MT package. OPAL Technical Note TN381, CERN, 1996.
- [46] T. Omori, S. Asai, and I. Nakamura. Attempt to Compensate Energy in OPAL Calorimeter Complex based on MT Package. OPAL Technical Note TN447, CERN, 1996.
- [47] S. Mihara and S. Yamashita. MT 3.00 a new algorithm to calculate energy flow based on MT package. OPAL Technical Note TN575, CERN, 1998.
- [48] D.R. Ward. Subroutine WWFIX. [Web page] <http://opalinfo.cern.ch/opal/group/ww/WmassWorkPage/drw/wwfix.html>. Last access: November 2000.

- [49] C. Caso et al. *Eur. Phys. J.*, C(3):1, 1998.
- [50] C. Hartmann. *Die Messung der Masse und Breite des W-Bosons und die Suche nach anomalen Drei-Boson-Kopplungen bei LEP II mit OPAL*. Bonn-ir-97-20, Bonn University, 1997. In German.
- [51] A. G. Frodesen, O. Skjeggstad, and H. Tøfte. *Probability and Statistics in Particle Physics*. Universitetsforlaget, 1979.
- [52] F. James. MINUIT Reference Manual. CERN Program Library Long Wrieteup D506, CERN, 1994.
- [53] J. Dubbert. W mass determination in the  $W^+W^- \rightarrow q\bar{q}\ell\bar{\nu}$  channel using a convolution method. OPAL Technical Note TN641, CERN, 2000.
- [54] R. Barlow. *Statistics*. John Wiley & Sons, 1989.
- [55] R.L. Coxe. *Measurement of the Mass and the Width of the W Boson with the OPAL detector at LEP*. PhD thesis, University of Chicago, 2000.
- [56] R. Barlow. Recycling Data Using MC Bootstrap. MAN/HEP 99/4, University of Manchester, 2000.
- [57] A. Blondel et al. *Eur. Phys. J.*, C(11):573, 1998.
- [58] LEP Energy Working Group. Evaluation of the LEP centre-of-mass energy for data taken in 1998. CERN 99-01, CERN, 1999.
- [59] The OPAL Collaboration. Measurement of the W Boson Mass and the  $W^+W^-$  Production Cross Section in  $e^+e^-$  Collisions at 183 GeV. OPAL Physics Note PN331, CERN, 1998.
- [60] The OPAL Collaboration. *Phys. Lett.*, B(453):138, 1999.
- [61] ALEPH Collaboration. *Phys. Lett.*, B(453):121, 1999.
- [62] DELPHI Collaboration. *Phys. Lett.*, B(462):410, 1999.
- [63] L3 Collaboration. *Phys. Lett.*, B(454):386, 1999.
- [64] The OPAL Collaboration. Measurement of the Mass and Width of the W Boson in  $e^+e^-$  Collisions at 189 GeV. CERN-EP 2000-099, CERN, 2000. Submitted to *Phys. Lett. B*.
- [65] The ALEPH Collaboration. Measurement of the W Mass and Width in  $e^+e^-$  Collisions at 189 GeV. CERN-EP 2000-45, CERN, 2000. Submitted to *Eur. Phys. J.*
- [66] D. Bloch et al. Measurement of the mass and width of the W Boson in  $e^+e^-$  Collisions at  $\sqrt{s} = 189$  GeV. DELPHI 2000-144, CONF 443, CERN, 2000. Contributed paper for ICHEP2000.

- [67] L3 Collaboration. Preliminary Results on the Measurement of Mass and Width of the W Boson at LEP. L3 Note 2575, CERN, 2000. Submitted to ICHEP2000.
- [68] The LEP Collaboration ALEPH, DELPHI, L3, OPAL, The LEP Electroweak Working Group, and the SLD Heavy Flavour and Electroweak Working Groups. A Combination of Preliminary Electroweak Measurements and Constraints on the Standard Model. CERN-EP 2000-016, CERN, 2000.
- [69] C. Burgard and C. Hartmann. Measurement of the Mass and the Width of the W Boson Using a Reweighting Method. OPAL Technical Note TN468, CERN, 1997.
- [70] R.L. Coxe. Measurement of the Mass and the Width of the W Boson at  $\sqrt{s} = 189$  GeV with the Reweighting Method. OPAL Technical Note TN639, CERN, 2000.
- [71] C.P. Ward and D.R. Ward. Measurement of the Mass of the W Boson at 183 GeV using an analytic Breit-Wigner fit. OPAL Technical Note TN564, CERN, 1998.
- [72] C.G. Littlewood, C.P. Ward, and D.R. Ward. Measurement of the Mass of the W Boson at 189 GeV using an analytic Breit-Wigner fit. OPAL Technical Note TN658, CERN, 2000.
- [73] The OPAL Collaboration. Determination of the W Mass in the Fully Leptonic Channel. OPAL Physics Note PN447, CERN, 2000.
- [74] P. Méndez Lorenzo. PhD thesis, Ludwig-Maximilians-Universität München. In preparation.
- [75] E. Barberio, R. Ströhmer, and N. Watson. Measurement of the mass of the W boson with  $WW \rightarrow qq\bar{q}q$  events at 189 GeV using a convolution fit. OPAL Technical Note TN644, CERN, 2000.
- [76] M.A. Thomson. Approximating the Kinematic Fit in  $W^+W^- \rightarrow qq\bar{q}v_\ell$  Events at LEP. Opal Technical Note TN656, CERN, 2000.
- [77] J. Dubbert. Measurement of the W mass in the  $W^+W^- \rightarrow q\bar{q}\ell\bar{\nu}$  channel at  $\sqrt{s} = 189$  GeV using a convolution method. OPAL Technical Note TN642, CERN, 2000.



# Acknowledgments

I think I should thank first of all the members of the OPAL collaboration for keeping the detector going smoothly and all the people involved at running the accelerators at CERN. Without these people there would be no data to analyze . . .

Special thanks go to the members of the OPAL WW working group for providing the software on which this analysis was built.

This thesis would not exist in its current version without comments provided by my supervisor Prof. Dorothee Schaile. Thank you.

My former *Diplomvater*, Prof. Martin Faessler, did not hesitate to say “yes” when I asked him to be my second referee—despite numerous other commitments he already had. Thank you very much.

I would also like to thank the other members of our group in Munich for ideas and comments on numerous talks given during the last few years.

Several people invested a lot of time to provide ideas, corrections, or did the much needed proofreading of this work: Tim Christiansen, Christian Dubbert, Günter Duckeck, Patricia Méndez Lorenzo, Oliver Sahr, Raimund Ströhmer, and Tatjana Unverhau. None of this will be forgotten.

It is also high time to thank my mother, Irene Dubbert, for her ongoing support.

True friends are hard to find. I had the luck to find at least one: Stefanie Meyer.

Most of the analysis of this thesis was carried out using free software on Linux/GNU systems. A big thank you to all developers throughout the world who made this software possible.

Of course, this thesis was typeset using the L<sup>A</sup>T<sub>E</sub>X program and several extensions thereof. Nobody would ever dream of using something else for such a momentous task . . . Special thanks to Michel Goossens and Frank Mittelbach for a quick reply to my questions.

I would also like to thank some of the people who provided the much needed entertainment during the long time it took to write this thesis. To name but a few: Eric Adams, Trevor Bolder, Mick Box, Phillip Campbell, Scott Columbus, Mickey Dee, Raymond DeFeis, Joey DeMaio, Udo Dirkschneider, Jörg Fischer, Neil Gaiman, Frank Gilchrist, Wolf Hoffman, Stefan Kaufmann, Lee Kerslake, Lemmy Kilmister, Phil Lanzon, Karl Logan, Allan Moore, Terry Pratchett, Edward Pursino, and Bernie Shaw.







# Curriculum Vitae

**23. February 1970**

**Born in Paderborn, Germany**

1976

Primary school in Steinheim

1977–1980

Primary school in Germering

1980–1989

Secondary school (Max-Born Gymnasium Germering)

**June 1989**

**Abitur**

Major courses: Physics and Chemistry

June 1989–August 1990

Service in the Armed Forces at the 4th Air Defense Regiment at Regensburg

November 1990–December 1996

Studies of physics at the University of Munich (LMU)

July 1995–September 1996

Diploma thesis at the European Laboratory for High Energy Physics CERN near Geneva, Switzerland  
Title: *Bestimmung der Ortsauflösung von Hochdruck-driftrohren für das Myon-Spektrometer des ATLAS-Experimentes*  
Supervisor: Prof. Dr. M. Faessler

August 1996

Invited stay at CERN on behalf of the Muon Group of the ATLAS collaboration

**December 1996**

**Diploma of physics**

since January 1997

Scientific employee at the University of Munich (LMU)  
Doctoral thesis at the OPAL experiment  
Supervisor: Prof. Dr. D. Schaile

August 1997–September 1997

European Summer School for High Energy Physics in St. Andrews, Scotland





